Microwave properties of superconducting $SrTiO_3$ at mK-temperatures

Master Thesis verfasst von
Cenk Beydeda

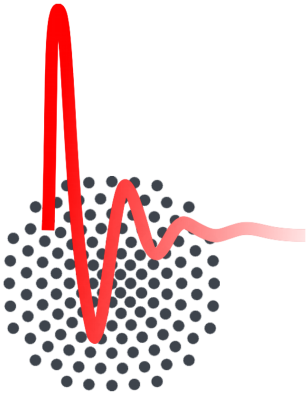

1. Physikalisches Institut
Universität Stuttgart

Hauptberichter	**Prof. Dr. Martin Dressel**
Mitberichter	**Prof. Dr. Sebastian Loth**
Betreuer	**Dr. Marc Scheffler**

7. November 2022

Contents

1 Motivation

Strontium titanate $SrTiO_3$ is interwoven with the history of superconductivity. Lightly doped $SrTiO_3$ was discovered to be superconducting in 1964 [1]. Early experiments revealed features of doped $SrTiO_3$ that are today associated with other unconventional superconductors: multiband superconductivity [2], the superconducting dome [3] and a perovskite structure [4]. Undoped $SrTiO_3$ shows a dielectric constant that rises to the order of $\epsilon_0 \sim 20000$ when approaching low temperatures [5]. Below 4 K the temperature dependence of $\epsilon_0(T)$ shows an anomaly [6, 7]. Undoped $SrTiO_3$ is referred to as quantum paraelectric, a material where quantum fluctuations at low temperatures prevent the phase transition in $SrTiO_3$ from a paraelectric to a ferroelectric. It is widely assumed that the quantum fluctuations and superconductivity in $SrTiO_3$ are linked [8, 9]. But so far the discussion on the origin of superconductivity is not settled although many proposals were made. The appealing aspect in this so far insufficiently understood material may be illustrated by quoting the discoverer of superconductivity in $SrTiO_3$ Schooley who said "If $SrTiO_3$ had magnetic properties, a complete study of this material would require a thorough knowledge of all of solid state physics" [10].

In the years after the discovery of superconductivity in $SrTiO_3$ the interest in this material decreased. It was believed that the main characteristics of $SrTiO_3$ were brought to daylight. Furthermore research in $SrTiO_3$ was seen as playground for basic research with no expectable practical benefit. This changed with the discovery of the 2-dimensional electron gas (2DEG) in the interface of undoped $SrTiO_3$ and $LaAlO_3$ that can also become superconducting [11, 12]. The superfluid density of the 2DEG in the $LaAlO_3/SrTiO_3$ interface was shown to be tunable when applying an external electric field [13]. The possibility to drive a state of matter from superconducting to almost insulating by applying a voltage motivates the development of new superconducting circuit elements [14]. Parallel to the research of the 2DEG in the $LaAlO_3/SrTiO_3$ interface the interest in one of the compounds $SrTiO_3$ was renewed.

The question whether Nb-doped $SrTiO_3$ is a single- or multi-gap superconductor is not conclusively clarified. The claim that Nb:$SrTiO_3$ is a multi-gap superconductor goes back to tunneling measurements by Binnig *et al.* who found two distinct peaks that correspond to two energy gaps, but when comparable measurements were performed by Swartz *et al.* single-gap s-wave BCS-behavior was observed [2, 15]. On the other hand the group of Kamran Behnia measured a kink in the thermal conductivity in the superconducting state in dependence of the magnetic flux density which was interpreted as two energy gaps and therefore supports Binnig's measurements [16]. Measurements of the optical conductivity and surface impedance carried out by Thiemann *et al.* reproduce the kink in the magnetic field but in the zero-field the optical data shows behavior as expected from a dirty s-wave single-gap BCS superconductor [17]. Thiemann argued that Nb:$SrTiO_3$ is a multiband superconductor whereas the small mean free path results in an averaging of the two energy gaps to a single energy gap according

to Anderson's theorem [18]. On the other hand the group of Kamran Behnia showed that Nb:$SrTiO_3$ is tuned from clean to dirty with greater doping [19]. So also the question whether Nb:$SrTiO_3$ is best described in the clean or dirty limit of superconductivity is not settled yet.

It becomes apparent that the experimental observations concerning Nb:$SrTiO_3$ up to now are not fully consistent. But there is also a lack in experimental data. The goal of this thesis is to contribute to the research in Nb:$SrTiO_3$. Therefore the samples from the previous work of Thiemann are reexamined with focus on the optical conductivity in a finite magnetic field. A thorough experimental investigation on the complex conductivity in a magnetic field so far is missing and may provide valuable insight into the superconducting state of Nb:$SrTiO_3$. Every effort in the experimental characterization of $SrTiO_3$ may be of value when it allows to come a step closer to understanding the origin of superconductivity in doped $SrTiO_3$.

2 Theoretical principles

2.1 Maxwell's equations

Maxwell's equations form the foundation for the description of the electromagnetic field [20]. In the presence of matter Maxwell's equations are given by [21]

$$\begin{aligned} \nabla \cdot \vec{D}(\vec{r},t) &= \rho(\vec{r},t) \\ \nabla \cdot \vec{B}(\vec{r},t) &= 0 \\ \nabla \times \vec{E}(\vec{r},t) &= -\partial_t \vec{B}(\vec{r},t) \\ \nabla \times \vec{H}(\vec{r},t) &= \vec{J}(\vec{r},t) + \partial_t \vec{D}(\vec{r},t) \end{aligned} \tag{2.1}$$

where $\vec{D} = \epsilon\vec{E}$ is the electric displacement field and $\vec{E}$ is the electric field, $\vec{B} = \mu\vec{H}$ is the magnetic flux density and $\vec{H}$ the magnetic field, $\epsilon = \epsilon_r\epsilon_0$ is the dielectric constant with the specific material dependent relative permittivity ϵ_r and the dielectric constant of vacuum $\epsilon_0 = 8.854 \cdot 10^{-12}\,\frac{\mathrm{F}}{\mathrm{m}}$. The magnetic permeability $\mu = \mu_0\mu_r$ is set to the value of the magnetic permeability in vacuum $\mu = \mu_0 = 1.2566 \cdot 10^{-6}\,\frac{\mathrm{Vs}}{\mathrm{Am}}$ with $\mu_r = 1$. ρ is the charge density, $\vec{J}$ is the current density.

With Ohm's law $\vec{J} = \sigma\vec{E}$ where σ is the conductivity and a harmonic time dependence $\partial_t\vec{D} = -i\omega\vec{D}$ with the frequency ω the fourth of Maxwell's equations (2.1) can be rewritten [21–23]

$$\nabla \times \vec{H} = -\mathrm{i}\omega\left(\epsilon + \frac{\mathrm{i}\sigma}{\omega}\right)\vec{E} = -i\omega\hat{\epsilon}\vec{E} \tag{2.2}$$

and a complex dielectric constant can be introduced

$$\hat{\epsilon} = \epsilon_1 + \mathrm{i}\epsilon_2 = \epsilon + i\frac{\sigma}{\omega} \tag{2.3}$$

with real part $\mathrm{Re}(\hat{\epsilon}) = \epsilon_1$ and imaginary part $\mathrm{Im}(\hat{\epsilon}) = \epsilon_2$. The complex dielectric constant

$$\hat{\epsilon} = \epsilon_0 + \frac{\mathrm{i}}{\omega}\hat{\sigma} \tag{2.4}$$

can be related to a complex conductivity $\hat{\sigma} = \sigma_1 + \mathrm{i}\sigma_2$ [21]. $\hat{\epsilon}(\omega)$ and $\hat{\sigma}(\omega)$ are response functions and therefore suffice the Kramers-Kronig relation [24].

2.2 Superconductivity

2.2.1 Introduction to superconductivity

In 1911 a new state of matter was discovered when Kammerlingh Onnes measured the vanishing DC-resistivity of mercury at the temperature of liquid helium [25]. The defining properties of the superconducting state that a theory of superconductivity must explain were listed by Bardeen, Cooper and Schrieffer in [26] and are

- the second-order phase transition at the critical temperature T_C,
- the dependence of the electronic specific heat $C_v \propto \exp(-T_0/T)$ on temperature T, here T_0 is an arbitrary constant [27],
- the exclusion of the magnetic field from the interior of the superconductor also known as Meissner-Ochsenfeld effect [28],
- the vanishing DC-resistance $\rho_{\mathrm{DC}}(T < T_C) = 0$
- and the isotope effect of element superconductors $T_C^I \sqrt{M^I} = \text{const.}$ where I marks different isotopes [29].

The above mentioned properties of so-called conventional superconductors that are typically associated with metallic element superconductors with $T_C < 20\,\mathrm{K}$ are well explained within the BCS theory that will be discussed in the next subsection. The BCS theory requires an attractive electron-electron interaction. Conventional superconductors are characterized by such an attractive electron-electron interaction by the exchange of virtual phonons below $T < T_C$.

In 1986 the first ceramic superconductor was discovered [30]. Since then new ceramic superconductors with a T_C greater than the boiling point of liquid nitrogen were discovered. For the ceramic superconductor as well as other superconductors the origin of the attractive electron-electron interaction is not known yet. Superconductors with an unknown origin of the attractive electron-electron interaction are referred to as unconventional superconductors. It is noted that the term 'unconventional superconductor' is used vaguely and may also refer to materials that are BCS superconductors but display distinct features such as two-band superconductivity and a superconducting dome [31, 32].

The research area of superconductivity may seem overwhelming due to massive amount of theoretical and experimental work. It is not the goal of this section to give a traceable description of the theory that is used throughout this thesis. The BCS theory will be discussed insofar as the theoretical arguments that lead to the important results are made plausible. In the other subsections on superconductivity the necessary concepts for this thesis are simply introduced. It is appropriate to mention some reference books. Most of this section is taken from Tinkham [33]. Another classic textbook for superconductivity was written by deGennes [34], Schmidt gives a nice introduction to superconductivity too [35]. Some theoretical books can also be found in the references [36–38]. The ultimate reference may be [10].

2.2.2 BCS theory

Cooper pair

The first microscopic description of the superconducting state that explained the before mentioned properties of conventional superconductors were given by Bardeen, Cooper and Schrieffer [26]. Cooper showed that in the presence of an attractive interaction V between two electrons at the Fermi surface E_F the energy E of both electrons is given by [39]

$$E = 2E_F - \frac{2\hbar\omega_C}{\exp\left(\frac{2}{N_\mathrm{n}(0)V_0}\right) - 1} \approx 2E_F - 2\hbar\omega_C \exp\left(-\frac{2}{N_\mathrm{n}(0)V_0}\right) \tag{2.5}$$

with the density of states (DOS) at the Fermi surface for one spin orientation $N_\mathrm{n}(0)$ in the normal conducting regime, the weak-coupling approximation $N_n(0)V_0 < 0.3$ is used with $V_0 > 0$. Cooper assumed that the electrons would interact in the momentum space (k-space) for energies ε between E_F and $E_F + \hbar\omega_C$ with $\hbar\omega_C \ll E_F$. The potential is assumed to be

$$V(\varepsilon) = \begin{cases} -V_0 & \text{for } E_F < \varepsilon < E_F + \hbar\omega_C \\ 0 & \text{else} \end{cases}. \tag{2.6}$$

In the BCS theory the cutoff frequency ω_C is set to the Debye frequency $\omega_C = \omega_D$ since the electron interaction is phonon mediated. In fact the framework of the BCS theory also applies to other ω_C with $\hbar\omega_C \ll E_F$ when $V(\varepsilon)$ can be expressed as in (2.6) [33]. $\hbar = h/(2\pi) = 1.055 \cdot 10^{-34}$ Js is Planck's constant [40].

BCS Ground state

The so-called pairing Hamilton is given by

$$\mathcal{H} = \sum_{\vec{k},\sigma} \varepsilon_{\vec{k}} c^*_{\vec{k},\sigma} c_{\vec{k},\sigma} + \sum_{\vec{k},\vec{l}} V_{\vec{k},\vec{l}} c^*_{\vec{k},\uparrow} c^*_{-\vec{k},\downarrow} c_{-\vec{l},\downarrow} c_{\vec{l},\uparrow} \tag{2.7}$$

where the sum goes over all Cooper pairs with energy $\varepsilon_{\vec{k}}$ wave vector $\vec{k}, \vec{l}$ and spin orientation $\sigma = \{\uparrow, \downarrow\}$. $V_{\vec{k},\vec{l}}$ is the interaction potential. In the mean-field approach of the BCS theory the ground state is assumed to be

$$|\psi_\mathrm{BCS}\rangle = \prod_{\vec{k}} \left(u_{\vec{k}} + v_{\vec{k}} c^*_{\vec{k},\uparrow} c^*_{-\vec{k},\downarrow}\right) |\phi_0\rangle \tag{2.8}$$

with the vacuum state $|\phi_0\rangle$ and probability amplitudes $u_{\vec{k}}, v_{\vec{k}}$. The normalization of the ground state requires $|u_{\vec{k}}|^2 + |v_{\vec{k}}|^2 = 1$. The BCS energy gap is defined as

$$\Delta_{\vec{k}} = -\sum_{\vec{l}} V_{\vec{k},\vec{l}} u_{\vec{k}} v_{\vec{l}}. \tag{2.9}$$

A variational approach to the Hamiltonian in equation (2.7) can be employed. The variation of the mean energy $\delta < E >$ is set to

$$\delta < E >= \delta \left\langle \psi_{\mathrm{BCS}} \right| \mathcal{H} - \mu \mathcal{N}_{\mathrm{op}} \left| \psi_{\mathrm{BCS}} \right\rangle = 0 \tag{2.10}$$

with the chemical potential μ and the particle-number operator $\mathcal{N}_{\mathrm{op}} = \sum_{\vec{k},S} c^*_{\vec{k},S} c_{\vec{k},S}$. It follows

$$u^2_{\vec{k}} = \frac{1}{2}\left(1 - \frac{\xi_{\vec{k}}}{E_{\vec{k}}}\right), \qquad v^2_{\vec{k}} = \frac{1}{2}\left(1 + \frac{\xi_{\vec{k}}}{E_{\vec{k}}}\right) \tag{2.11}$$

with $\xi_{\vec{k}} = \varepsilon_{\vec{k}} - E_F$ and $E_{\vec{k}} = \sqrt{\Delta^2_{\vec{k}} + \xi^2_{\vec{k}}}$.

The before made assumption in equation (2.6) for the interaction potential $V_{\vec{k},\vec{l}}$ results in a $\vec{k}$-independent $\Delta_{\vec{k}} = \Delta$. In this case equation (2.9) together with equation (2.11) can be solved and returns

$$\Delta(T=0) = \Delta_0 = \frac{\hbar\omega_C}{\sinh\left[1/(N_{\mathrm{n}}(0)V_0)\right]} \approx 2\hbar\omega_C \exp\left[-1/(N_{\mathrm{n}}(0)V_0)\right] \tag{2.12}$$

whereas in the last transformation the weak coupling approximation $N_{\mathrm{n}}(0)V_0 < 0.3$ is used again. In general $\Delta(T)$ is a temperature-dependent quantity. The energy gap is related to the critical temperature by

$$\Delta(T=0) = 1.764 \cdot k_B T_C \tag{2.13}$$

with the Boltzmann constant $k_B = 1.38 \cdot 10^{-23}\,\mathrm{J/K}$. The energy gap can be used to define the BCS coherence length

$$\xi_\Delta = \frac{\hbar v_F}{\pi \Delta_0} \tag{2.14}$$

with the Fermi velocity v_F [33].

Density of states

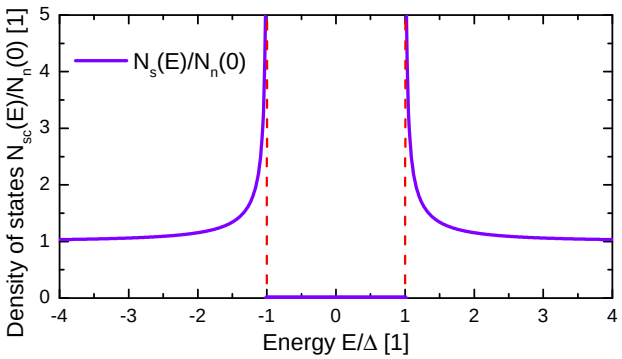

Fig. 2.1: Density of states in the superconducting state according to equation (2.15).

The density of states (DOS) in the superconducting regime $N_{\mathrm{sc}}(E)$ is given by

$$\frac{N_{\mathrm{sc}}(E)}{N_{\mathrm{n}}(0)} = \mathrm{Re}\left(\frac{|E|}{\sqrt{E^2-\Delta^2}}\right). \tag{2.15}$$

Note here that throughout this thesis the DOS is measured respective to the Fermi energy E_F, this means that $N_\alpha(E)$ is the DOS at energy $E_F + E$ and $\alpha = \mathrm{sc}, \mathrm{n}$ characterizes the superconducting and normal state. In figure 2.1 the density of states in the superconducting state can be seen. Characteristic for the superconducting state is $N_{\mathrm{sc}}(-\Delta < E < \Delta) = 0$ and $N_{\mathrm{sc}}(E = \pm\Delta) \to \infty$.

The occupation of the density of states depends on the temperature T and is given by the Fermi distribution

$$f_F(E) = \frac{1}{1+e^{\beta E}} \tag{2.16}$$

with the inverse temperature $\beta = 1/k_B T$ and the Boltzmann constant $k_B = 8.617 \cdot 10^{-5}\,\frac{\mathrm{eV}}{\mathrm{K}}$ [33, 40].

2.2.3 Bogoliubov deGennes equations

The BCS theory motivated generalizations of the theory of superconductivity. Gor'kov showed that the Ginzburg Landau theory is a limiting case of the BCS theory for T close to T_C [41]. Eliashberg found equations that allow to compute the superconducting state for a more complex interaction potential [42]. The Bogoliubov deGennes equations (BdG equations) generalize the BCS theory for a spatially varying pairing potential

$$\hat{\Delta}(\vec{r}) = \sum_n \hat{v}_n^*(\vec{r}) V (E_F + E_n) \hat{u}_n(\vec{r})\,(1 - 2 f_F(E_n)) \tag{2.17}$$

to

$$\begin{aligned} \hat{\mathcal{H}}_0 \hat{u}_i(\vec{r}) + \hat{\Delta}(\vec{r})\hat{v}_i(\vec{r}) &= E_i \hat{u}_i(\vec{r}) \\ -\hat{\mathcal{H}}_0 \hat{v}_i(\vec{r}) + \hat{\Delta}^*(\vec{r})\hat{u}_i(\vec{r}) &= E_i \hat{v}_i(\vec{r}) \end{aligned} \tag{2.18}$$

with

$$\hat{\mathcal{H}}_0 = \frac{1}{2m}\left(\hat{\vec{p}} - e\vec{A}\right)^2 + U(\vec{r}) - E_F. \tag{2.19}$$

Here m is the effective electron mass, $e = 1.602 \cdot 10^{-19}\,\mathrm{C}$ the elementary charge [40], $U(\vec{r})$ the interaction potential and the momentum operator is given by $\hat{\vec{p}} = -\mathrm{i}\hbar\vec{\nabla}$. The definition of the interaction potential (2.17) and the resemblance to equation (2.9) suggest that the introduced superconducting amplitudes $\hat{u}_i(\vec{r})$, $\hat{v}_i(\vec{r})$ can be seen as generalizations of equation (2.11) to the case of spatial inhomogeneity. The potential can be expressed in analogy to the BCS theory as equation (2.6). The index i denotes the eigenvalues E_i and eigenvectors $\hat{u}_i(\vec{r})$, $\hat{v}_i(\vec{r})$ [33].

2.2.4 Electrodynamics of superconductivity

London and Pippard equations

One of the early proposed phenomenological models on the electrodynamics of superconductors are the London equations [43]

$$\partial_t \vec{J}_{\mathrm{sc}} = \frac{n_{\mathrm{sc}} e^2}{m_e} \vec{E}, \quad \nabla \times \vec{J}_{\mathrm{sc}} = -\frac{n_{\mathrm{sc}} e^2}{m_e} \vec{B} \tag{2.20}$$

that explain the Meissner-Ochsenfeld effect and the vanishing DC resistance on a macroscopic scale. London assumed that the total density of electrons $n = n_{\mathrm{sc}} + n_{\mathrm{n}}$ is composed of the density of normal conducting electrons n_{n} and superconducting electrons n_{sc} with the according current density $\vec{J}_{\mathrm{sc}}$ of the superconducting electrons. The London penetration depth is defined as

$$\lambda_L = \sqrt{\frac{m_e}{\mu_0 n_{\mathrm{sc}} e^2}}. \tag{2.21}$$

In the framework of the London equations an external magnetic field $\vec{B}$ decays exponentially in the superconductor on the length scale of λ_L. The London equations can be also expressed as

$$\vec{J}_{\mathrm{sc}} = -\frac{1}{\mu_0 \lambda_L^2} \vec{A} \tag{2.22}$$

with vector potential $\vec{A}$.

Based on a generalization by Chambers for non-local normal conducting metals Pippard proposed as non-local generalization of equation (2.22)

$$\vec{J}_{\mathrm{sc}}(\vec{r}) = -\frac{3}{4\pi \mu_0 \xi_\Delta \lambda_L^2} \int_{\mathbb{R}^3} \frac{\vec{R}\left[\vec{R} \cdot \vec{A}(\vec{r}')\right]}{R^4} \mathrm{e}^{-R/\xi^*} \mathrm{d}\vec{r}' \tag{2.23}$$

for superconductors with $\vec{R} = \vec{r} - \vec{r}'$, $R = |\vec{R}|$, ${\xi^*}^{-1} = \xi_\Delta^{-1} + l^{-1}$ and mean free path l [44]. Pippard introduced ξ_Δ as experimentally observable length scale, the identification with the BCS coherence length was made within the BCS theory. The BCS theory reproduced equation (2.23) except the exponential that is replaced by the similar behaving BCS kernel function $J(R, T)$ [33].

Mattis Bardeen Formalism

The optical conductivity of a superconductor can be obtained by considering the absorption

$$\alpha_{\mathrm{sc}} = \int_{\mathbb{R}} |M|^2 F(\Delta, E, E + \hbar\omega) N_{\mathrm{sc}}(E) N_{\mathrm{sc}}(E + \hbar\omega) \cdot [f_F(E) - f_F(E + \hbar\omega)] \, \mathrm{d}E \tag{2.24}$$

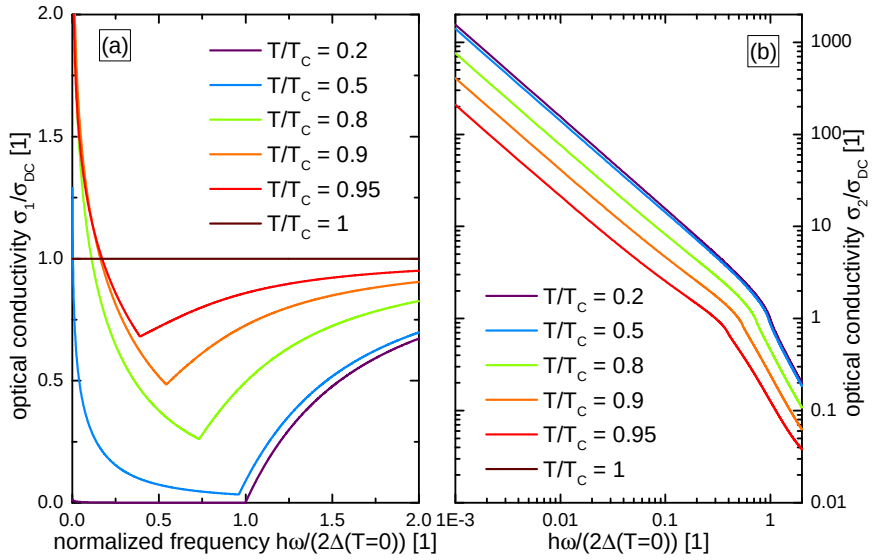

Fig. 2.2: The optical conductivity (2.26) in dependence of frequency $\omega = 2\pi f$ for different normalized temperatures T/T_C. The real part can be seen in (a), the imaginary part can be seen in (b).

that is proportional to the real part of the optical conductivity $\alpha_{\mathrm{sc}} \propto \sigma_1$ [33]. The absorption depends on the frequency $\omega = 2\pi f$ of the interacting electromagnetic field. Here $|M|^2$ is the transition matrix element and

$$F(\Delta, E, E+\hbar\omega) = \frac{1}{2}\left(1 + \frac{\Delta^2}{E(E+\hbar\omega)}\right) \tag{2.25}$$

is the case II coherence factor of superconductivity. Due to the phase-coherent superposition of superconducting one-electron states interference terms arise that can be taken into account with the coherence factor $F(\Delta, E, E+\hbar\omega)$. As result the electron creation and annihilation operator $c^*_{\vec{k},\sigma}$, $c_{\vec{k},\sigma}$ of the normal conducting state are not identical with the quasiparticle creation and annihilation operator of the superconducting state which give rise to interference terms.

The optical conductivity

$$\begin{aligned} f_1^{\mathrm{MB}}(\Delta,\omega) = \frac{\sigma_1(\omega)}{\sigma_{\mathrm{DC}}} &= \frac{2}{\hbar\omega}\int_{\Delta}^{\infty} \frac{(f_F(E) - f_F(E+\hbar\omega))\,(E^2+\Delta^2+\hbar\omega E)}{\sqrt{E^2-\Delta^2}\sqrt{(E+\hbar\omega)^2-\Delta^2}} \\ &\quad + \frac{\Theta(\hbar\omega-2\Delta)}{\hbar\omega}\int_{\Delta-\hbar\omega}^{-\Delta} \frac{(1-2f_F(E+\hbar\omega))\,(E^2+\Delta^2+\hbar\omega E)}{\sqrt{E^2-\Delta^2}\sqrt{(E+\hbar\omega)^2-\Delta^2}} \\ f_2^{\mathrm{MB}}(\Delta,\omega) = \frac{\sigma_2(\omega)}{\sigma_{\mathrm{DC}}} &= \frac{1}{\hbar\omega}\int_{\min(\Delta-\hbar\omega,-\Delta)}^{\Delta} \frac{(1-2f_F(E+\hbar\omega))\,(E^2+\Delta^2+\hbar\omega E)}{\sqrt{E^2-\Delta^2}\sqrt{(E+\hbar\omega)^2-\Delta^2}} \end{aligned} \tag{2.26}$$

was given by Mattis and Bardeen in the limit $l \to \infty$ [45]. The expressions are normalized to the DC conductivity in the normal state σ_{DC}. Zimmermann obtained an expression for $\hat{\sigma}$ for arbitrary l [46]. $\Theta(x)$ is the Heaviside step function [33].

Effective London penetration depth

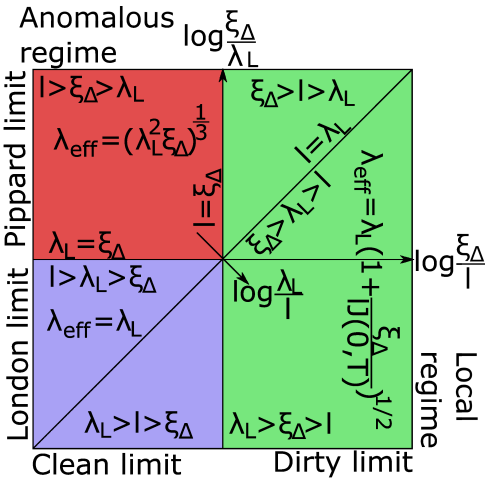

Fig. 2.3: Schematic depiction of the various limits in a superconductor with according λ_{eff}. The depiction is motivated from a similar one in [21].

London showed that an external magnetic flux density B is exponentially screened from the interior of a bulk superconductor at length scale λ_L. In fact the real penetration depth that will be referred to as effective London penetration depth $\lambda_{\mathrm{eff}}(\lambda_L, \xi_\Delta, l)$ depends on ξ_Δ and l in various ways in different limiting cases as will be shown next.

In the London limit $\xi_\Delta < \lambda_L$ the effective London penetration depth

$$\lambda_{\mathrm{eff}} = \lambda_L \tag{2.27}$$

equals the usual London penetration depth.

In the dirty limit $l < \xi_\Delta$ the effective London penetration depth is given by

$$\lambda_{\mathrm{eff}} = \lambda_L \sqrt{1 + \frac{\xi_\Delta}{J(0,T)l}} \tag{2.28}$$

with the BCS kernel function $J(0,0) = 1$, $J(0,T_C) = 1.33$. The London limit and the dirty limit are also referred to as local limit

The anomalous limit $\lambda_L < l, \xi_\Delta$, also referred to as clean limit and non-local limit, is given by

$$\lambda_{\mathrm{eff}} = (\xi_\Delta \lambda_L^2)^{\frac{1}{3}} \tag{2.29}$$

The limit of a superconductor may change with temperature since λ_L depends heavily on temperature close to T_C. In figure 2.3 the various limiting cases are schematically depicted. The distinction into the London-, dirty and anomalous limit is taken from [47] [33].

Surface impedance and optical conductivity

The relation between the surface impedance $\hat{Z}_S$ and the optical conductivity $\hat{\sigma}$ also depends on the investigated limit [47]. In analogy to [47] the relation between $\hat{Z}_S$ and $\hat{\sigma}$ is defined in a normalized manner. The physical foundation of the surface impedance $\hat{Z}_S$ is forwarded to the next section.

The local limit covers the London limit and the dirty limit that were mentioned before. With $R_n^L = \sqrt{\omega\mu_0/(2\sigma_{\mathrm{DC}})}$, the surface impedance $\hat{Z}_S$ in the local limit is given by

$$\frac{\hat{Z}_S}{R_n^L} = \sqrt{2}\left(i\frac{\hat{\sigma}}{\sigma_{\mathrm{DC}}}\right)^{-1/2}. \tag{2.30}$$

The non-local limit covers the anomalous limit. For these the surface impedance with $R_n^P = (\mu_0^2\omega^2 l/(4\sigma_{\mathrm{DC}}))^{1/3}$ is given by

$$\frac{\hat{Z}_S}{R_n^P} = 2\left(-\frac{\hat{\sigma}}{\sigma_{\mathrm{DC}}}\right)^{-1/3}. \tag{2.31}$$

Equation (2.30) and (2.31) are defined for the superconducting $\hat{Z}_S$ and superconducting $\hat{\sigma}$ within the limits that were defined previously. In fact equation (2.30) and (2.31) can also be used for normal conducting metals whereas the relevant length scale becomes the skin depth δ_S. In this case $l < \delta_S$ denotes the local limit and $l > \delta_S$ the non-local limit [21].

2.2.5 Ginzburg Landau theory

Introduction to Ginzburg Landau theory

The Ginzburg Landau theory (GL theory) is a phenomenological approach to the macroscopic properties of superconductors. The GL equations follow from an expansion of the free energy. A complex space-dependent order parameter $\psi_{\mathrm{GL}}(\vec{r})$ is introduced that can be related to the local density of superconducting electrons $n_{\mathrm{sc}}(\vec{r}) = |\psi_{\mathrm{GL}}(\vec{r})|^2$. Gor'kov showed that the order parameter is proportional to the energy gap, both being complex quantities, for T close to T_C [41]. This subsection on GL theory will focus on the distinction into type I and type II superconductors, the Ginzburg Landau coherence length and the Shubnikov phase [33].

Type I and Type II superconductors

The GL theory introduces a new length scale, the so-called Ginzburg Landau coherence length $\xi_{\mathrm{GL}}(T)$. A small disturbance of $\psi_{\mathrm{GL}}(\vec{r})$ decays on a length scale of ξ_{GL}. For a superconductor in the local regime it can be related

$$\frac{\xi_{\mathrm{GL}}(T)}{\xi_{\Delta}} = \frac{\pi}{2\sqrt{3}} \frac{B_C(T=0)}{B_C(T)} \frac{\lambda_L(T=0)}{\lambda_{\mathrm{eff}}(T)} \tag{2.32}$$

with the critical magnetic flux density $B_C(T)$ that marks the transition between the superconducting and the normal conducting phase. For $T \to 0$ it is obtained in the London limit

$$\xi_{\mathrm{GL}} = 0.907 \cdot \xi_{\Delta} \tag{2.33}$$

and in the dirty limit

$$\xi_{\mathrm{GL}} = 0.907 \cdot \sqrt{\xi_{\Delta} l}. \tag{2.34}$$

Furthermore the Ginzburg Landau coefficient (GL coefficient) can be defined

$$\kappa = \frac{\lambda_{\mathrm{eff}}}{\xi_{\mathrm{GL}}}. \tag{2.35}$$

A superconductor with $\kappa < 1/\sqrt{2}$ is referred to as type I superconductor and displays the before mentioned properties of superconductivity. A superconductor with $\kappa > 1/\sqrt{2}$ is referred to as type II superconductor and displays two critical magnetic flux densities B_{C1}, B_{C2}. For $B < B_{C1}$ type II superconductors expel the external B. For $B_{C1} < B < B_{C2}$ the external B penetrates the superconductor within a laminar lattice of vortices. The type II superconductor becomes normal conducting for $B > B_{C2}$ [33].

Shubnikov phase

For $B_{C1} < B < B_{C2}$ a type II superconductor is partially penetrated by the external magnetic flux density within a triangular lattice of vortices. The superconducting state is then referred to as Shubnikov phase or mixed state. The superconductor displays spatial inhomogeneity due to the vortices. The Shubnikov phase was predicted by Abrikosov [48]. In figure 2.4 the schematic dependence of the magnetization on the external magnetic flux density can be seen. It is noted that also for type II superconductors a B_C can be defined where the area below the blue dashed and the black curve are the same.

A vortex contains a flux quantum $\Phi_0 = h/(2e)$. The superconducting order parameter within the vortex rises radially approximately as

$$\psi_{\mathrm{GL}}(r) \propto \tanh \frac{r}{\xi_{\mathrm{GL}}}. \tag{2.36}$$

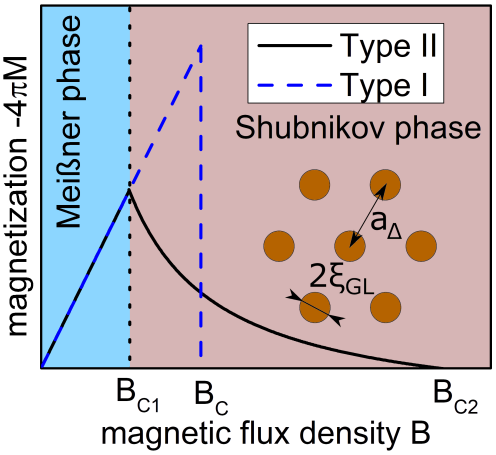

Fig. 2.4: Schematic dependence of the magnetization on the external magnetic flux density for a type I and type II superconductor with the same B_C. The inset shows the vortex lattice with spacing a_Δ and radius ξ_{GL}.

with distance r from the vortex core. The confined magnetic flux density inside of the vortex varies radially as

$$B_{\mathrm{vortex}}(r) = \frac{\Phi_0}{2\pi\lambda_{\mathrm{eff}}^2} K_0\left(\frac{r}{\lambda_{\mathrm{eff}}}\right) \tag{2.37}$$

with the 0'th order Bessel function $K_0(x)$. The distance between two vortices is given by

$$a_\Delta(B) = \left(\frac{4}{3}\right)^{\frac{1}{4}} \left(\frac{\Phi_0}{B}\right)^{\frac{1}{2}}. \tag{2.38}$$

The upper critical magnetic field is given by

$$B_{C2}(T=0) = \frac{\Phi_0}{2\pi\xi_{\mathrm{GL}}^2(T=0)}. \tag{2.39}$$

Since $\psi_{\mathrm{GL}}(r)$ rises on length scale ξ_{GL} the radius of a vortex is usually set to ξ_{GL} to apply methods of Effective Medium theory more easily although a single vortex does not possess a sharp edge [33].

2.3 Microwave principles

2.3.1 Propagation in a waveguide

This subsection will provide the foundation to relate the surface impedance $\hat{Z}_S$ with the microwave properties of superconducting resonators, specifically the resonance frequency f_0 and the frequency width f_b. The most general case of a waveguide of arbitrary shape as depicted in figure 2.5 is considered. The waveguide displays translational invariance in z direction. Together with an exponential time dependence the vector potential can be

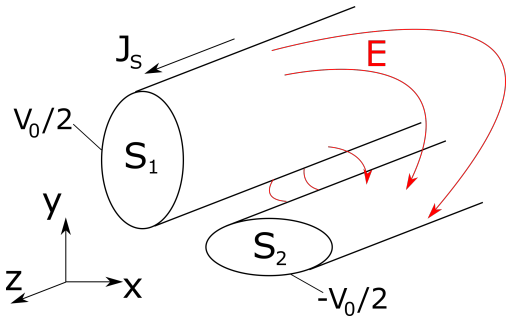

Fig. 2.5: Schematic depiction of a waveguide of arbitrary shape with translational invariance in z direction. The cross sections of the conductors are labeled as S_1 and S_2 with potential amplitudes $\pm V_0/2$ on the contour of S_1 and S_2. The surface current $\vec{J}_S$ and electric field $\vec{E}$ can be seen in the depiction.

expressed as $\vec{A} = \vec{e}_z \psi(x,y) \exp(-\gamma_P z - \mathrm{i}\omega t)$. γ_P is the propagation constant and $\psi(x,y)$ is a scalar field. The following derivation of γ_P is taken from [49], for a more complete discussion the reader is referred to this textbook.

With the Lorenz gauge $\nabla \cdot \vec{A} = \mathrm{i}\omega\epsilon\mu\phi$ the potential ϕ can be expressed in terms of $\vec{A}$. The potential on the surface of the conductor is a voltage wave $\phi = \pm\frac{1}{2} V_0 \exp(-\gamma_P z - \mathrm{i}\omega t)$ with opposite sign on the conductor contours ∂S_1 and ∂S_2. Here ∂S_1 and ∂S_2 denote the contour respectively of the cross sections S_1 and S_2. The electromagnetic field is related to the vector potential $\vec{A}$ by

$$\begin{aligned} \vec{B} &= \nabla \times \vec{A}, \\ \vec{E} &= \mathrm{i}\omega\vec{A} + \mathrm{i}\frac{\nabla\left(\nabla \cdot \vec{A}\right)}{\omega\epsilon\mu}. \end{aligned} \tag{2.40}$$

$\vec{A}$ fulfills the wave equation

$$\left(\nabla^2 + k^2\right)\vec{A} = 0 \tag{2.41}$$

with the wave number $k = \omega\sqrt{\epsilon\mu} = \omega\sqrt{\epsilon_r}/c$ and $c = 2.998 \cdot 10^8\,\mathrm{m/s}$ is the speed of light [40]. On the contour of ∂S_1 and ∂S_2 the surface current J_S can be related to the E-field by defining the surface impedance $\hat{Z}_S$ such that $\hat{Z}_S J_S = \vec{e}_z \vec{E}$.

Equation (2.41) can be rewritten to

$$\nabla_{xy}^2 \psi + k_c^2 \psi = 0 \tag{2.42}$$

with the Nabla operator in the xy-plane $\nabla_{xy} = \partial_x^2 + \partial_y^2$ and $k_c^2 = k^2 + \gamma_P^2$. ψ fulfills the boundary condition

$$\left(-\frac{\mathrm{i}\omega\epsilon\hat{Z}_S}{k_c^2}\frac{\partial\psi}{\partial n} - \psi\right)|_{\partial S_1, \partial S_2} = 0 \tag{2.43}$$

on the surface of the conductor whereas the normal vector $\vec{n}$ is directed into the conductor. Assuming $\hat{Z}_S = 0$ results in $\gamma_P = -\mathrm{i}k$ which is purely imaginary and no damping or change in frequency may be expected, this is consistent with an ideal transmission line.

Equation (2.42) may be rewritten to

$$k_c^2 = -\frac{\int \psi \nabla_{xy}^2 \psi \,\mathrm{d}x\mathrm{d}y}{\int \psi^2 \,\mathrm{d}x\mathrm{d}y}. \tag{2.44}$$

where the integral goes over the whole xy-plane. The expression

$$-k_c^2 \int \psi^2 \,\mathrm{d}x\mathrm{d}y = \int \psi \nabla_{xy}^2 \psi \,\mathrm{d}x\mathrm{d}y - \oint_{C=\partial S_1, \partial S_2} \left(-\frac{\mathrm{i}\omega\epsilon \hat{Z}_S}{k_c^2} \frac{\partial \psi}{\partial n} - \psi \right) \frac{\partial \psi}{\partial n} \,\mathrm{d}l \tag{2.45}$$

is equivalent to (2.44) since the contour integral over ∂S_1 and ∂S_2 vanishes due to the boundary condition (2.43). Here $\mathrm{d}l$ denotes the infinitesimal path variable that is used to integrate over $C = \partial S_1, \partial S_2$. In contrast to equation (2.44) the variation of k_c in equation (2.45) vanishes in first order and therefore provides a solution for the propagation in a lossy waveguide that is correct up to the second order when inserting ψ_0 of an ideal transmission line.

The solution to equation (2.42) for $\hat{Z}_S = 0$, this means the solution for the ideal transmission line, is referred to as ψ_0. As normalization it is set $\int \psi_0^2 \mathrm{d}S = \mu\epsilon$. The surface current that goes into opposite direction on S_1 and S_2 is given by $\mu|\vec{J}_S| = |\partial\psi_0/\partial n|$. Equation (2.45) can be rewritten to

$$k_c^2 = -\sqrt{\frac{\mu}{\epsilon}} \frac{V_0}{2} \left(\oint_{S_1} |\vec{J}_S| \mathrm{d}l + \oint_{S_2} |\vec{J}_S| \mathrm{d}l \right) - \mathrm{i} \frac{k\hat{Z}_S}{k_c^2} \sqrt{\frac{\mu}{\epsilon}} \oint_{S_1+S_2} |\vec{J}_S|^2 \mathrm{d}l. \tag{2.46}$$

The first two integrals return respectively the total current I_0 on each conductor. The last integral is expected to be proportional to I_0^2 but will depend on the geometry of the setup. A geometry factor Γ is introduced such that

$$\frac{2\pi\sqrt{\mu\epsilon} V_0 I_0}{\Gamma} = \oint_{\partial S_1 + \partial S_2} |\vec{J}_S|^2 \mathrm{d}l. \tag{2.47}$$

Equation (2.46) may be rewritten to

$$k_c^4 + k_c^2 \sqrt{\frac{\mu}{\epsilon}} V_0 I_0 + \mathrm{i}k\hat{Z}_S 2\pi\mu \frac{V_0 I_0}{\Gamma} = 0. \tag{2.48}$$

Solving the quadratic formula and assuming $k\hat{Z}_S\epsilon \ll V_0 I_0 \Gamma$ returns

$$\gamma_P = \mathrm{i}k + \frac{\pi\sqrt{\epsilon\mu}}{\Gamma}\hat{Z}_S = \mathrm{i}\left(k + \frac{\pi\sqrt{\epsilon\mu}}{\Gamma} X_S \right) + \frac{\pi\sqrt{\epsilon\mu}}{\Gamma} R_S = i\beta_P - \alpha_P \tag{2.49}$$

where β is the propagation coefficient and α the attenuation coefficient. Thus a small but finite surface impedance $\hat{Z}_S$ results in a change of propagation and introduces attenuation.

2.3.2 Transmission coefficient

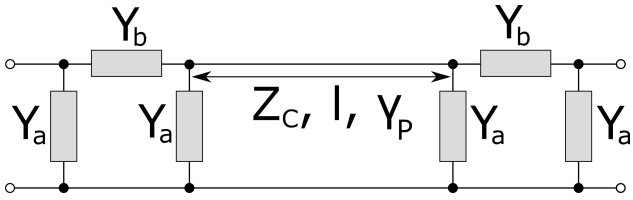

Fig. 2.6: Circuit diagram of the microwave setup. The two gaps are modeled as Π-network. The center conductor is between both Π networks with circuit impedance Z_C, resonator length l and propagation coefficient γ. Y_i are the coupling admittances.

In this subsection the transmission coefficient S_{21} for a generic resonator setup is computed. A resonator can be constructed from an arbitrary waveguide as depicted in 2.5 by introducing two gaps on one conductor. The two gaps have the distance l. In analogy to [50] a gap is modeled as Π network with admittances Y_a and Y_b. The part between the two gaps is modeled as waveguide with propagation coefficient γ_P, length l and circuit impedance Z_C. In figure 2.6 the complete circuit diagram of the resonator setup can be seen. The resonator setup is discussed in the next chapter 3.2.

With the ABCD matrix approach the transmission coefficient [51]

$$\hat{S}_{21}(\omega) = \frac{2}{A + B/Z_C + CZ_C + D} \tag{2.50}$$

can be given with

$$\begin{bmatrix} A & B \\ C & D \end{bmatrix} = \begin{bmatrix} 1 + \frac{Y_a}{Y_b} & \frac{1}{Y_b} \\ 2Y_a + \frac{Y_a^2}{Y_b} & 1 + \frac{Y_a}{Y_b} \end{bmatrix} \begin{bmatrix} \cos(il\gamma_P) & iZ_c \sin(il\gamma_P) \\ \frac{i}{Z_c}\sin(il\gamma_P) & \cos(il\gamma_P) \end{bmatrix} \begin{bmatrix} 1 + \frac{Y_a}{Y_b} & \frac{1}{Y_b} \\ 2Y_a + \frac{Y_a^2}{Y_b} & 1 + \frac{Y_a}{Y_b} \end{bmatrix}. \tag{2.51}$$

$Y_i = \mathrm{i}\omega C_i$ with $i = \mathrm{a}, \mathrm{b}$ are the coupling admittances with coupling capacitances C_i. A normalized coupling coefficient $r_i = \omega C_i Z_C$ can be defined.

Frequencies close to resonance $\beta_P = \sqrt{\epsilon\mu}(n\omega_0^* + \delta\omega)$ with small losses $\alpha_P l \ll 1$ are assumed. $n = 1, 2, 3, ...$ is the integer mode number and ω_0^* is defined such that $\omega_0^* l\sqrt{\epsilon\mu} = \pi$ as expected for a half-wavelength resonator. $\hat{S}_{21}(\omega)$ depends on the frequency ω, the quantity $\delta\omega$ with $\delta\omega \ll \omega_0^*$ is introduced as new variable for the transmission coefficient $\hat{S}_{21}(\delta\omega)$. It is noted with emphasis that the propagation coefficient β_P is not the wave vector, in fact with equation (2.49) it is obtained

$$\omega + \frac{\pi}{\Gamma} X_S = n\omega_0^* + \delta\omega. \tag{2.52}$$

The made assumptions allow to set $\cos(\mathrm{i}\gamma_P l) \approx 1$ and $\sin(\mathrm{i}\gamma_P l) = -\pi\delta\omega/\omega_0^* - \mathrm{i}l\alpha_P$ as first order Taylor expansion. Further it is assumed $r_a \ll r_b$ so that it can be set $r_a = 0$. As result

$$\hat{S}_{21}(\delta\omega) = \frac{2\left(Z_C Y_b\right)^2}{2\left(Z_C Y_b\right)^2\left(1 + l\alpha_P - \frac{\mathrm{i}\pi\delta\omega}{\omega_0^*}\right) + 2Z_C Y_b\left(1 + l\alpha_P - \frac{\mathrm{i}\pi\delta\omega}{\omega_0^*}\right) + l\alpha_P - \frac{\mathrm{i}\pi\delta\omega}{\omega_0^*}} \tag{2.53}$$

is obtained. In the weak coupling regime $r_b = \omega C_b Z_C \ll 1$ it is obtained

$$\hat{S}_{21}(\delta\omega) = -\frac{2r_b^2}{l\alpha_P - \mathrm{i}\left(\frac{\pi\delta\omega}{\omega_0^*} - 2r_b\right)}. \tag{2.54}$$

The coupling introduces a small shift

$$\delta\omega_C = \frac{2r_b\omega_0^*}{\pi} = \omega\frac{2C_bZ_C}{l\sqrt{\epsilon\mu}} \tag{2.55}$$

of the resonance frequency. Since $C_b(\omega)$ only depends weakly on ω, $\delta\omega_C \propto \omega$ [50], the higher modes are equidistantly spaced for $\hat{Z}_S = 0$. Equation (2.54) motivates a complex Lorentzian

$$L(f) = \frac{A}{\frac{f_b}{2} + \mathrm{i}\,(f - f_0)} \tag{2.56}$$

with $\omega = 2\pi f$, resonance frequency f_0, frequency width f_b and amplitude A.

2.3.3 Microwave properties due to finite $\hat{Z}_S$

In the previous section the identification $f_b\pi\sqrt{\epsilon\mu} = \alpha_P$ was made towards the Lorentzian and the phase of π absorbed into A. In general the attenuation constants

$$\alpha = \alpha_P + \alpha_D + \alpha_R \tag{2.57}$$

are additive, $\alpha_P = \pi\sqrt{\epsilon\mu}R_S/\Gamma$ accounts for the surface impedance of the conductor, α_D for losses in the dielectric and α_R for radiation losses [51]. The frequency width due to the additive attenuation constants is then given by $f_b\pi\sqrt{\epsilon\mu} = \alpha$. It is noted that the relation $f_b\pi\sqrt{\epsilon\mu} = \alpha$ only holds true in the weak coupling regime $r_b = \omega C_b Z_C \ll 1$.

The resonance frequency $\omega_0 = 2\pi f_0$ for a lossy conductor in the weak coupling regime can be obtained by comparing the coefficients in equation (2.54) and (2.56) while accounting for (2.52), it is then obtained

$$\omega_0 = n\omega_0^* + \frac{2\omega_0^*}{\pi}\omega C_bZ_C - \frac{\pi}{\Gamma}X_S. \tag{2.58}$$

It is assumed that the main losses occur due to the surface impedance in the weak coupling regime $r_b \ll 1$ so that $\alpha = \alpha_P$ and $\Delta\omega_0 = 2\pi\Delta f_0 = n\omega_0^* - \omega_0 = \pi X_S/\Gamma$. It follows

$$\hat{Z}_S = R_S + \mathrm{i}X_S = 2\Gamma\left(\frac{f_b}{2} + \mathrm{i}\Delta f_0\right). \tag{2.59}$$

3 Experimental techniques

3.1 He^3/He^4 Dilution Refrigerator

Microwave measurements with superconducting samples such as Nb:$SrTiO_3$ require low temperatures. In a liquid He_4 bath cryostat temperatures of around 1 to 2 K can be reached. To reach these temperatures the boiling temperature of He_4 is lowered by pumping He_4 from the bath cryostat. To reach even lower temperatures in the mK regime a He_3/He_4 dilution refrigerator is used.

In figure 3.1 a schematic view on a dilution refrigerator can be seen. The He_3/He_4 mixture is in a separated circulation system. Two cold traps respectively in liquid nitrogen and in liquid He_4 ensure that the valuable mixture is preserved and purified. When the He_3/He_4 mixture is condensed and below $T < 0.86\,\mathrm{K}$ a phase separation of the He_3/He_4 mixture into a He_3 rich phase and a He_3 poor phase occurs. Both phases are in equilibrium and separated. Pumping He_3 from the He_3 poor phase will result in a He_3 flow from the He_3 rich phase into the He_3 poor phase to maintain the equilibrium between both phases. The necessary energy to maintain the equilibrium is extracted from the environment as heat. This is the main cooling mechanism to reach mK-temperatures [52].

The 1K pot is used to cool and condense the He_3/He_4 mixture before it enters the mixing chamber. A constant He_4 flow in the 1 K pot ensures a temperature of around 1.7 K in the 1 K pot. The constant He_4 flow in the 1 K pot is controlled by the 1 K Needle Valve (1 K NV). In the mixing chamber the He_3/He_4 mixture has the lowest temperature. The previously described cooling mechanism due to the phase separation takes place in the mixing chamber. The inset that contains the circulation system and the sample is in vacuum down to 10^{-5} hPa. The base temperature is only limited by external heat inputs such as the coaxial cables. In this setup the mixing chamber reaches a base temperature of 25 mK.

The sample in this experiment is mounted in a brass box with 1.85 mm connectors. The brass box contains the stripline setup that is introduced in the next section. The sample is connected via coaxial cables with the VNA. The wiring in the dilution refrigerator is thermally coupled to reduce heat input. In the He_4 bath a superconducting magnet is located that can provide an external magnetic flux density B_{ext} at the position of the sample. Experiments that employ the described setup can be found in [17, 53–55].

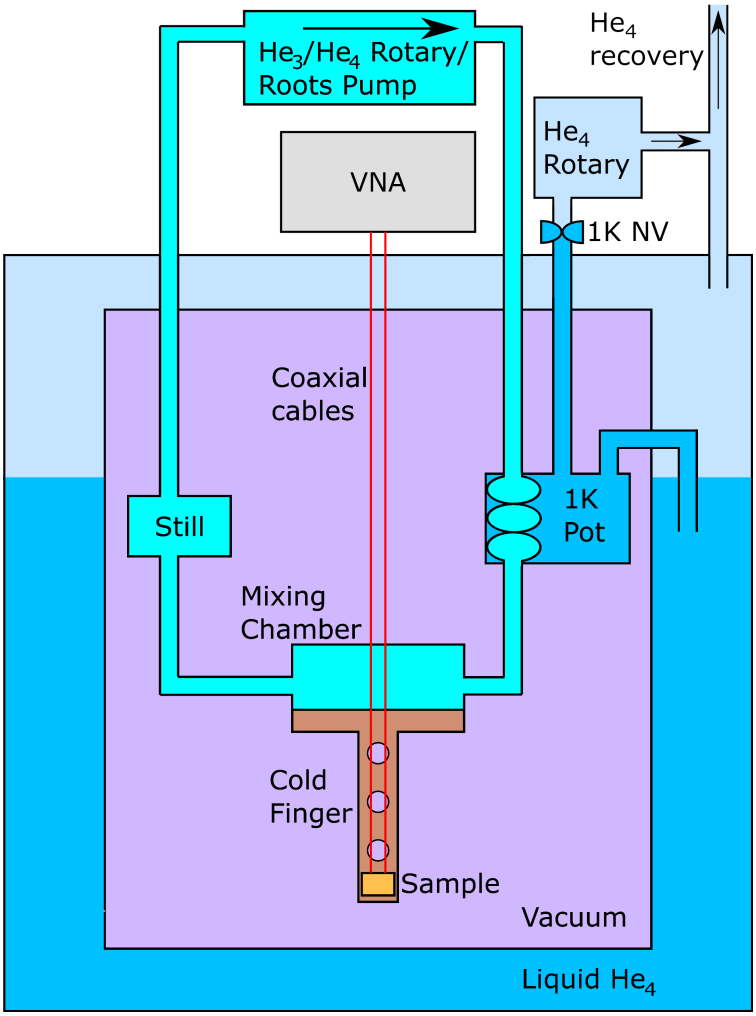

Fig. 3.1: Schematic view on the dilution refrigerator. The He_3/He_4 mixture is in a separated circulation system to preserve the valuable mixture. In the mixing chamber temperatures down to 25 mK are reached. The He_3/He_4 mixture is precooled in the 1K pot with liquid He_4. The He_3/He_4 rotary pump, the roots pump and the He_4 rotary pump maintain low pressure in the mixing chamber and the 1K pot respectively to ensure the low base temperature. The mixing chamber cools the cold finger with the sample. The sample is connected via coaxial cables with a Vector Network Analyzer (VNA) for microwave measurements.

3.2 Stripline setup

3.2.1 Stripline geometry

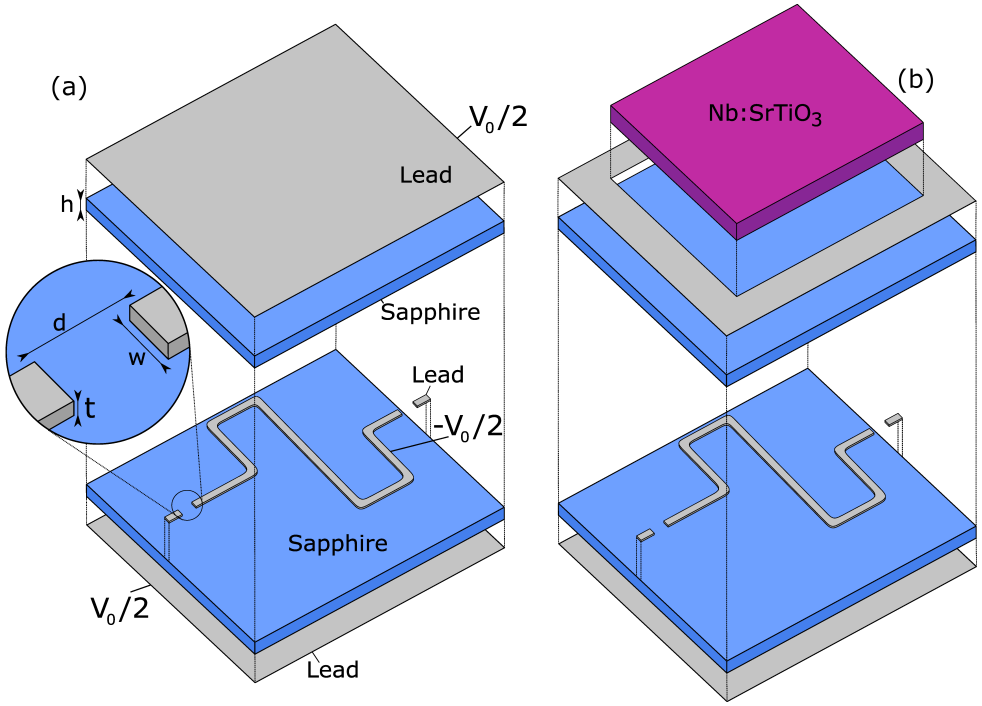

Fig. 3.2: (a) shows a schematic exploded view on a stripline microwave conductor. The potential difference between upper and lower groundplane and the center conductor is V_0. The center conductor is of thickness t and width w with gap distance d. Both sapphire plates have height h. (b) shows the same as (a) except that the upper groundplane is replaced with an interesting sample like Nb:$SrTiO_3$.

A stripline feedline consists of a center conductor that is sandwiched between two groundplanes. The potential difference between the groundplane and the center conductor is V_0. The ground plane and the center conductor are separated by a sapphire bulk with height $h = 127\,\mu m$. The height of the sapphire h, the thickness $t = 1\,\mu m$ and the width $w = 50\,\mu m$ of the center conductor determine the circuit impedance Z_C. Introducing two gaps of length $d = 50\,\mu m$ into the center conductor turns the stripline feedline into a stripline resonator. The coupling capacitance C depends on d. An appropriate circuit diagram for the setup as described can be seen in figure 2.6. In figure 3.2 in (a) a schematic depiction of the stripline resonator can be seen. The length of the center conductor between both gaps is l. The stripline resonators investigated in this thesis are made out of lead except one resonator in chapter 4 that is made out of tin.

The Nb:$SrTiO_3$ samples can replace the upper ground plane by partially removing the lead and placing the Nb:$SrTiO_3$ sample on top with GE varnish. This is schematically depicted in figure 3.2 in (b). The Nb:$SrTiO_3$ sample covers the whole meander structure of the center conductor. In this case Nb:$SrTiO_3$ acts as perturbation on the microwave resonators. With

the help of the cavity perturbation technique it is possible to extract the optical properties of $SrTiO_3$ from the microwave data.

Experiments that employ the described setup can be found in [17, 53, 55–58].

3.2.2 Microwave properties of the Stripline setup

With the help of conformal mapping techniques the circuit impedance

$$Z_C = \frac{1}{4}\sqrt{\frac{\mu}{\epsilon}}\frac{K(k_e)}{K(k_e')} \tag{3.1}$$

can be given with the inverse elliptic function $K(k_e)$ with argument

$$k_e = \frac{1}{\cosh\frac{\pi w'}{4h}}, \quad k_e' = \sqrt{1-k_e^2} \tag{3.2}$$

and effective width w' and height $h = 127\,\mu$m [22]. Z_C also depends on the relative permittivity ϵ_r since it is $\epsilon = \epsilon_0\epsilon_r$. The effective width w' is related to the real width $w = 50\,\mu$m and thickness $t = 1\,\mu$m by [59]

$$w' = w + \frac{t}{\pi}\ln\frac{\exp(1)}{\sqrt{\left[\frac{1}{3h/t+1}\right]^2 + \left[\frac{1/(4\pi)}{w/t+1.1}\right]^m}}, \quad m = \frac{6}{3+t/h}. \tag{3.3}$$

As dielectric sapphire is used. Despite of small anisotropies of sapphire it is set $\epsilon_r = 10$ [22]. The parameters are chosen such that $Z_C \approx 50\,\Omega$ and reflections between the coaxial cables and the stripline setup are minimized. The geometry factors are given by [49]

$$\frac{\pi\sqrt{\epsilon\mu}}{\Gamma_{gp}} = \frac{\pi^2 w}{64 Z_C h^2 \left[K(k_e')k_e'\right]^2} \approx 12.3\,\frac{1}{\Omega\mathrm{m}} \tag{3.4}$$

for both groundplanes together and

$$\begin{aligned}\frac{\pi\sqrt{\epsilon\mu}}{\Gamma_{cc}} &= \frac{\pi}{16 Z_c h k_e' K(k_e')^2}\int_0^{K(k_e')} \mathrm{d}x\left[\mathrm{sn}^2(x,k_e') + (K(k_e')\Delta v)^2\mathrm{cn}^2(x,k_e')\mathrm{dn}^2(x,k_e')\right]^{-\frac{1}{2}} \\ &\approx 246\,\frac{1}{\Omega\mathrm{m}}\end{aligned} \tag{3.5}$$

for the center conductor with

$$\left(1+k_e^4\right)^{\frac{1}{4}} K(k_e')\Delta v = \frac{\pi}{4h}e^{-\pi/2}\sqrt{\frac{4wt}{\pi}}. \tag{3.6}$$

The functions sn, cn and dn are the Jacobi elliptic functions. Going back to equation (2.47) the total Γ can be obtained by summing the partial Γ_i of the respective contour integrals

$$\frac{1}{\Gamma} = \sum_i \frac{1}{\Gamma_i}. \tag{3.7}$$

It is $\Gamma_{gp} = 2.69\,\Omega/\mathrm{GHz}$ and $\Gamma_{cc} = 0.135\,\Omega/\mathrm{GHz}$.

The coupling admittances $Y_{i=a,b} = \mathrm{i}\omega C_{i=a,b} = \mathrm{i}r_{i=a,b}/Z_C$ of the stripline setup are given by [50, 60, 61]

$$r_a = \omega C_a Z_c = -\frac{\frac{2h}{\lambda}\left(\frac{J_1(\pi d/\lambda)}{2h/\lambda}\right)^2}{1 - \frac{3}{4}\left(\frac{\pi d}{2\lambda}\right)^2 + \left(\frac{\pi d}{2\lambda}\right)^2 \ln\frac{4h}{\pi d} + \frac{1}{6}\left(\frac{\pi d}{4h}\right)^2 - 2\left(\frac{\pi d}{4h}\right)^2 S_1(\frac{2h}{\lambda})} \tag{3.8}$$

and

$$\begin{aligned} r_b = \omega C_b Z_c = &-\frac{1}{2} r_a + \frac{1}{2}\frac{4h/\lambda}{(J_0(\pi d/\lambda))^2} \\ &\left\{\left[1 - \left(\frac{\pi d}{2\lambda}\right)^2\right] \ln\frac{4h}{\pi d} + S_0\left(\frac{2h}{\lambda}\right) + \frac{1}{2}\left(\frac{\pi d}{2\lambda}\right)^2 - \frac{1}{6}\left(\frac{\pi d}{4h}\right)^2 + 2\left(\frac{\pi d}{4h}\right)^2 S_1\left(\frac{2h}{\lambda}\right)\right\} \end{aligned} \tag{3.9}$$

with

$$S_0(x) = \sum_{n=1}^{\infty}\left(\frac{1}{\sqrt{n^2 - x^2}} - \frac{1}{n}\right) \tag{3.10}$$

and

$$S_1(x) = \sum_{n=1}^{\infty}\left(\sqrt{n^2 - x^2} - n + \frac{x^2}{2n}\right) \tag{3.11}$$

and the gap width $d = 50\,\mu\mathrm{m}$. λ is the wavelength in the dielectric. $J_i(x)$ is the Bessel function of i'th order. For computational evaluation the sum only goes to $n = 5$. The admittances Y_i can be seen in the circuit diagram in figure 2.6.

3.3 Fitting technique

With the help of the ABCD matrix approach it was shown that the transmission coefficient $\hat{S}_{21}$ may be fitted with a Lorentzian as in equation (2.56). The Vector Network Analyzer (VNA) used in the setup measures the transmission coefficient $\hat{S}_{21}$. As fit equation for the resonance it is used

$$\hat{S}_{21}(f) = e^{if\tau}\left[\frac{v_1}{f - v_2} + v_3 + v_4 \cdot (f - \mathrm{Re}(v_2))\right]. \tag{3.12}$$

Here the coefficients v_i and τ are complex fitting parameters. The coefficients $v_1 = -\mathrm{i}A$ and $v_2 = f_0 + \mathrm{i}f_b/2$ characterize the resonance. The coefficients v_3 and v_4 model the background of the transmission spectrum in the vicinity of the resonance as linear Taylor expansion.

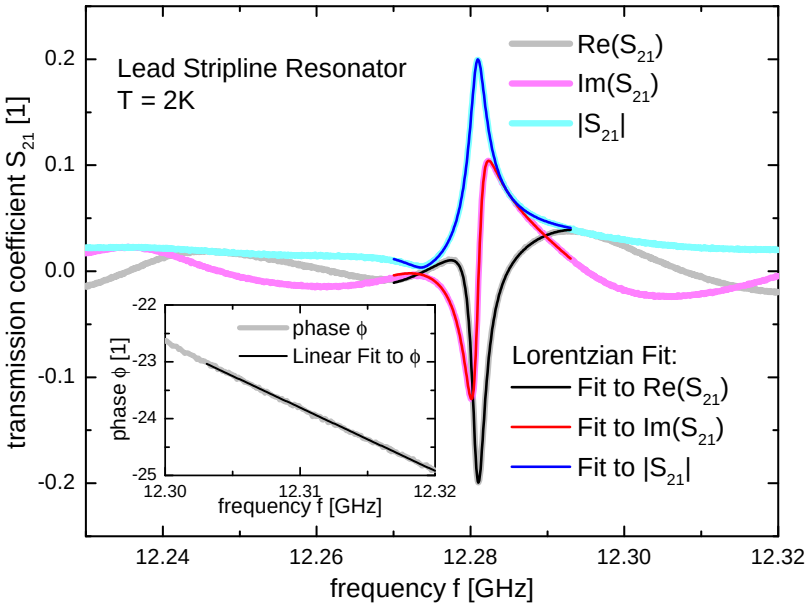

Fig. 3.3: The data shows the imaginary part $\mathrm{Im}(\hat{S}_{21})$, the real part $\mathrm{Re}(\hat{S}_{21})$ and the absolute value $|\hat{S}_{21}|$ of the transmission coefficient $\hat{S}_{21}$ near a resonance of a lead stripline resonator at $T = 2\,\mathrm{K}$. The fit to $\hat{S}_{21}$ is the complex Lorentzian fit in equation (3.12). The inset show a linear fit to the phase $\phi(f)$.

The cables add a global phase on the real and imaginary part of $\hat{S}_{21}$ that the coefficient τ accounts for.

The coefficient τ is determined by a linear fit on $\phi = \arctan\left[\mathrm{Im}(\hat{S}_{21})/\mathrm{Re}(\hat{S}_{21})\right]$ off-resonance. This can be seen in the inset in figure 3.3. In equation (3.12) the fitted value of τ is inserted and v_i are determined by fitting the real and imaginary part of $\hat{S}_{21}$ at resonance simultaneously. The resulting fit can be seen in figure 3.3.

3.4 Cavity perturbation technique

The resonance frequency f_0 and frequency bandwidth f_b allow to obtain the surface impedance $\hat{Z}_S = R_S + \mathrm{i}X_S$ in the superconducting state for different temperatures T and magnetic flux densities B. In this section the procedure for obtaining $\hat{Z}_S$ and the necessary assumptions are presented. Although the presented procedure makes no distinction between setup (a) and (b) in figure 3.2, it turns out that only for the Nb:$SrTiO_3$ samples in setup (b) the procedure is feasible. The procedure is applied respectively for one resonance.

The conductivity $\hat{\sigma}$ of an ideal s-wave superconductor is for frequencies $0\,\mathrm{GHz} < f \leq 2\Delta/h$ purely imaginary at $T = B = 0$. Under these circumstances in the local as well as in the non-local case it results in $R_S = 0$. The frequency bandwidth f_b accounts for losses due to the superconducting state of interest as well as residual losses. It is assumed that the residual losses show no T- and B-dependence. This assumption is reasonable since the losses are expected to occur due to the dielectric. In the present case the dielectric is sapphire

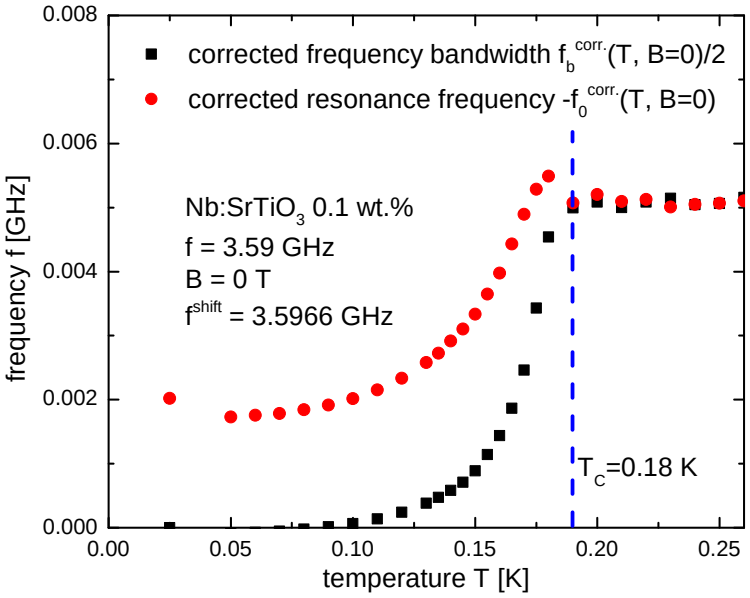

Fig. 3.4: Corrected resonance frequency $f_0^{\text{corr.}}$ and frequency bandwidth $f_b^{\text{corr.}}$ according to equation (3.16) and (3.13) for Nb:$SrTiO_3$ 0.1 wt.% in zero field $B = 0$ for frequency $f = 3.59\,\text{GHz}$.

which is a well established material in the operation of superconducting resonators and shows no unusual T or B dependencies in this regime [62]. A corrected frequency bandwidth is introduced

$$f_b^{\text{corr.}}(T, B) = f_b(T, B) - f_b(T = 0, B = 0). \tag{3.13}$$

In practice it is not possible to measure $f_b(T = 0, B = 0)$ since $T = 0$ is not achievable. Instead it suffices to correct f_b with the measured $f_b(T = T_{\text{low}}, B = 0)$ at the lowest achievable temperature T_{low}. Correcting with f_b measured at T_{low} suffices since σ_1 rises roughly exponentially with temperature T because the non-finite σ_1 is caused by quasi-particle excitations of the superconducting state.

The further procedure requires that f_0 and f_b are also measured in the normal state $T > T_C$ at $B = 0$. It is assumed that in the normal state $\hat{\sigma} = \sigma_{\text{DC}}$ is purely real, for low operating frequencies as in the microwave regime this is usually a good approximation. $\hat{\sigma} = \sigma_{\text{DC}}$ can be inserted into equation (2.30) and (2.31), as result it can be related in the normal conducting state

$$R_S = \alpha X_S \tag{3.14}$$

with $\alpha = 1$ in the local and $\alpha = 1/\sqrt{3}$ in the non-local limit. With equation (2.59) and for $B = 0$ it is possible to shift the resonance frequency f_0 to make a relation with $f_b^{\text{corr.}}$. A f^{shift} is introduced such that

$$\frac{1}{2} f_b^{\text{corr.}}(T > T_C, B = 0) = \alpha \left[-f_0(T > T_C, B = 0) + f^{\text{shift}} \right]. \tag{3.15}$$

The resonance frequency is then corrected

$$f_0^{\text{corr.}}(T,B) = f_0(T,B) - f^{\text{shift}}. \tag{3.16}$$

When a lead resonator with a Nb:$SrTiO_3$ sample as perturbation is measured, $f_b^{\text{corr.}}$ and $f_0^{\text{corr.}}$ still contain a B-dependence due to the lead. Lead shows in the temperature regime where Nb:$SrTiO_3$ is superconducting no temperature dependence, so it is assumed that the B-dependence of lead during the normal conducting state of Nb:$SrTiO_3$ is the same as in the superconducting state of Nb:$SrTiO_3$. A B-dependent quantity $\zeta_i(B)$ with $i = 1, 2$ is introduced such that

$$\begin{aligned} \frac{f_b^{\text{corr.}}(T > T_C, B)}{\zeta_1(B)} &= f_b^{\text{corr}}(T > T_C, B = 0), \\ \frac{f_0^{\text{corr.}}(T > T_C, B)}{\zeta_2(B)} &= f_0^{\text{corr}}(T > T_C, B = 0). \end{aligned} \tag{3.17}$$

The data is then corrected with $\zeta_i(B)$ for a last time

$$f_b^R(T,B) = \frac{f_b^{\text{corr.}}(T,B)}{\zeta_1(B)}, \qquad f_0^X(T,B) = \frac{f_0^{\text{corr.}}(T,B)}{\zeta_2(B)}. \tag{3.18}$$

The data can be finally related to a B- and T-dependent surface impedance of the sample of interest

$$\hat{Z}_S(T,B) = R_S(T,B) + \mathrm{i}X_S(T,B) = 2\Gamma\left(\frac{f_b^R(T,B)}{2} + \mathrm{i}f_0^X(T,B)\right). \tag{3.19}$$

With equation (2.30) and (2.31) the optical conductivity $\hat{\sigma}$ can then be obtained. The geometry coefficient Γ can be calculated numerically as it was done in subsection 3.2.2, but Γ can also be removed by a fitting normalization of the optical conductivity.

It is appropriate to mention a further assumption relevant for the case where Nb:$SrTiO_3$ acts as perturbation to the lead resonator. Using different metals with different surface impedance is expected to change the field configuration in the resonator. So a material as perturbation with a surface impedance that is similar to that of the resonator should be used. In that case it can be assumed that the field configuration changes only to a negligible extent. The total loss is then a superposition of the respective losses of the different materials. More details and experiments can be found in [21, 47, 55, 63–65].

4 Properties of Superconducting Stripline Resonators

4.1 Spectrum of the Stripline Resonator

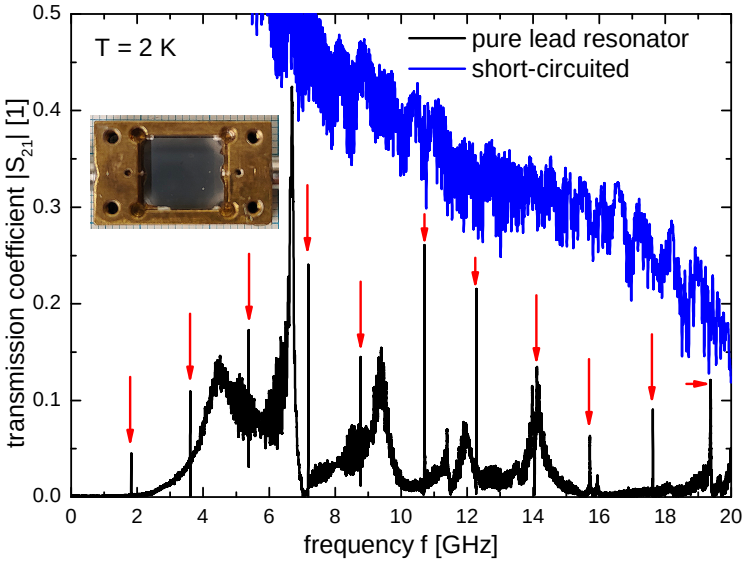

Fig. 4.1: Transmission coefficient $|S_{21}(f)|$ of a stripline resonator with all conductors made out of lead at $T = 2\,\mathrm{K}$. The transmission coefficient at the same temperature can be seen when the stripline resonator is replaced by an adaptor, this is labeled as short-circuited. The red arrows mark the equidistant resonances of the stripline resonator. The inset shows the view on the box and the upper lead ground plane.

In figure 4.1 the frequency dependence of the absolute value of the transmission coefficient $|S_{21}(f)|$ can be seen for a stripline resonator with all conductors made out of lead at $T = 2\,\mathrm{K}$. The transmission is close to zero for most frequencies except for the sharp peaks that are marked with a red arrow. The continuous development of $|S_{21}|$ in dependence of f is referred to as frequency background. The frequency background is different for every resonator and even changes slightly after heating up and cooling down. Due to the gaps in the stripline setup as it can be seen figure 3.2 it is expected that the transmission coefficient should be zero off-resonance. The non-finite frequency background is caused by small impedance mismatches and cavity resonances across the volume of the brass box that contains the stripline resonator. The red arrows mark the equidistant resonances, these are of Lorentzian shape and can be fitted with equation (3.12).

In figure 4.1 the transmission coefficient can be seen when the stripline resonator is replaced by an adaptor, this means when the setup is short-circuited. In that case the $|S_{21}|$ decreases with frequency due to absorption of the wiring, but $|S_{21}|$ for the short-circuited case is higher than for the resonator case for all frequencies.

4.2 Coupling coefficient

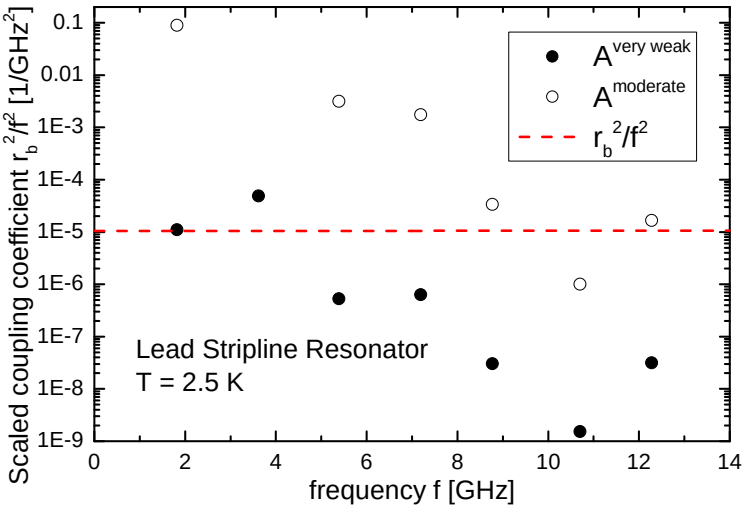

Fig. 4.2: Scaled coupling coefficient r_b^2/f^2 according to equation (3.9) with $A^{\text{very weak}}$ and A^{moderate} according to equation (4.5) and (4.6). Although $A^{\text{very weak}}$ and A^{moderate} vary a lot for different resonances, the trend from the very weak coupling to the moderate coupling regime can be seen. The resonances are the same as in figure 4.1.

In subsection 2.3.2 it is set $r_a = 0$ since it is $r_a \ll r_b$ according to equation (3.8) and (3.9) in the microwave regime. here it is further set $r_a = 0$ and the analysis will concentrate on the lead resonator whose resonances can be seen in figure 4.1. The quantity that is used to account for effects due to coupling is the coupling coefficient r_b. It is appropriate to calculate r_b according to equation (3.9) and to check it with the experimentally observed data. The most straightforward way is to take equation (2.53) at resonance, this means that $0 = \mathrm{d}\hat{S}_{21}(\delta\omega)/\mathrm{d}\delta\omega|_{\delta\omega=\delta\omega_C}$ must be fulfilled. It is obtained

$$|\hat{S}_{21}(\delta\omega = \delta\omega_C)| = \frac{2r_b^2}{\sqrt{4r_b^4\,(1+l\alpha)^2 + 4r_b^2\,(1+l\alpha) + (l\alpha)^2 - \frac{4r_b^2}{4r_b^2+1}}}. \tag{4.1}$$

with the frequency shift of the resonance frequency due to the coupling

$$\delta\omega_C = \frac{1}{l\sqrt{\epsilon\mu_0}}\frac{2r_b}{4r_b^4+1}. \tag{4.2}$$

It can be seen that the frequency shift in equation (4.2) simplifies in the weak coupling limit to (2.55).

A scaled coupling coefficient r_b/f is calculated according to equation (3.9). The obtained theoretical scaled coupling coefficient r_b/f varies from $0.00323\,\mathrm{GHz}^{-1}$ to $0.00328\,\mathrm{GHz}^{-1}$ for frequencies from 1 GHz to 20 GHz thus suggesting that the effects of coupling may be well approximated by using a frequency-independent coupling capacitance $C_b(f) = \text{const.}$. It is noted that in equation (3.9) the effective dielectric constant ϵ_r enters via the wavelength λ, thus for high ϵ_r materials the effects of coupling may not be appropriately taken care of by introducing a frequency-independent coupling capacitance. It is seen that up to 20 GHz it is $r_b^2 \ll 1$ thus the resonator is expected to be in the weak coupling regime over the considered frequency range. Therefore two coupling limits are considered, the very weak limit $r_b^2 < l\alpha$ and the moderate limit $l\alpha < r_b^2 < 1$.

The relations $\omega_0^* l\sqrt{\epsilon\mu_0} = \pi$ and $f_b\pi\sqrt{\epsilon\mu_0} = \alpha$ are used, it is noted that $l\alpha = f_b\pi^2/\omega_0^*$. ω_0^* is a quantity that is not experimentally accessible since the length l can't be determined with appropriate accuracy. With respect to equation (2.58) it can be argued that $\omega_0 \approx n\omega_0^*$ since r_b is sufficiently small and X_S of superconducting lead is known to disturb the resonance frequency only to a negligible extent [57]. So it is set $\omega_0^* \approx 2\pi f_0/n$ with integer mode number $n = 1, 2, 3, ...$ and as result it is obtained

$$|\hat{S}_{21}(\delta\omega = \delta\omega_C)|^{\text{very weak coupling}}_{\text{at resonance}} = \frac{4r_b^2 f_0}{\pi f_b n} \tag{4.3}$$

in the very weak coupling limit $r_b^2 < l\alpha$ and

$$|\hat{S}_{21}(\delta\omega = \delta\omega_C)|^{\text{moderate coupling}}_{\text{at resonance}} = \left(1 + \frac{\pi f_b n}{2f_0} + \frac{1}{2r_b^2}\right)^{-1} \tag{4.4}$$

in the moderate coupling limit $l\alpha < r_b^2 < 1$.

The quantities

$$A^{\text{very weak}} = |S_{21}(\delta\omega = \delta\omega_C)|\frac{\pi f_b n}{4f_0^3} \quad \text{very weak limit} \quad = \quad \frac{r_b^2}{f_0^2} \tag{4.5}$$

and

$$A^{\text{moderate}} = \left(2f_0^2\right)^{-1} \cdot \left(\frac{1}{|S_{21}(\delta\omega = \delta\omega_C)|} - \frac{\pi f_b n}{2f_0} - 1\right)^{-1} \quad \text{moderate limit} \quad = \quad \frac{r_b^2}{f_0^2} \tag{4.6}$$

are defined. $A^{\text{very weak}}$ and A^{moderate} are experimentally accessible quantities and are expected to equal r_b^2/f_0^2 in the respective weak and strong limit.

In figure 4.2 $A^{\text{very weak}}$ and A^{moderate} can be seen. The analysis features the resonances that can be seen in figure 4.1. The amplitudes $|S_{21}(\delta\omega = \delta\omega_C)|$ at resonance are scaled with respect to the short-circuited transmission line. The resonances do not show a continuous behavior for changing frequencies, in fact the resonances vary heavily even on the logarithmic scale. This is attributed to the finite frequency background that adds up an the actual

amplitude. Based on the comparison of the data with the dashed line a departure from the very weak coupling limit to the moderate coupling limit for greater frequencies can be observed as trend. This results from the linear f dependence of r_b.

4.3 Geometry factor

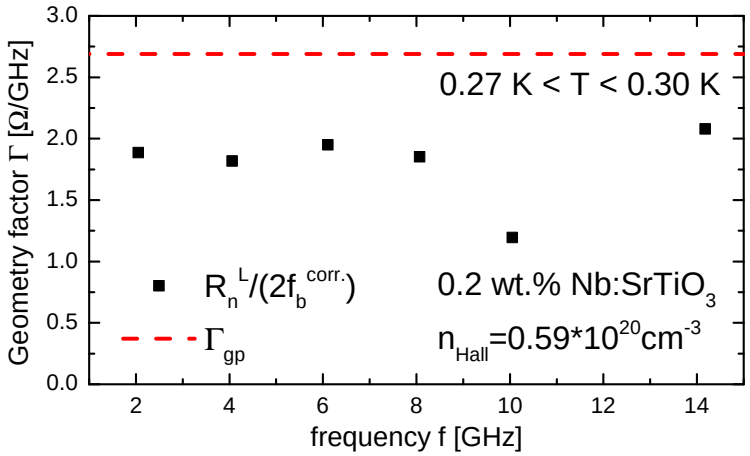

Fig. 4.3: Geometry factor $\Gamma_{gp} = 2.69\,\Omega/\mathrm{GHz}$ as calculated in equation (3.4) with the normal phase surface resistance divided by the corrected bandwidth $R_n^L/(2f_b^{\mathrm{corr.}})$.

The geometry factor Γ describes how the frequency bandwidth and the surface resistance are related. Although Γ may be discarded when normalizing the optical conductivity and surface impedance data, it is appealing to compare the theoretically expected values with the experimental results. There are two approaches to compute Γ. One approach features the calculation of the contour integrals of the stripline setup, this is the path that was chosen in subsection 3.2.2. Another approach is to calculate Γ with the help of a variational principle from the circuit impedance Z_C [57, 66]. Both approaches return the same Γ_{cc} for $w \geq 4h$ and Γ_{gp} regardless of the choice of w and h. It is assumed that the variational principle treats the edge of the center conductor in a simplified way thus resulting in a different Γ compared to the one that is obtained from a direct evaluation of the contour integrals. Therefore the values for Γ that are obtained in 3.2.2 are used.

Experimental values for Γ can be obtained by considering f_b of the normal conducting phase in Nb:$SrTiO_3$. In this section it is focused on the geometry factor of the upper ground plane $2\Gamma_{gp}$. It can be related

$$2\Gamma_{gp} f_b^{\mathrm{corr.}} = R_n^L = \sqrt{\frac{\pi f_0 \mu_0}{\sigma_{\mathrm{DC}}}}. \tag{4.7}$$

The bandwidth is corrected according to section 3.4 to obtain $f_b^{\mathrm{corr.}}$. The surface resistance of the normal conducting phase in the dirty limit R_n^L is used. The discussion whether the

dirty limit is appropriate for Nb:$SrTiO_3$ is forwarded to the next chapter. The DC resistance $\rho_{DC} = 1/\sigma_{DC}$ of 0.2 wt.% Nb:$SrTiO_3$ is given by $\rho_{DC}(0.2\text{ wt.\% Nb:SrTiO}_3) = 0.57\,\mu\Omega\text{m}$ [17].

In figure 4.3 the theoretical value of $\Gamma_{gp} = 2.69\,\Omega/\text{GHz}$ together with the quantity $R_n^L/(2f_b^{\text{corr.}})$ that is expected to equal Γ_{gp} can be seen. The quantity $R_n^L/(2f_b^{\text{corr.}})$ is in the same order of magnitude as Γ_{gp} but substantially lower. The deviation is most likely a result from the uncertainties of the dimensions of the stripline setup. It is noteworthy that the respective points of $R_n^L/(2f_b^{\text{corr.}})$ deviate among each other less than with the theoretically expected Γ_{gp}. This suggests that the real Γ_{gp} does not vary for different resonances as it is the case for the scaled coupling coefficient r_b^2/f^2 in the previous section.

4.4 Effective London penetration depth

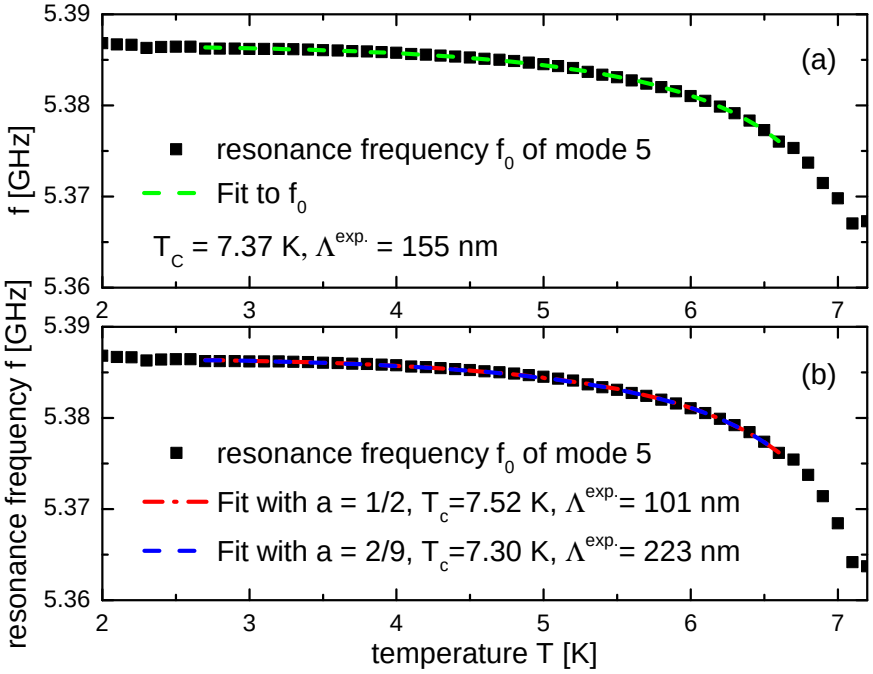

Fig. 4.4: In (a) a fit of equation (4.10) to the resonance frequency $f_0(T)$ of a pure lead stripline resonator can be seen with the corresponding fitting values. In (b) the same fit can be seen but a different temperature scaling coefficient a was assumed.

	$\lambda_L^{\text{lit.}}$	$\xi_\Delta^{\text{lit.}}$	$l^{\text{lit.}}$	$\lambda_{\text{eff}}^{\text{lit.}}$	$\Lambda^{\text{lit.}}$
Pb	38 nm [47]	83 nm [47]	200 nm [47]	49 nm	99 nm
Sn	34 nm [67]	230 nm [67]	17-56 µm [68–70]	64 nm	518-771 nm

Tab. 4.1: Literature values of $\lambda_L^{\text{lit.}}$, $\xi_\Delta^{\text{lit.}}$ and $l^{\text{lit.}}$ with the respective sources at $T = 0$. For both clean type I superconductors $\lambda_{\text{eff}}^{\text{lit.}}$ is given by equation (2.29) and $\Lambda^{\text{lit.}}$ by equation (4.13).

mode	1	2	3	4	5	6	7
$\Lambda^{\text{exp.}}$ of Pb [nm]	158	157	155	162	162	135	143
$T_C^{\text{exp.}}$ of Pb [K]	7.38	7.36	7.37	7.43	7.49	7.27	7.34
$\Lambda^{\text{exp.}}$ of Sn [nm]	511	424	(1119)	(1587)	(920)		
$T_C^{\text{exp.}}$ of Sn [K]	3.83	3.87	(4.88)	(5.19)	(4.73)		

Tab. 4.2: Obtained experimental data by fitting equation (4.10) to $f_0(T)$ of a pure lead and tin stripline resonator. Values for $\Lambda^{\text{exp.}}$ are at $T = 0$. An exemplary fit can be seen in figure 4.4 in (a) for mode 3.

Hafner *et al.* showed that the frequency shift in a superconducting resonator can be related to the temperature dependence of the effective London penetration depth $\lambda_{\text{eff}}(T)$ [57]. Nevertheless fitting absolute values of the effective London penetration depth could not be obtained. In this section this issue is investigated in greater detail. This issue is of interest since the superconducting state in [57] was investigated without making assumptions about the normal state conductivity as required in the cavity perturbation technique.

For low frequencies $hf/(2\Delta) < 1$ it is $\sigma_2 > \sigma_1$ in a superconductor [21]. Then it is appropriate to set

$$\hat{\sigma} \approx i\sigma_2 = i\frac{1}{2\pi\mu_0\lambda_{\text{eff}}^2 f}. \tag{4.8}$$

The expression of $\hat{\sigma}$ is the same for London- and Pippard superconductors [21, 47]. With equation (2.59) and $\omega_0^* = 2\pi f_0^*$ the frequency shift of the resonator can be evaluated and is given in the London case with equation (2.30) by

$$f_0 = nf_0^*\left(1 + \frac{\mu_0\pi\lambda_{\text{eff}}}{\Gamma}\right)^{-1} \approx \frac{nf_0^*}{\sqrt{1 + \frac{2\mu_0\pi\lambda_{\text{eff}}}{\Gamma}}} \tag{4.9}$$

and in the Pippard case with equation (2.31) by

$$f_0 = nf_0^*\left(1 + \frac{\mu_0\pi(2l\lambda_{\text{eff}}^2)^{1/3}}{\Gamma}\right)^{-1} \approx \frac{nf_0^*}{\sqrt{1 + \frac{2\mu_0\pi(2l\lambda_{\text{eff}}^2)^{1/3}}{\Gamma}}}. \tag{4.10}$$

Equation (4.9) was derived by Hafner and is equivalent to equation (15) in [57] except the additional factor 2. Hafner's derivation is based on the analysis of the skin effect in the normal state by Wheeler where the skin depth was replaced by $\delta_S \to \lambda_{\text{eff}}$ [71]. In fact the phase orientation of the complex superconducting $\hat{\sigma}$, that is imaginary compared to the normal conductivity σ_{DC} that is real in the microwave regime, suggests $\delta_S \to 2\lambda_{\text{eff}}$ [21]. It is also noted that it is more appropriate to use equation (4.10) to analyze the frequency shift of lead and tin since both materials are non-local superconductors [47, 68–70].

The temperature dependence of λ_{eff} is a delicate topic since $\lambda_L(T)$ contributes to λ_{eff} in different limits and a superconductor may even switch from the non-local to the local limit when $\lambda_L(T) > \xi_\Delta$. In the non-local limit it can be related

$$\frac{\lambda_{\text{eff}}(T)}{\lambda_{\text{eff}}(T=0)} = \left[\frac{\Delta(T)}{\Delta(T=0)} \tanh \frac{\beta\Delta(T)}{2}\right] \approx \frac{1}{\sqrt{1-(T/T_C)^4}} \tag{4.11}$$

whereas the approximation holds better at lower temperatures than close to T_C [33]. It is appropriate to consider at which temperature the non-local behavior switches to a local behavior. Close to T_C it is $(\lambda_L(0)/\lambda_L(T))^2 \approx 1-(T/T_C)^2$ [33]. The transition temperature between the local and non-local regime $T_{\text{n-nl}}$ is then given by

$$T_{\text{n-nl}} = T_C \sqrt{1-\left(\frac{\lambda_L(T=0)}{\xi_\Delta}\right)^2}, \tag{4.12}$$

with the values from table 4.1 it is obtained $T^{\text{transition}}(\text{Pb}) = 0.89\,T_C$ and $T^{\text{transition}}(\text{Sn}) = 0.99\,T_C$. The fit in equation (4.10) will only extend up to these temperatures.

The literature values are listed in table 4.1. For the comparison of literature and experimental data the length scale

$$\Lambda = \left(2l\lambda_{\text{eff}}^2\right)^{\frac{1}{3}} \tag{4.13}$$

with a temperature dependence

$$\Lambda(T) = \Lambda(T=0) \cdot \left[1-\left(\frac{T}{T_C}\right)^4\right]^{-\frac{1}{3}} \tag{4.14}$$

is introduced. In subsection 3.2.2 the geometry coefficient $\Gamma^{-1} = \Gamma_{cc}^{-1} + \Gamma_{gp}^{-1}$ is computed, it is given by $\Gamma = 0.129\,\Omega/\text{GHz}$. The geometry coefficient is necessary to compute Λ.

In table 4.2 the obtained $\Lambda^{\text{exp.}}$ and $T_C^{\text{exp.}}$ from using equation (4.10) as fit to $f_0(T)$ for the pure lead and tin resonator can be seen. The values in brackets follow from a questionable fit and are only mentioned for completeness. The expected critical temperature is for lead $T_C = 7.2\,\text{K}$ and for tin $T_C = 3.7\,\text{K}$ [72], the literature values are close to the experimental values although the expected T_C is lower than the obtained T_C. The obtained $\Lambda^{\text{exp.}}$ in the case of lead do not differ substantially for different modes as it is expected since the frequency does not enter in the denominator of equation (4.10). $\Lambda^{\text{exp.}}$ of lead is about $\sim$1.5 times greater than the expected value, this is attributed to a simplified temperature dependence as taken in equation (4.14) and the geometry factor Γ that is a difficult to obtain with a theoretical scheme. It is noteworthy that for a smaller theoretical obtained Γ the data of the previous section as it can be seen in figure 4.3 and the value of $\Lambda^{\text{exp.}}$ and $\Lambda^{\text{lit.}}$ would show more accordance whereas caution is appropriate since in figure 4.3 it was investigated on Γ_{gp} but the geometry factor in this section is dominated by $\Gamma \approx \Gamma_{cc}$. The data on tin is somewhat ambiguous, but it can be seen that there is also some accordance between $\Lambda^{\text{lit.}}$ and $\Lambda^{\text{exp.}}$.

It is important to discuss the role of the temperature scaling on the results of the fit. In figure 4.4 in (a) a fit of equation (4.10) with the temperature scaling as in (4.14) can be seen.

The temperature scaling exponent a is introduced that is in equation (4.14) $a = 1/3$. If one would assume the two fluid model e.q. $\lambda_L \approx (1 - (T/T_C)^4)^{1/2}$ [33] with the respective limits as discussed in subsection 2.2.4 then an $a = 1/2$ in the local limit and an $a = 2/9$ in the non-local limit would be obtained. In figure 4.4 in (b) the resulting fitting values can be seen. It becomes apparent that the fits seem to match nicely but the values differ in a relatively broad way. Thus there is a considerable risk in obtaining wrong values for T_C and Λ.

5 Nb:$SrTiO_3$ in magnetic field

5.1 Introduction to $SrTiO_3$

5.1.1 Properties of $SrTiO_3$

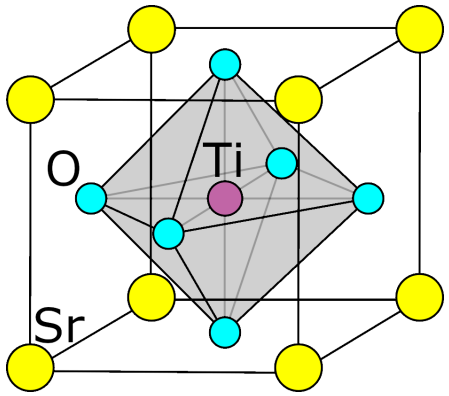

Fig. 5.1: Schematic depiction of the crystal structure of $SrTiO_3$, illustrative for the perovskite structure.

$SrTiO_3$ is a semiconductor with a perovskite structure that has an energy gap of 3.22 eV [73], a schematic depiction of the crystal structure can be seen in figure 5.1. At room temperature $SrTiO_3$ is a transparent insulator with a relatively high dielectric constant of $\epsilon_r \sim 300$. Upon cooling down, ϵ_r rises according to the Curie-Weiss law

$$\epsilon_r \propto (T - T_{\text{Curie}})^{-1} \tag{5.1}$$

with the Curie temperature T_{Curie}. This behavior is observed down to roughly $T = 65\,\text{K}$ [74]. $SrTiO_3$ does not undergo a transition to a ferroelectric state whereas other compounds with the perovskite structure turn to a ferroelectric state. A ferroelectric is a material that has below T_{Curie} a finite nonvanishing dipole moment even in absence of an external electric field [40].

Instead ϵ_r of $SrTiO_3$ levels of at $\epsilon_r \sim 20000$ due to the stabilization by quantum fluctuations in the paraelectric phase [5]. $SrTiO_3$ is thus referred to as quantum paraelectric. A paraelectric is in analogy to a paramagnet a material with $\epsilon_r > 1$ but without spontaneous polarization.

When introducing charge carriers in $SrTiO_3$ by substituting titanium with niobium or reducing oxygen, $SrTiO_3$ becomes conducting and superconducting below T_C for sufficient doping. As already mentioned in the motivation, superconducting $SrTiO_3$ exhibits multiband

superconductivity [2] and a superconducting dome of T_C in dependence of the charge carrier density n [3, 75]. Superconducting Nb:$SrTiO_3$ is a type II superconductor [19]. Reduced $SrTiO_3$ was shown to exhibit superconductivity down to a very low charge carrier density of $n = 5.5 \cdot 10^{17}\,\mathrm{cm}^{-3}$ [76]. As result the ratio of the Debye frequency to Fermi Energy is in the range of $\hbar\omega_D/E_F \sim 1$ for different doping n [77]. Since the BCS theory requires the smallness of $\hbar\omega_D/E_F \ll 1$, many early attempts to derive the dome of $T_C(n)$ from first hand principles were not appropriate [77].

Today $SrTiO_3$ is known as challenging material for fundamental research. The high ϵ_r, the absence of a transition to a ferroelectric state, the superconducting dome, the small E_F and the relation of these aspects to each other alongside with the three relevant electronic bands and the anisotropic Fermi surface of this compound pose a challenge to the modern research. In this subsection only an introduction into the essential aspects is given, a review on the experimental [8] and theoretical [9] side explore the topic in more detail.

5.1.2 Discussion of recent findings

Undoped $SrTiO_3$

Rowley *et al.* published a paper on the dielectric constant of critical quantum paraelectrics such as undoped $SrTiO_3$, O^{18} substituted $SrTiO_3$ and $KTaO_3$ [6]. Their approach uses the ϕ^4-theory. It is often appropriate to assume an interaction up to fourth order of an order parameter ϕ. The interaction is expressed as Ginzburg-Landau free energy functional

$$S[\phi] = \int \mathrm{d}^d x \left(\frac{1}{2} (\nabla\phi)^2 + \frac{r}{2}\phi^2 + g\phi^4 \right) \tag{5.2}$$

with parameters r and g and inserted into the field integral

$$\mathcal{Z} = \int \mathrm{D}\phi\, e^{-S[\phi]} \tag{5.3}$$

to define the partition function $\mathcal{Z}$. Perturbation schemes may be readily employed when an interaction can be brought into the form (5.2) as it is the case for the Ising model [38]. In the case of a critical quantum paraelectric the relation

$$\epsilon_0 E = aP + bP^3 - c\nabla^2 P \tag{5.4}$$

between E and the electric polarization P is introduced. The parameters are the inverse static susceptibility a, the mode-mode coupling parameter b and the mode stiffness parameter c. It can be readily seen that an expression of the type in equation (5.4) follows when setting the variation of equation (5.2) to $\delta S[\phi] = 0$.

The parameter a, b and c are determined experimentally. When plotting $\epsilon_r E/P$ vs P^2 a and b can be determined from the intercept with the $\epsilon_r E/P$-axis and slope. The parameter c is obtained from inelastic neutron and Raman scattering. The driving force behind the quantum fluctuations of the polarization is assumed to be of Langevin type, this way the variance of P can be related to the dielectric constant via the fluctuation-dissipation theorem.

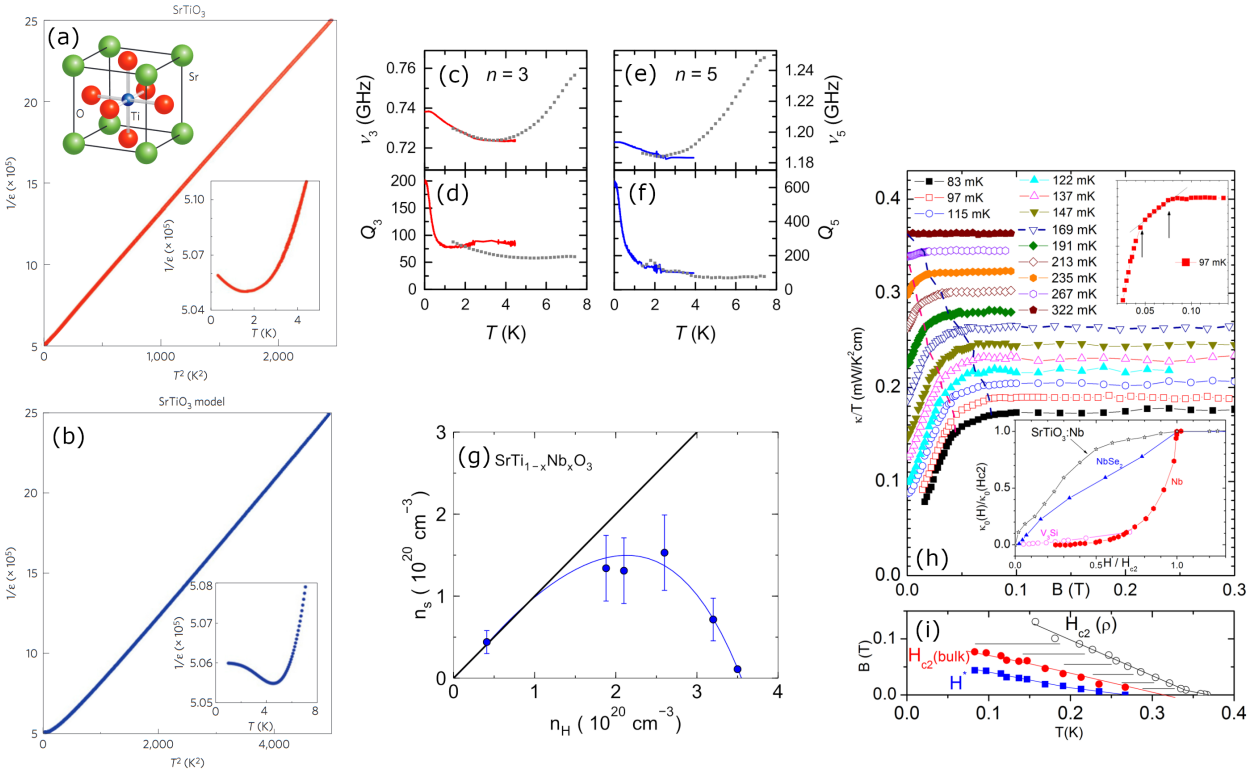

Fig. 5.2: In (a) and (b) the experimentally obtained inverse dielectric constant $1/\epsilon_r$ of undoped $SrTiO_3$ and the theoretical model as described in the main text for $1/\epsilon_r$ can be seen, data taken from [6]. In (c) and (e) the resonance frequency $\nu \propto \epsilon_r^{-1/2}$ and in (d) and (f) the quality factor $Q = f_b/f_0$ of a superconducting microwave resonator operating on an undoped $SrTiO_3$ substrate can be seen, data taken from [7]. In (g) the superfluid density n_{sc} of Nb:$SrTiO_3$ for different dopings with the Hall charge carrier concentration n_H can be seen, the departure of n_{sc} from n_H suggests a transition from the clean to the dirty limit, data taken from [19]. In (h) the thermal conductivity κ of Nb:$SrTiO_3$ is shown in dependence of B for different T with two visible kinks that relate to two bands, the inset makes a comparison with other superconductors. (i) shows the extracted magnetic field B^* from the first kind and B_{C2} extracted from the thermal conductivity and resistivity measurements. (h) and (i) is taken from [16].

As result the dielectric constant can be obtained and the temperature dependence enters the dielectric constant via the fluctuation-dissipation theorem.

In figure 5.2 in (a) and (b) the experimentally obtained inverse dielectric constant $1/\epsilon_r$ and the theoretical model as just described in a simplified manner for $1/\epsilon_r$ can be seen. The non-classical T^2 behavior follows from the quantum criticality model.

Engl *et al.* fabricated a superconducting microwave resonator on an undoped $SrTiO_3$ substrate [7, 78]. To overcome the impedance mismatch due to the high ϵ_r of $SrTiO_3$ the distant-flip-geometry is used [79]. In figure 5.2 in (c) and (e) the resonance frequency $\nu \propto \epsilon_r^{-1/2}$ and in (d) and (f) the quality factor $Q = f_b/f_0$ can be seen for the resonator modes $n = 3, 5$. Towards the mK regime a steep rise of Q can be observed for the $SrTiO_3$ microwave resonator. The dielectric constant is a non-monotonous function of temperature $\epsilon_r(T)$. The inverse dielectric function in (c) and (e) shows a minimum at 2 to 4 K and in (c) a small but significant maximum at around 0.2 K. The behavior of ϵ_r in the microwave regime in the mK regime challenges the understanding of the dielectric properties.

Doped $SrTiO_3$

Many recent findings were published by the group of Kamran Behnia. Lin *et al.* measured in reduced $SrTiO_3$ at a doping of $n = 5.5 \cdot 10^{17}\,\mathrm{cm}^{-3}$ superconductivity at a barely anisotropic Fermi surface with $E_F = 1.1\,\mathrm{meV}$ [76]. By Shubnikov-deHaas measurements two critical dopings $n_{C1} = 1.2 \cdot 10^{18}\,\mathrm{cm}^{-3}$ and $n_{C2} = 1.6 \cdot 10^{20}\,\mathrm{cm}^{-3}$ were found, at n_{C1} superconducting $SrTiO_3$ turns from a single-band to a two-band superconductor [80]. The DC resistivity ρ_{DC} of normal conducting $SrTiO_3$ was shown to have a T^2 behavior

$$\rho_{\mathrm{DC}} = \rho_0 + AT^2 \tag{5.5}$$

with resisitivity coefficient ρ_0, the prefactor A changes in four orders of magnitude for different doping n [81]. Van der Marel *et al.* published a theoretical investigation on the T^2 resistivity term and computed the Fermi energy in dependence of doping $E_F(n)$ [82].

T_C of superconducting Nb:$SrTiO_3$ with $n = 2.1 \cdot 10^{20}\,\mathrm{cm}^{-3}$ was shown not to change significantly when point defects are introduced by electron irradiation, alongside the thermal conductivity data that suggests the absence of nodal particles it was deduced that $SrTiO_3$ is a multigap s-wave superconductor [16, 83]. The thermal conductivity data can be seen in figure 5.2 in (h) and (i), in (h) the thermal conductivity κ of Nb:$SrTiO_3$ is shown in dependence of B for different T with two visible kinks that relate to two bands whereas the inset makes a comparison with other superconductors. (i) shows the extracted magnetic field B^* from the first kink and B_{C2} extracted from the thermal conductivity and resistivity measurements. It is seen that the thermal conductivity and resistivity data suggest a slightly different T_C in optimally doped Nb:$SrTiO_3$.

Nb:$SrTiO_3$ was shown to undergo a transition from a clean to a dirty superconductor for greater doping [19]. This can be seen in figure 5.2 in (g), the departure of the superfluid density n_{sc} from the measured Hall charge carrier concentration $n_H = n_{\mathrm{Hall}}$ suggests a transition from the clean to the dirty regime. Thiemann *et al.* measured the complex $\hat{\sigma}$ of Nb:$SrTiO_3$ and observed single-gap multi-band superconductivity in the dirty limit, they

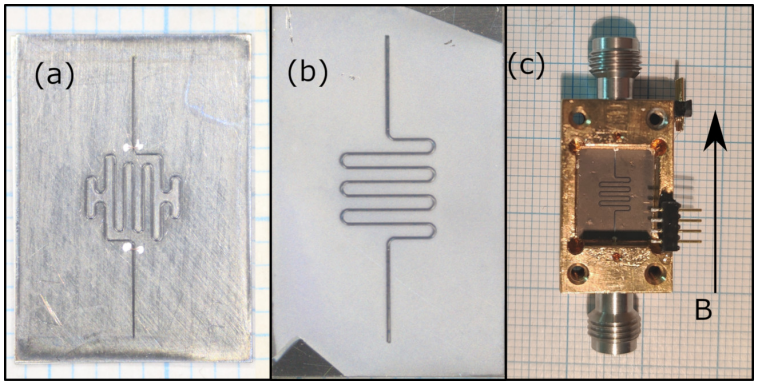

Fig. 5.3: In (a) the mask for the parallel (||) setup and in (b) the mask for the perpendicular ($\perp$) setup can be seen. In (c) the center conductor for the $\perp$-setup is visible. The arrow marks the direction of the applied B.

Nb doping [wt. %]	T_C [K]	ρ_{DC} [$\mu\Omega$m]	n_{Hall} [$10^{20}\,cm^{-3}$]	μ [cm^2/Vs]	measured in || orientation	measured in $\perp$ orientation
0.1	0.168	0.58	0.33	3300	Beydeda	
0.2	0.254	0.57	0.59	1800	Thiemann	Beydeda
0.35	0.346	0.52	1.1	1100	Thiemann Zinßer	
0.5	0.278	0.42	2.0	800	Thiemann	
0.7	0.213	0.56	2.2	500	Beydeda	

Tab. 5.1: Available samples with doping concentrations, T_C, DC resistivity ρ_{DC}, charge carrier concentration determined from Hall measurements n_{Hall} and mobility μ. The samples have either size $5 \times 5 \times 1\,mm^3$ or $5 \times 5 \times 0.5\,mm^3$. The last two columns list in which orientation the samples were measured, the respective data can be found in [88, 89] and this thesis. Values are taken from [17].

tracked the energy gap $\Delta(T)$ and showed that Nb:$SrTiO_3$ fulfills Homes' law, in addition they observed the same kinks in the B dependence as Lin *et al.* [16, 17, 84].

Measurements of the resistivity of normal conducting Nb:$SrTiO_3$ suggests a temperature dependent effective mass [85]. Large magnetoresistance in lightly doped reduced $SrTiO_3$ was found, the resistivity increases 40 times at $B = 54\,T$ [86]. Stucky *et al.* observed a strong isotope effect with opposite sign compared to the usual isotope effect of conventional superconductivity [87]. The conventional isotope effect $T_C \propto M^{-\alpha}$ with exponent $\alpha = 1/2$ was shown to differ for many conventional element superconductors and the solution to the slightly different α often confirmed the BCS theory, but in the case of $SrTiO_3$ the strong enhancement of T_C hints to a new kind of attractive interaction [29, 33].

5.1.3 Nb:$SrTiO_3$ samples

The Nb:$SrTiO_3$ samples in this thesis are listed in table 5.1, a Nb:$SrTiO_3$ sample is considered as measured when the B and T dependence of the optical conductivity $\hat{\sigma}$ is obtained. The stripline configuration can be seen in figure 3.2 in (b), the optical conductivity is obtained with the cavity perturbation technique. In figure 5.3 two different mask designs for the center conductor that were used in this thesis can be seen. Depending on the mask most of the center conductor will be orientated parallel ($\|$) or perpendicular ($\perp$) to the external magnetic flux density B, those cases will be referred to as $\|$- and $\perp$-setup.

It is of worth to note that a dirty normal conductor is characterized by $\delta_S/l > 1$ in contrast to a dirty superconductor $\xi_\Delta/l > 1$ whereas δ_S is the skin depth. Using [21]

$$\delta_S = \sqrt{\frac{2\rho_{\mathrm{DC}}}{\omega\mu_0}} \tag{5.6}$$

$\delta_S > 1\,\mu$m for the samples in table 5.1 for frequencies below $\omega < 2\pi \cdot 20\,\mathrm{GHz}$ is obtained. This is considerably larger than the free mean path l [88]. A dirty conductor can be described with the Drude model [21]

$$\hat{\sigma} = \sigma_{\mathrm{DC}} \frac{1}{1 - \mathrm{i}\omega/\Gamma_{\mathrm{scat.}}} \tag{5.7}$$

with the scattering rate $\Gamma_{\mathrm{scat.}}$. The mobility is defined as $\mu = e/\left(\Gamma_{\mathrm{scat.}} m\right)$ with effective mass m [40]. An upper bound for the effective mass $m = 4.2\,m_e$ [80] and mobility is taken to obtain a lower limit for $\Gamma_{\mathrm{scat.}} = 2\pi \cdot 20\,\mathrm{GHz}$. As result the operating frequency should be lower than $f < 20\,\mathrm{GHz}$ to reasonably apply Cavity perturbation technique.

5.2 Optical conductivity $\hat{\sigma}$ in $\|$-orientation

5.2.1 Sample with 0.1 wt. % Nb doping

The optical conductivity $\hat{\sigma}$ in $\|$-orientation was obtained in dependence of the magnetic flux density $B = |\vec{B}|$ at multiple T. After sweeping B at one finite T, it was set $B = 0$ and the sample was heated above $T > T_C(\mathrm{Nb{:}SrTiO_3})$ and cooled down again before the next B-sweep was executed for one next T. The zero-field cooling was performed to prevent hysteresis effects of Nb:$SrTiO_3$. The magnetic flux density was never swept above the critical field of lead $B_C \approx 80\,\mathrm{mT}$ to prevent hysteresis effects due to lead [90].

In figure 5.4 and 5.5 the optical conductivity of the 0.1 wt. % Nb-doped $SrTiO_3$ sample can be seen for frequencies $f = 3.59\,\mathrm{GHz}$, $f = 10.59\,\mathrm{GHz}$ in $\|$ orientation. In both figures a kink in the B-dependence of σ_1, σ_2 can be seen as abrupt change of the slope. The same kink shows up in the thermal conductivity data in figure 5.2 in (h), the respective magnetic flux density is labeled B^*. A better view on the kink can be seen in figure 5.6 in (b) and (c). In the analysis of Thiemann and Zinßer the kink is attributed to the partial filling of three bands whereas two of the bands have the same effective mass [17, 88, 89]. In that sense B^* is the upper critical field of the charge carriers with effective mass $m = 1.5\,m_e$ and B_{C2}

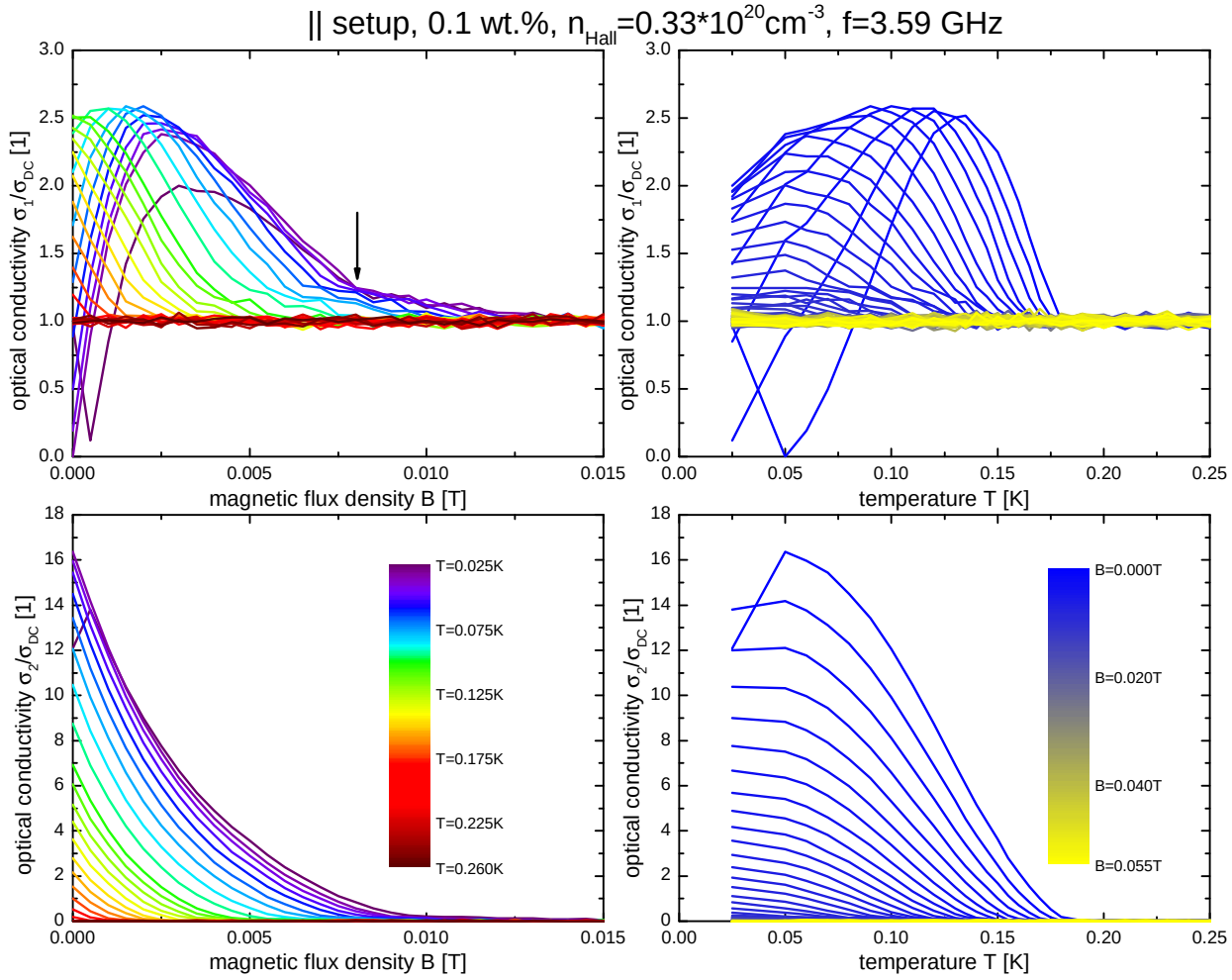

Fig. 5.4: Optical conductivity of the 0.1 wt. % Nb-doped $SrTiO_3$ sample at $f = 3.59\,\mathrm{GHz}$ in || orientation. The arrow marks the kink at B^* for lowest temperature.

corresponds to $m = 4.2\,m_e$, the values for the effective masses are obtained from quantum oscillation measurements [17, 80].

The values for B^* and B_{C2} are obtained by linear fits at $\sigma_i(B)$, $i = 1, 2$ before and after the kink e.g. for $B < B^*$ and $B > B^*$. Exemplary fits can be seen in figure 5.6 in (b) and (c). From the intercept of both fits B^* is obtained. B_{C2} is obtained from the intercept of the fit for $B > B^*$ with $\sigma_1/\sigma_{\mathrm{DC}} = 1$ and $\sigma_2/\sigma_{\mathrm{DC}} = 0$. The temperature dependent $B^*(T)$, $B_{C2}(T)$ can be fitted with

$$\frac{B_C(T)}{B_C(T=0)} = 1 - \left(\frac{T}{T_C}\right)^2 \tag{5.8}$$

to obtain $B^*(T=0) = 9.0\,\mathrm{mT}$, $B_{C2}(T=0) = 15.1\,\mathrm{mT}$ [33]. Equation (5.8) as fit can be seen in figure 5.6 in (a).

The field configuration in the stripline setup induces a current $\vec{J}_{\mathrm{ind.}}$ in the Nb:$SrTiO_3$ sample, it is $\vec{J}_{\mathrm{ind}} || \vec{B}$ since most of the center conductor is oriented parallel to $\vec{B}$. Thus no

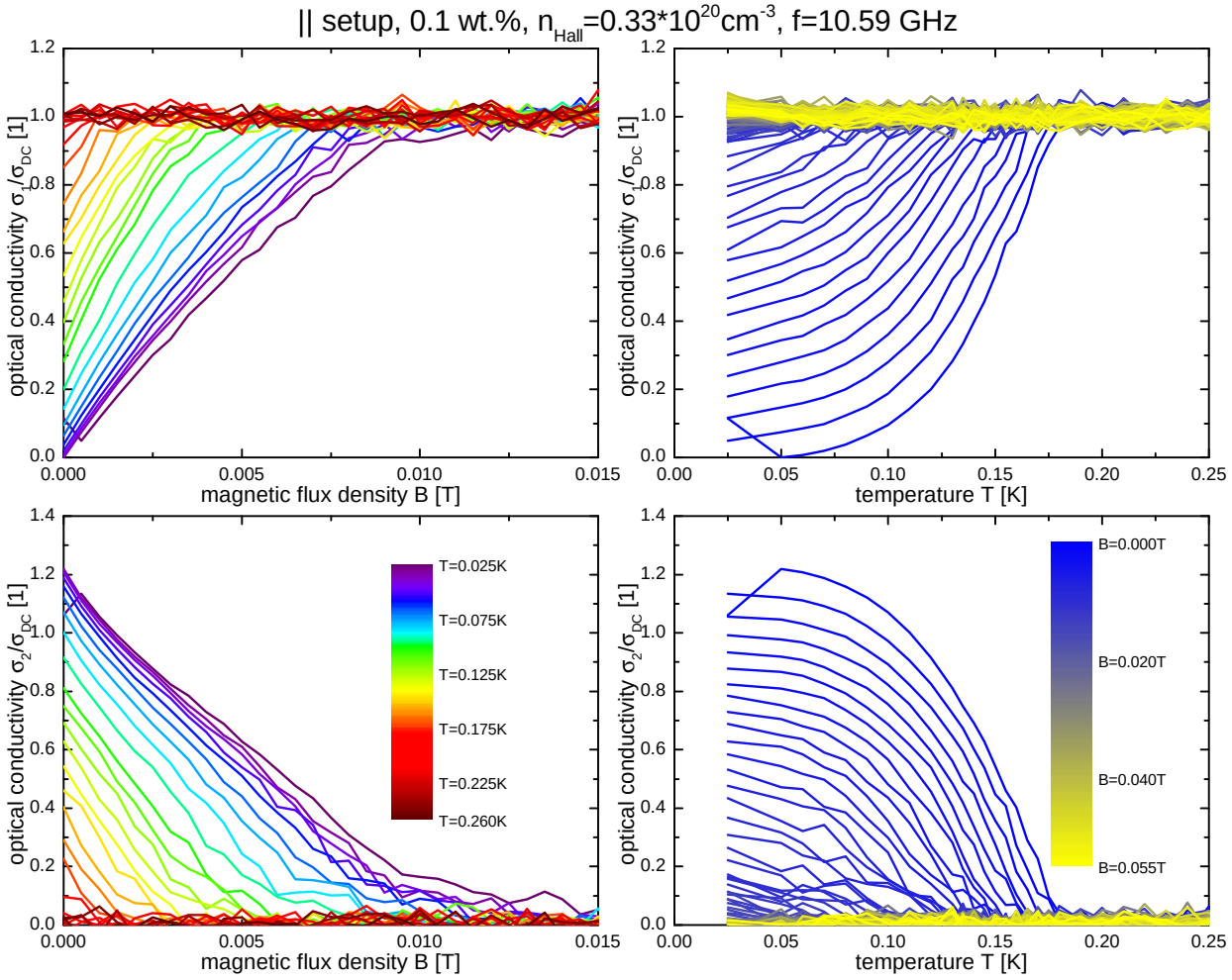

Fig. 5.5: Optical conductivity of the 0.1 wt. % Nb-doped $SrTiO_3$ sample at $f = 10.59\,\mathrm{GHz}$ in || orientation.

Lorentz force acts as driving force on the trapped flux quanta of the vortices [33]. In the Bardeen-Stephen model vortices are assumed to be normal conducting cylinders with finite radius ξ_{GL} [91]. Turning back to Nb:$SrTiO_3$, the two critical fields are related to two GL coherence lengths ξ^l_{GL}, ξ^m_{GL} according to equation (2.39). In this framework the kink in slope occurs naturally when it is $a_\Delta(B^*) = 2\xi^m_{\mathrm{GL}}$ since one band turns normal conducting. The distance between two vortices a_Δ is given by (2.38). In figure 5.6 in (a) a schematic depiction of the described situation can be seen. In table 5.2 the values for $\xi^{l,m}_{\mathrm{GL}}$ can be seen.

The perhaps most puzzling feature is the coherence peak like maximum of $\sigma_1(B) > \sigma_{\mathrm{DC}}$ as it can be seen in figure 5.4. It is appropriate to make a distinction between the usual coherence peak, that is now referred to as T-coherence peak and the B-coherence peak. The T-coherence peak was predicted by the BCS theory and can be reproduced with the Mattis-Bardeen equation (2.26). The T-coherence peak results from the density of states that diverges at $E = \pm\Delta$ as it can be seen in figure 2.1, for low frequencies $hf/(2\Delta_0) < 1$ and close to T_C excitations in the divergence cause $\sigma_1 > \sigma_{\mathrm{DC}}$. The T-coherence peak can

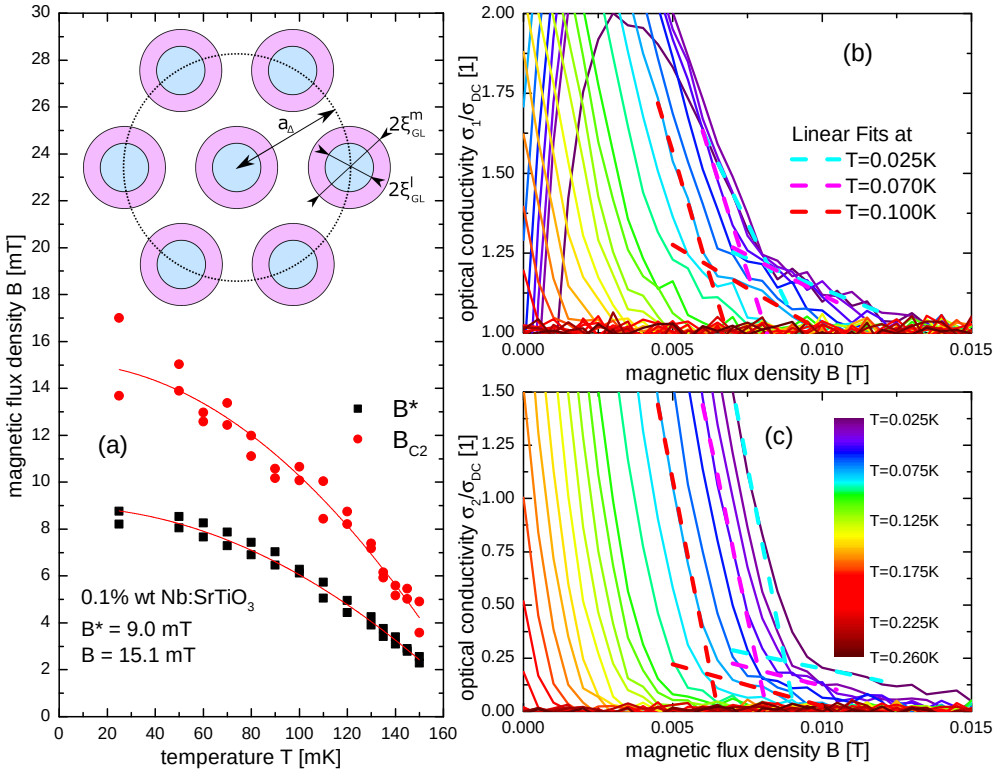

Fig. 5.6: In (a) the critical magnetic flux densities B^* and B_{C2} with a fit according to equation (5.8) can be seen. In (b) and (c) linear fits to the optical conductivity from figure 5.4 ($f = 3.59\,\mathrm{GHz}$) for temperature 0.025 K, 0.07 K and 0.1 K can be seen, B^* and B_{C2} are determined from the fits. The inset in (a) shows a microscopic view on the situation, B^* and B_{C2} are related to two distinct coherence lengths for the two bands ξ^m_{GL}, ξ^l_{GL}.

be seen in the temperature dependence of $\sigma_1(T)$ for the $B = 0$ curve in the upper right plot of figure 5.4, experimental data that tracks the T-coherence peak in frequency and temperature can be found in [92]. In contrast the B-coherence peak can be observed at lowest achievable temperature, the initial rise of $\sigma_1(B)$ in dependence of B is greater than it would be expected when assuming normal conducting vortices. Quantities that are used to describe the superconducting state such as Δ, n_{sc}, ξ_{GL}, λ_L change only to small extent in dependence of T and B for $T \ll T_C$, $B \ll B_{C1},\ B_{C2}$, in this context the B-coherence peak is rather unusual. The density of vortices scales with B since the distance between two vortices is given by equation (2.38) and scales with $a_\Delta \propto B^{-1/2}$, so it is naturally to assume that the B-coherence peak is a result from enhanced conductivity in the vortex core. It is noted that B_{C1} of Nb:$SrTiO_3$ is in the order of the magnetic flux density of the planet earth [19]. Furthermore it is noted that the B-coherence peak vanishes with increasing frequency as it can be seen in figure 5.5, this behavior is similar to the T-coherence peak. A similar behavior of σ_1 is to the best knowledge of the author only described in thin films of BSCCO whereas the data is interpreted with a model for d-wave superconductivity, thus the comparability of

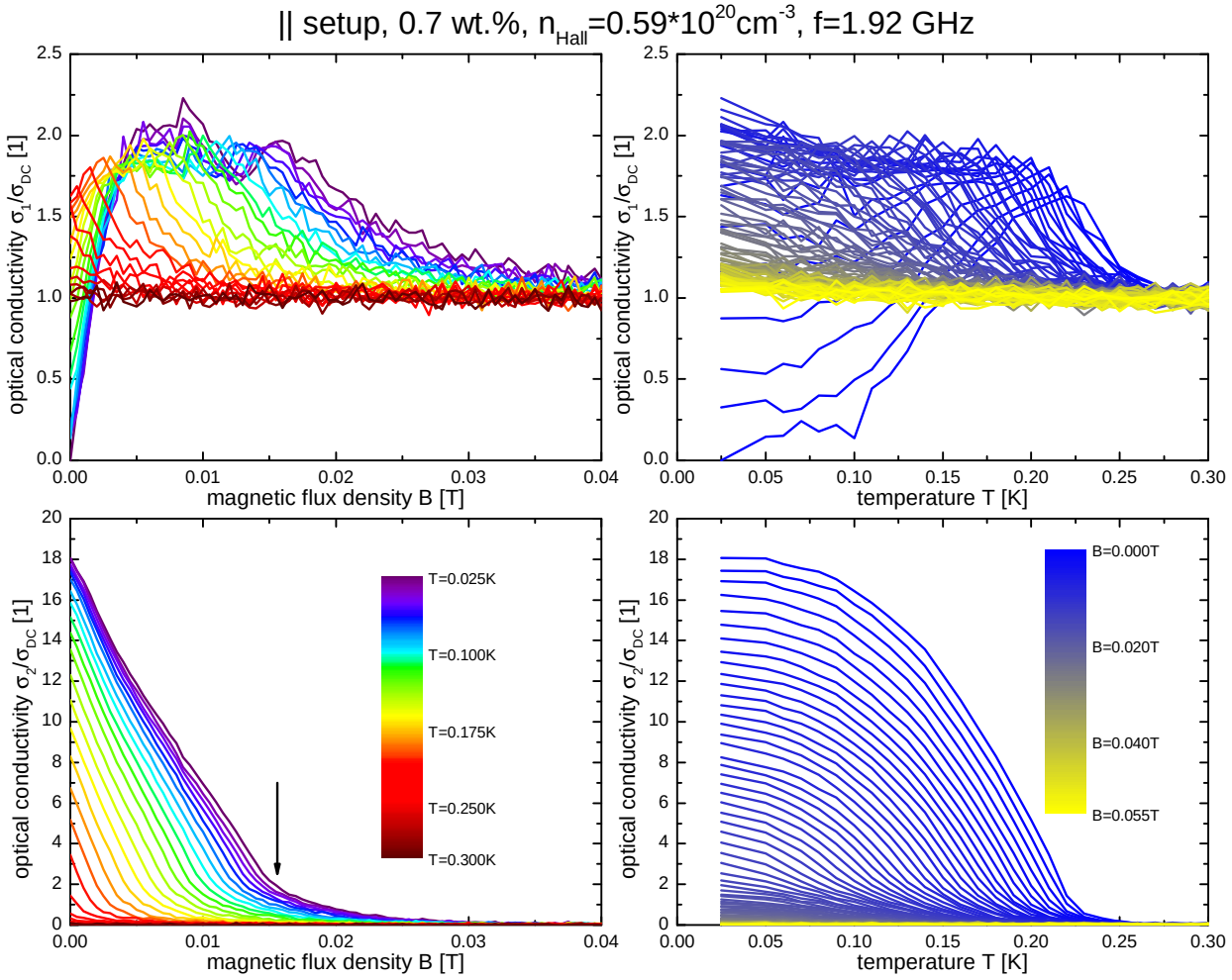

Fig. 5.7: Optical conductivity of the 0.7 wt. % Nb-doped $SrTiO_3$ sample at $f = 1.92\,\mathrm{GHz}$ in || orientation. The arrow marks the kink at B^* for lowest temperature.

thin BSCCO films to Nb:$SrTiO_3$ is not evident [93]. A discussion on conductivity enhancing effects in the Shubnikov phase is forwarded to the next chapter.

For $f = 10.59\,\mathrm{GHz}$, $\sigma_2(B)$ in dependence of B shows a linear decrease with a kink in the slope, the linear B-dependence can be readily interpreted with the linear B-scaling of the normal conducting volume that the vortices occupy in the superconducting bulk. For $f = 10.59\,\mathrm{GHz}$ $\sigma_1(B)$ also shows a linear B-dependence. It is interesting to note that the optical conductivity can be relatively easy interpreted in context of the Bardeen-Stephen model for greater frequencies whereas for lower frequencies conductivity enhancing effects in the vortex core may play a role.

5.2.2 Sample with 0.7 wt. % Nb doping

The analysis for the $SrTiO_3$ sample with 0.7 wt. % Nb doping is executed in the same way as for the sample with 0.1 wt. % Nb doping. In figure 5.7 and 5.8 the optical conductivity

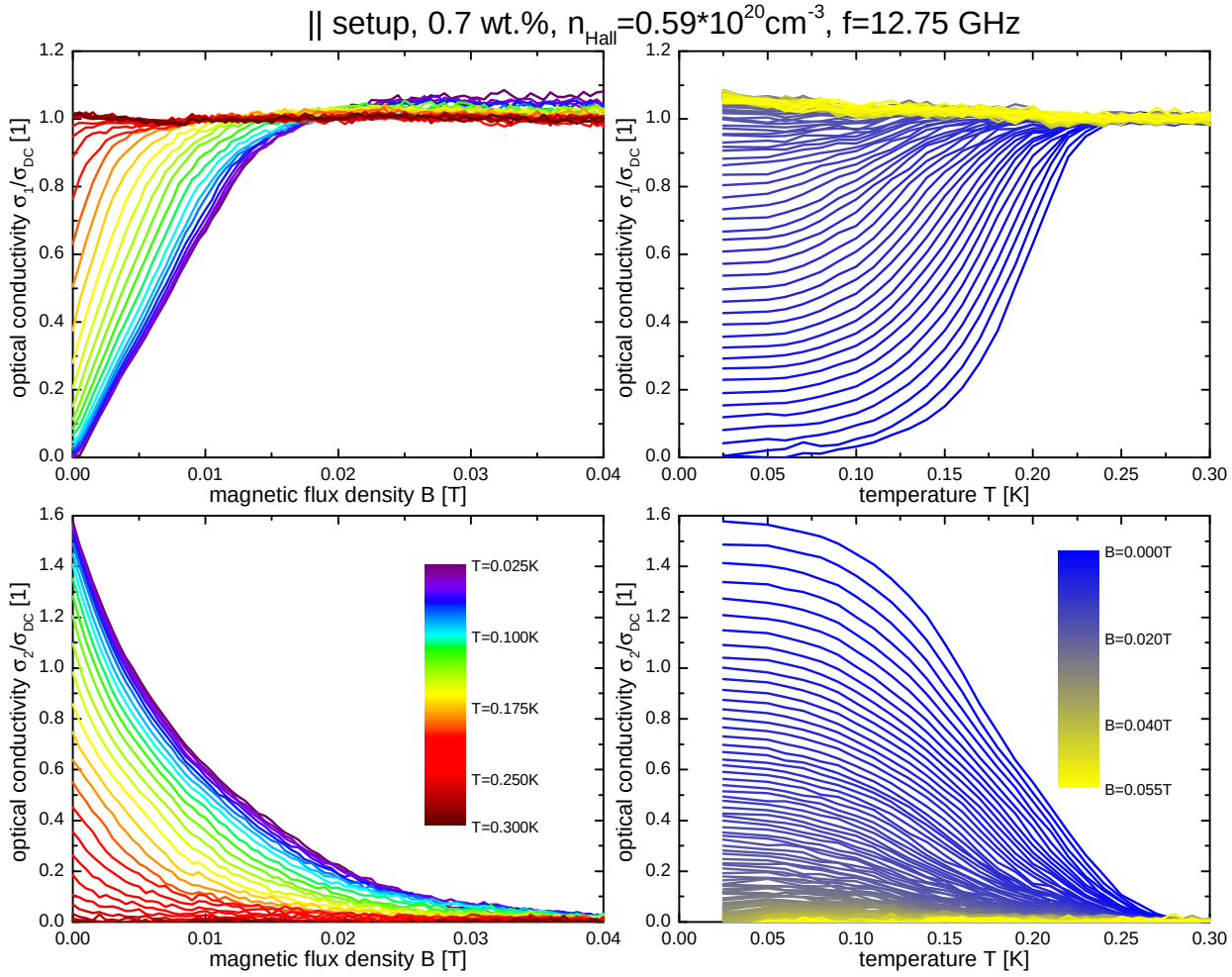

Fig. 5.8: Optical conductivity of the 0.7 wt. % Nb-doped $SrTiO_3$ sample at $f = 12.75\,\mathrm{GHz}$ in || orientation.

can be seen for frequencies $f = 1.92\,\mathrm{GHz}$, $f = 12.75\,\mathrm{GHz}$. The doping of the sample is not homogeneous, as result the change in slope at B^* is not fully developed as in the previously investigated sample [88]. As critical magnetic flux densities it is obtained $B^* = 15.6\,\mathrm{mT}$ and $B_{C2} = 24.3\,\mathrm{mT}$. Figure 5.7 shows the B-coherence peak as sharp initial rise of σ_1 in dependence of B as well as $\sigma_1(B) > \sigma_{\mathrm{DC}}$ even at lowest temperature. For greater frequencies the B-coherence peak vanishes as it can be seen in figure 5.8.

5.3 Optical conductivity $\hat{\sigma}$ in $\perp$-orientation

5.3.1 Hysteresis

When a superconducting resonator is swept from $B = 0$ to $B > B_{C2}$ and then back to $B = 0$, hysteresis can occur. In case when hysteresis occurs, the resonator properties $f_b(B,T)$, $f_0(B,T)$ change after sweeping to $B > B_{C2}$, typically a lowered quality factor $Q = f_0/f_b$

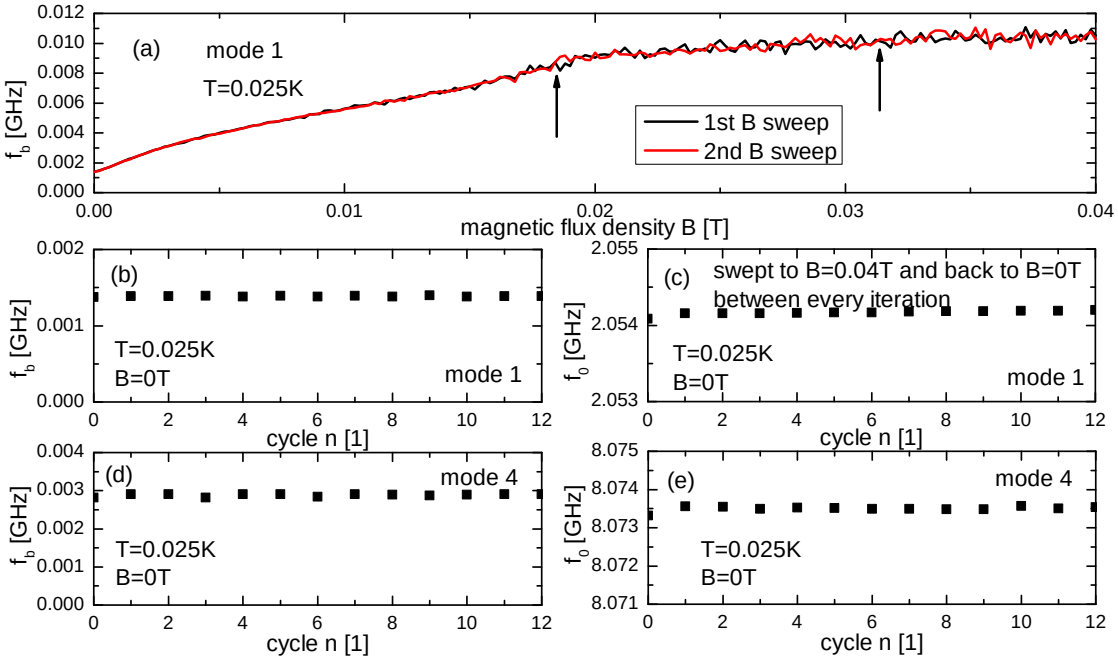

Fig. 5.9: Resonator properties of a lead resonator with 0.2 wt. % Nb-doped $SrTiO_3$ sample that has $B_{C2} = 31.3$ as perturbation. All measurements were executed without zero-field cooling. In (a) the frequency bandwidth f_b can be seen in dependence of B whereas the measurement was repeated, the arrows mark $B^* = 18.6\,\mathrm{mT}$ and $B_{C2} = 31.3\,\mathrm{mT}$ [88]. In (b), (c), (d), (e) the resonator properties f_b and f_0 can be seen for multiple cycles whereas a cycle consists of sweeping $B = 0$ to $B = 0.04\,\mathrm{T}$ and back to $B = 0$ again.

at the same B and T is observed. Hysteresis effects are a well-known feature in type I superconductors such as lead [90] as well as in type II superconductors such as niobium [94]. Since zero-field cooling is a time-consuming procedure, it is appropriate to check on hysteresis effects in Nb:$SrTiO_3$. In this subsection it is investigated on the 0.2 wt. % Nb-doped $SrTiO_3$ sample within the $\perp$-setup.

In figure 5.9 in (a) the frequency bandwidth f_b can be seen in dependence of B, the first B-sweep was executed after employing zero-field cooling of the sample to $T = 0.025\,\mathrm{K}$. After sweeping the magnetic flux density from the first B-sweep to $B = 0$, the second B-sweep was executed. The frequency bandwidth of the first and second sweep show close to perfect overlap whereas the small deviations are probably a result from slight uncertainties in the fitting procedure. In (b), (c), (d) and (e) the frequency bandwidth f_b and resonance frequency f_0 can be seen for two modes. A single measurement cycle consists of sweeping $B = 0$ to $B = 0.04\,\mathrm{T}$ and back to $B = 0\,\mathrm{T}$ whereas 12 cycles were performed. The resonance properties f_b and f_0 do not change significantly with accumulating cycles. It is noted that the first cycle shifts the resonance frequency slightly to a greater value whereas multiple cycles do not show a further shift, this is attributed to small hysteresis effects either due to lead or Nb:$SrTiO_3$.

In the context of the measurements it is concluded that Nb:$SrTiO_3$ shows no observable hysteresis effects.

5.3.2 Sample with 0.2 wt. % Nb doping

In contrast to the measurement in the ||-setup, no zero-field cooling is performed since the previous investigation established that no significant hysteresis effect could be observed. In contrast to the ||-setup the field configuration in the $\perp$-setup causes $\vec{J}_{\mathrm{ind}} \perp \vec{B}$ which results in a Lorentz force on the trapped flux quanta in the vortices. It is first checked if the lattice defects introduced by the niobium doping may pin the vortices. The crystal lattice parameter is $a_l = 0.39\,\mathrm{nm}$ [8] and every unit cell provides 0.0035 charge carriers [17], this way an average distance between two dopant sites that may possibly act as pinning centers of $0.39/0.0035\,\mathrm{nm} = 111.4\,\mathrm{nm}$ can be obtained. This is in the same order of magnitude as the GL coherence length ξ_{GL} as it can be seen in table 5.2. It is therefore concluded that pinning forces do not contribute to the vortex dynamics in Nb:$SrTiO_3$.

In figure 5.10 and 5.11 the optical conductivity can be seen for frequencies $f = 4.06\,\mathrm{GHz}$ and $f = 8.07\,\mathrm{GHz}$. For $f = 4.06\,\mathrm{GHz}$ the B-coherence peak is visible with an initial slope of $\sigma_1(B)$ that is much faster than expected from normal conducting vortices resulting in $\sigma_1(B,T) > \sigma_{\mathrm{DC}}$ even at lowest measured temperature. The decrease of $\sigma_2(B)$ shows a non-linear dependence on B, this is different from what is expected from the density of vortices that scales with B. In figure 5.12 the optical conductivity $\sigma_1(T,B)$ for $f = 4.06\,\mathrm{GHz}$ can be seen as 3D color plot. In figure 5.12 it is seen most convincingly how the B-coherence peak and T-coherence peak evolve into each other in dependence of T and B while displaying each on their own different characteristic features. For $f = 8.07\,\mathrm{GHz}$ $\sigma_1(B)$ in dependence of B asymptotically reaches a value of $\sigma_1 \approx 0.9\,\sigma_{\mathrm{DC}}$ at $B = 0.015\,\mathrm{T}$, it is not clear if this is a deviation from a linear B-dependence due to a weakly developed B-coherence peak or an exponential depletion of the first band. For both frequencies and real and imaginary part of the optical conductivity a kink in the B-dependence can be seen, as in the previous

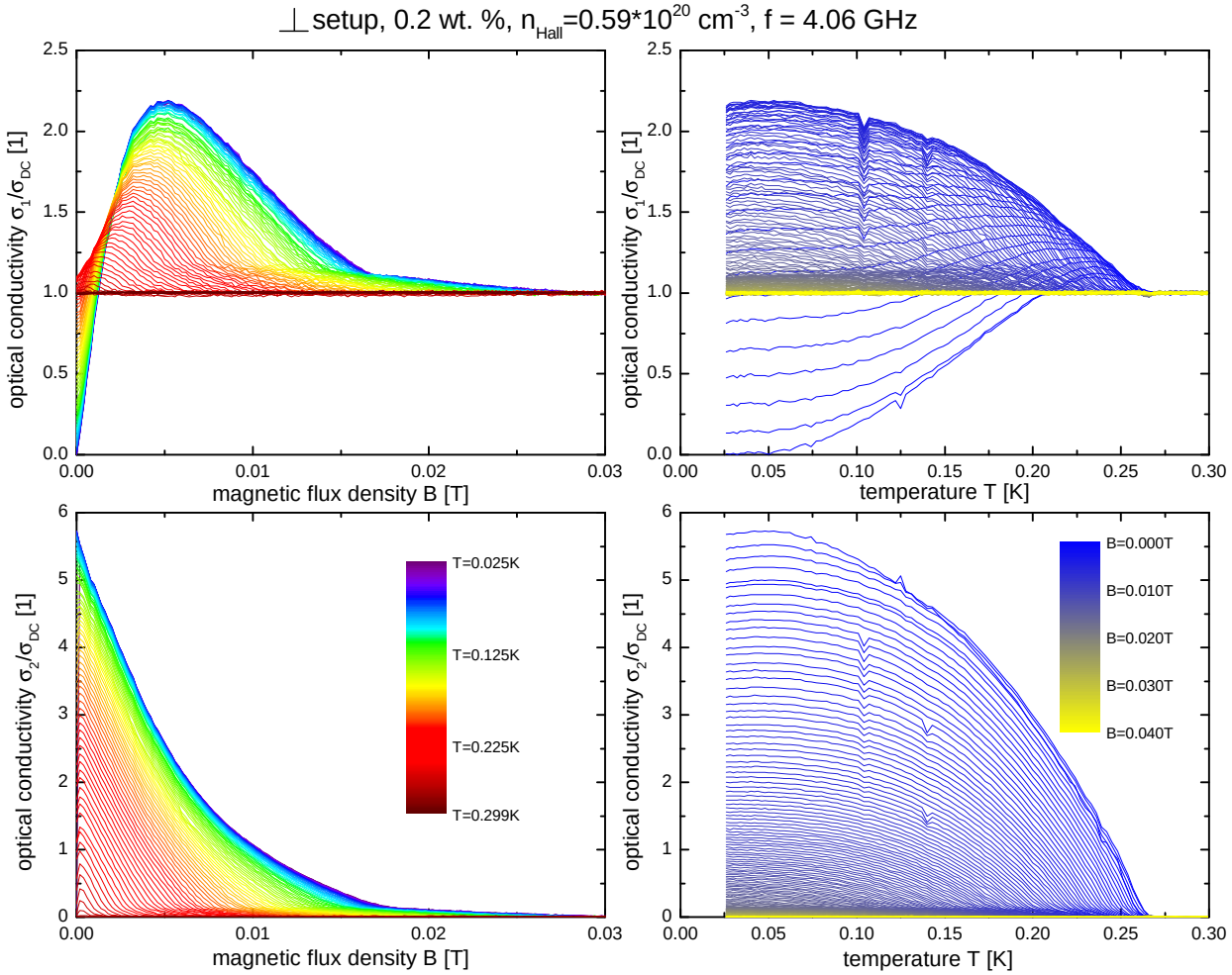

Fig. 5.10: Optical conductivity of the 0.2 wt. % Nb-doped $SrTiO_3$ sample at $f = 4.06\,\mathrm{GHz}$ in $\perp$ orientation.

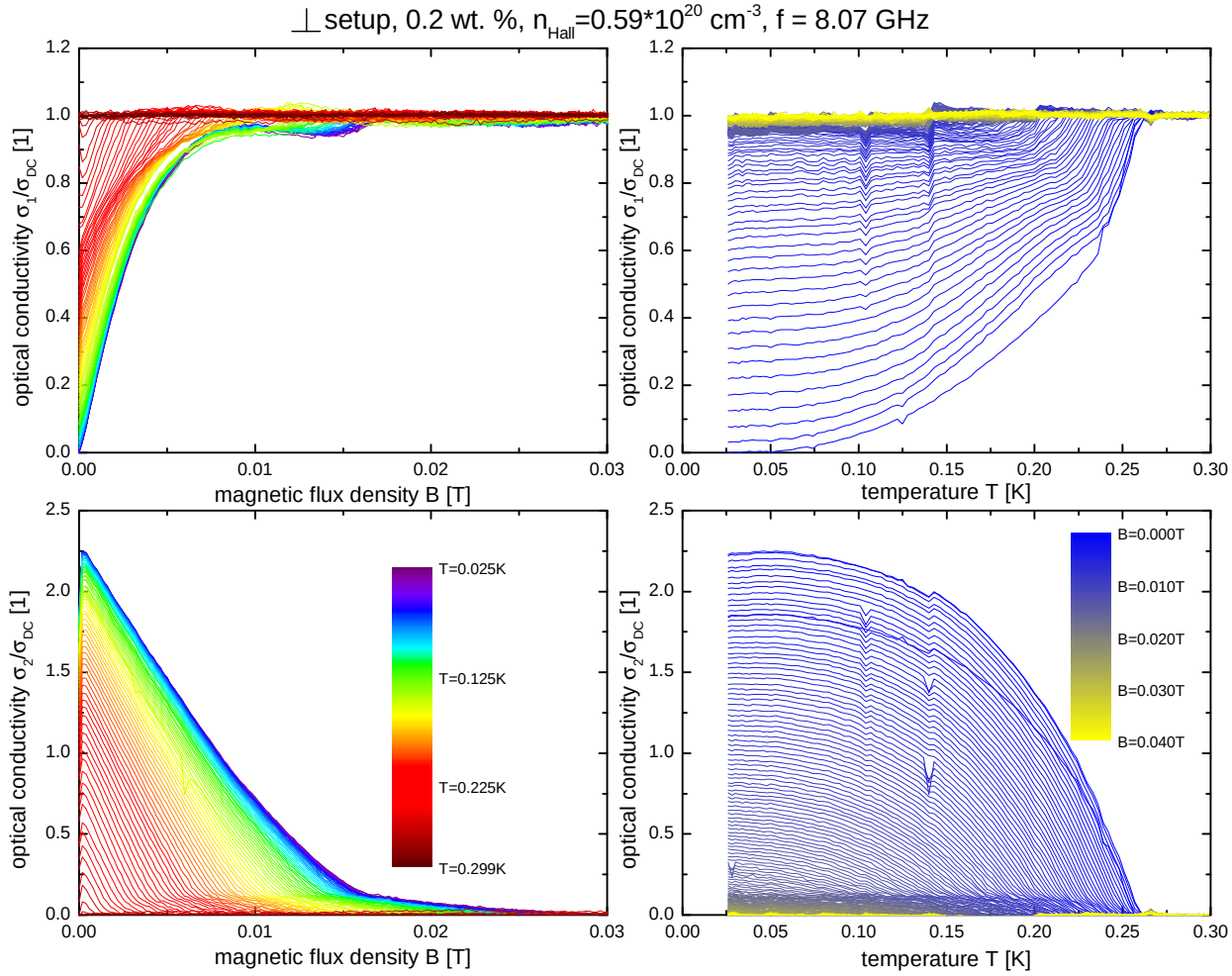

Fig. 5.11: Optical conductivity of the 0.2 wt. % Nb-doped $SrTiO_3$ sample at $f = 8.07\,\mathrm{GHz}$ in $\perp$ orientation.

optical conductivity data this is a result from the partial band filling where one band turns completely normal conducting at the kink, this means at $B = B^*$.

The optical conductivity in the $\perp$-setup shows a phenomenological behavior that is very similar to that in the ||-setup. Since the optical conductivity in the ||-setup could be readily interpreted in many points in the context of the Bardeen-Stephen model without including vortex dynamics, it is assumed that vortex dynamics do not enter the $\hat{\sigma}$ of the $\perp$-setup. It is appropriate to consider the field configuration of a resonance in the stripline setup. The field configuration depends on the meander structure of the center conductor. The magnetic field has nodes at the gaps and further nodes and maxima along the center conductor depending on the mode number n. It can be argued that the currents in neighboring loops and along one long arm of the center conductor cancel each other or enhance when the Lorentz force acts on the flux quanta of the vortices. It must be noted that taking account of the specific meander structure of the $\perp$-setup for every resonance mode is a non-trivial task. It may be speculated that the Lorentz force on the vortices cancel due to the meander structure where

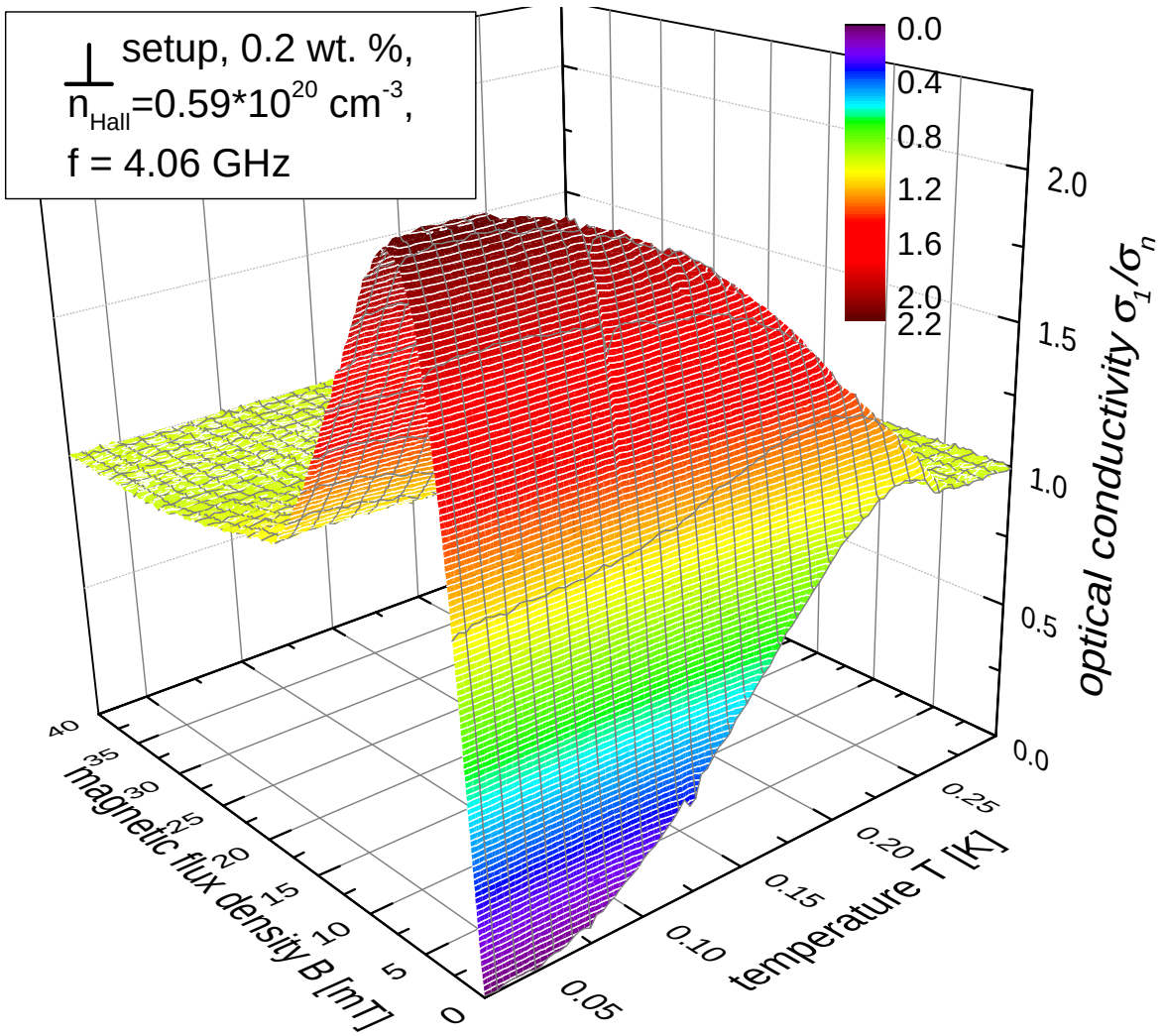

Fig. 5.12: Optical conductivity $\sigma_1(T, B)$ of the 0.2 wt. % Nb-doped $SrTiO_3$ sample at $f = 4.06\,\mathrm{GHz}$ in $\perp$ orientation.

every arm of the center conductor contains a current in the opposite direction that may even switch in sign along one arm. But in any case this is not a satisfying explanation and as conclusion it is stated that the optical conductivity data does not show effects of vortex dynamics although induced currents and vortices in Nb:$SrTiO_3$ are orientated perpendicular.

The optical conductivity data for more frequencies can be seen in the Appendix.

5.4 Dome of critical fields

Nb doping [wt. %]	0.1	0.2	0.35	0.5	0.7
n_{Hall} [$10^{20}\,\mathrm{cm}^{-3}$]	0.33	0.59	1.1	2.0	2.2
$\lambda_{\mathrm{eff}}(T=0)$ [μm]	2.4	1.7	1.4	1.4	1.8
$\Gamma_{\mathrm{scat.}}/(2\pi)$ [GHz]	47	87	169	248	365
B^* [mT]	9.0	18.6	32.5	18.9	15.6
ξ^m_{GL} [nm]	191	133	100	132	145
B_{C2} [mT]	15.1	31.3	53.8	32.0	24.3
ξ^l_{GL} [nm]	148	103	78	101	116
clean: E_F [meV] from B^*	2.82	3.11	3.31	3.67	2.61
clean: E_F [meV] from B_{C2}	4.70	5.18	5.59	6.07	4.69
lower limit:					
dirty: E_F [meV] from B^*	1.09	1.47	2.23	4.52	6.17
corresponding l [nm]	339	213	135	131	104
dirty: E_F [meV] from B_{C2}	1.08	1.46	2.25	4.46	6.63
corresponding l [nm]	339	213	136	130	108
upper limit:					
dirty: E_F [meV] from B^*	1.82	2.46	3.73	7.56	10.33
corresponding l [nm]	262	165	104	101	81
dirty: E_F [meV] from B_{C2}	1.81	2.45	3.77	7.47	11.09
corresponding l [nm]	262	164	105	101	83

Tab. 5.2: Scattering rates $\Gamma_{\mathrm{scat.}}$ obtained from resistivity measurements and London penetration depth $\lambda_{\mathrm{eff}}(T=0)$, taken from [88]. Critical B^*, B_{C2} taken from [88] except for the highest and lowest doped sample. Fermi energy calculated according to equation (5.10) and (5.14). GL coherence length calculated according to equation (2.39).

At this stage of the analysis it is appropriate to discuss the band structure of doped $SrTiO_3$. The analysis so far established that two bands with two coherence lengths ξ^m_{GL}, ξ^l_{GL} are respectively depleted at B^* and B_{C2}. The charge carrier concentration of the samples that are investigated in this thesis range from $n_{\mathrm{Hall}} = 0.33 \cdot 10^{20}\,\mathrm{cm}^{-3}$ to $n_{\mathrm{Hall}} = 2.2 \cdot 10^{20}\,\mathrm{cm}^{-3}$. In figure 5.13 in (a) the effective mass m of the three relevant electronic bands as determined by Lin *et al.* can be seen, the charge carrier concentration of the samples in this thesis is larger than the n_{c2} by Lin *et al.* [80]. The band that is referred to as upper band in figure 5.13 in (a) and (b) contributes only weakly to the superconducting state.

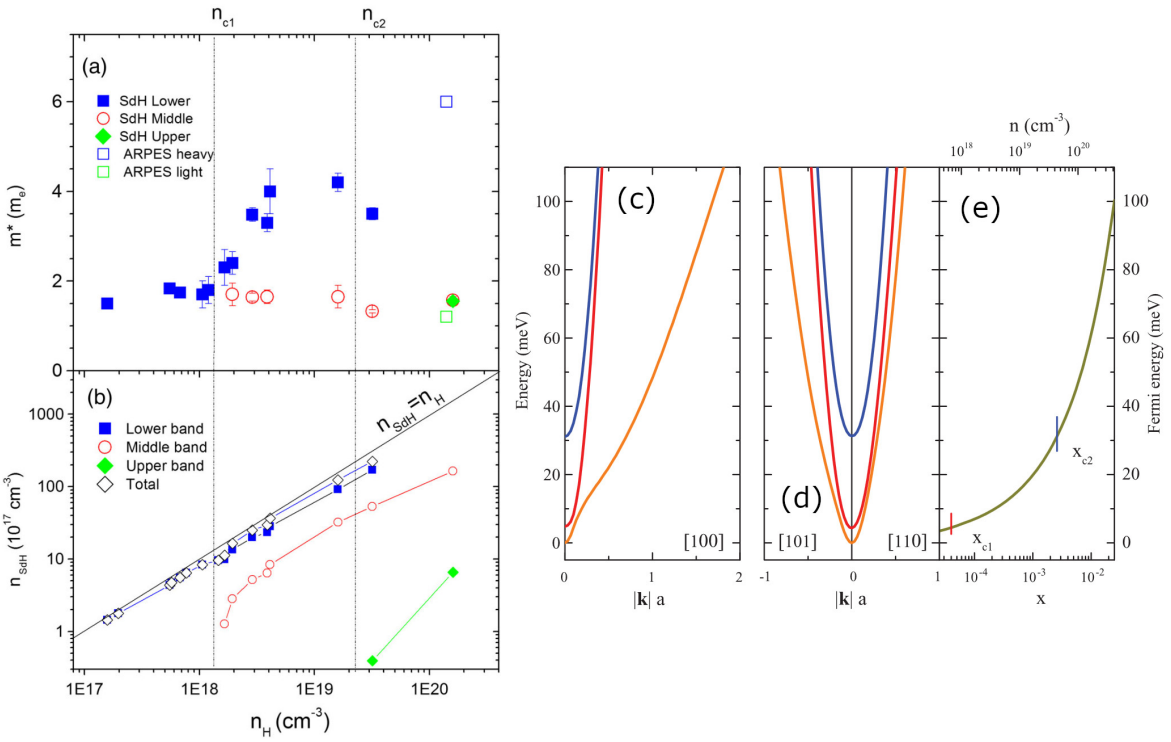

Fig. 5.13: In (a) the effective mass of the respective band in $SrTiO_3$ determined by Shubnikov-deHaas measurements can be seen, in (b) the charge carrier density contributed by the respective bands can be seen, both in dependence of the total charge carrier density $n_{\mathrm{H}} = n_{\mathrm{Hall}}$. (a) and (b) are taken from [80]. In (c) and (d) the theoretically obtained band structure of doped $SrTiO_3$ can be seen, in (e) the theoretically expected dependence of the Fermi energy on the charge carrier density. (c), (d) and (e) are taken from [82].

It can be seen that the effective mass for the lower band in figure 5.13 in (a) shifts from approximately $m = 1.5\,m_e$ to approximately $m = 4.2\,m_e$ for greater charge carrier density. The values for m are chosen such that the analysis here can be conducted in the same manner as it was done by Thiemann [88]. Lin *et al.* interpreted the n_{Hall}-dependent effective mass in the context of the theoretical investigation by van der Marel *et al.* that can be seen in figure 5.13 in (c), (d) and (e) [82]. The investigation by van der Marel *et al.* revealed in analogy to the investigation by Lin *et al.* three contributing bands that are respectively filled for two critical doping concentration x_{c1} and x_{c2}. The lowest band in figure 5.13 in (c) and (d) shows a departure from the parabolic behavior that was interpreted by Lin *et al.* as cause for the change in the measured effective mass in dependence of charge carrier density. The Shubnikov-deHaas measurements conducted by Lin *et al.* suggests that the observed bands in this thesis are the lower and middle band. The lower band has the effective mass $m = 4.2\,m_e$ and the middle band has the effective mass $m = 1.5\,m_e$. The following analysis will establish that the middle band is depleted at B^* and the lower band is depleted at B_{C2} hence the index m for the middle band in the coherence length ξ^m_{GL} and l for the lower band in ξ^l_{GL}.

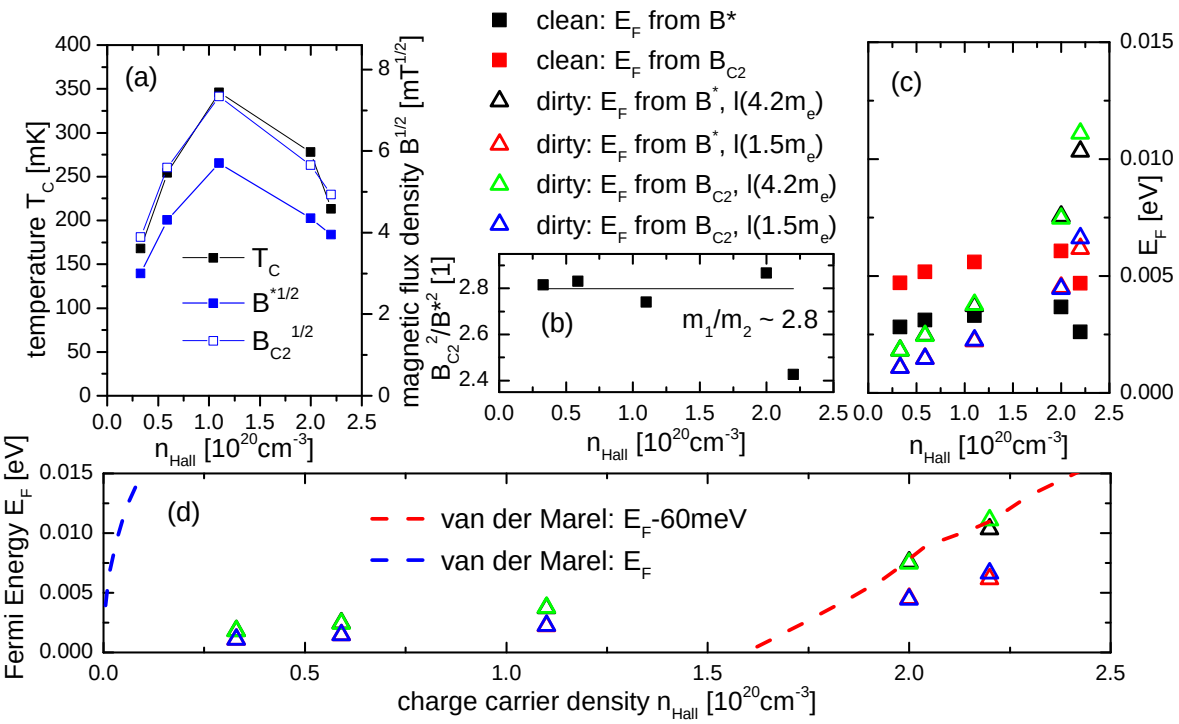

Fig. 5.14: In (a) T_C together with B^*, B_{C2} can be seen, the overlapping data suggest $T_C \propto B_{C2}^{1/2}$, $B^{*1/2}$. In (b) the ratio $(B_{C2}/B^*)^2$ can be seen, the straight line is the ratio of effective masses $4.2m_e/1.5m_e = 2.8$ of both bands of Nb:$SrTiO_3$ [80]. In (c) the Fermi energy can be seen in the dirty and clean limit according to equation (5.10) and (5.14). In (d) the Fermi energy from (c) in the dirty limit can be seen along the prediction by van der Marel [82], the red curve is shifted so that it matches the two data points at highest doping for $l(4.2m_e)$.

In figure 5.14 in (a) the dome of critical fields B^* and B_{C2} can be seen along T_C in dependence of the charge carrier density n_{Hall}. The data suggests $T_C \propto B_{C2}^{1/2}$, $B^{*1/2}$. It is noted that the unusually strong isotope effect of $SrTiO_3$ with an enhancement of T_C by ~ 1.5 and B_{C2} by ~ 2 is consistent with the dependence of T_C, $B_{C2}^{1/2}$, $B^{*1/2}$ on the n_{Hall} that is observed here [87]. The critical temperature T_C can be related to the critical fields $B_{C2}^{1/2}$, $B^{*1/2}$. First T_C is expressed as Δ with equation (2.13). The next step will make a distinction into the clean and dirty limit.

In the clean case it is related via equation (2.14), (2.33), (2.39)

$$\Delta(T=0) = \frac{0.907 \cdot \hbar v_F}{\pi} \sqrt{\frac{2\pi B^{\alpha}}{\Phi_0}} \tag{5.9}$$

whereas $B^\alpha = B^*, B_{C2}$ is a placeholder variable. The band-specific Fermi velocity is expressed as Fermi Energy $v_F = \sqrt{2E_F/m}$ with effective mass m. With the definition of the flux quantum $\Phi_0 = h/(2e)$

$$\Delta(T=0) = \frac{2 \cdot 0.907}{\pi}\sqrt{e\hbar} \cdot \sqrt{\frac{E_F B^\alpha}{m}} = \sqrt{\frac{E_F B^\alpha}{m}} \cdot 2.37 \cdot 10^{-27}\sqrt{\mathrm{kgAm}} \tag{5.10}$$

is obtained.

In the dirty limit it can be related via equation (2.14), (2.34), (2.39)

$$\Delta(T=0) = \hbar v_F \cdot 0.907^2 l \frac{2B^\alpha}{\Phi_0}. \tag{5.11}$$

Unlike as in the clean limit the band-specific free mean path l enters. It is again $v_F = \sqrt{2E_F/m}$ with effective mass m. It is obtained

$$\Delta(T=0) = \frac{2\sqrt{2}e \cdot 0.907^2}{\pi} \cdot lB^\alpha\sqrt{\frac{E_F}{m}} = lB^\alpha\sqrt{\frac{E_F}{m}} \cdot 1.185 \cdot 10^{-19}\,\mathrm{As}.. \tag{5.12}$$

The band-specific free mean path l can be related to the scattering rate $l = 2\pi v_F/\Gamma_{\text{scat.}}$ that is given in table 5.1 but those $\Gamma_{\text{scat.}}$ are averaged over the bands. Therefore appropriate upper and lower limits for l are estimated. It is assumed that the correct l is within the limits

$$l = \frac{2\pi}{\Gamma_{\text{scat.}}}\sqrt{\frac{2E_F}{m}} \tag{5.13}$$

for $m = 1.5\,m_e$ and $m = 4.2\,m_e$. The effective mass m enters the free mean path via the band-specific Fermi velocity, but m in equation (5.13) is not set according to the band that is considered, but as limits. When equation (5.13) is inserted into (5.12) the upper and lower limit of l results in an upper and lower limit for E_F. It is noted with emphasis that m in equation (5.12) and (5.13) are not the same quantities! Inserting equation (5.13) into (5.12) returns

$$\Delta(T=0) = \frac{2\sqrt{2}e \cdot 0.907^2}{\pi} \cdot \frac{2\pi}{\Gamma_{\text{scat.}}}\sqrt{\frac{2E_F}{m^\beta}} \cdot B^\alpha\sqrt{\frac{E_F}{m^\alpha}}. \tag{5.14}$$

An upper ($m^\beta = 4.2\,m_e$) and lower limit ($m^\beta = 1.5\,m_e$) for E_F is obtained with equation (5.14)

Assuming the same E_F for both bands together with the observation of only one gap $\Delta(T=0)$ [17] it is seen from both equations (5.10) and (5.14) that a greater B^α is associated with a greater effective mass. It is therefore concluded that the lower band with effective mass $m = 4.2\,m_e$ is depleted at B_{C2} and that the middle band with effective mass $m = 1.5\,m_e$ is depleted at B^*. The obtained Fermi energies in the respective clean and dirty limit according to equation (5.10) and (5.14) can be seen in table 5.2.

When assuming that the Fermi Energy E_F and that the free mean path l is the same for both bands, with equation (5.12) it can be related in the dirty limit $B_{C2}^2/B^{*2} = 4.2m_e/1.5m_e = 2.8$. In the clean limit it suffices to assume that the Fermi energy is the same for both bands to

relate with equation (5.10) $B_{C2}/B^* = 4.2m_e/1.5m_e = 2.8$. In figure 5.14 in (b) it can be seen that the measured ratios of the critical fields squared equals relatively good ~ 2.8 except the highest doped sample that is known to be not homogeneously doped. This finding suggests the dirty limit. The significance of this statement should not be overestimated since E_F and l were assumed for both bands to be same, but it is an indication that points towards the dirty limit.

In figure 5.14 in (c) the Fermi energy from table 5.2 can be seen. Here $l(4.2m_e)$ and $l(1.5m_e)$ mark the upper and lower limit for the Fermi energy due to the uncertainty of the band-specific free mean path. The values for the dirty limit for the upper and lower limit of l almost overlap, this is no surprise since it was previously established that $B_{C2}^2/B^{*2} \sim 4.2m_e/1.5m_e$. The Fermi energy in the clean limit shows a dome-behavior whereas the maximal Fermi energy is reached for $n_{\mathrm{Hall}} = 2 \cdot 10^{20}\,\mathrm{cm}^{-3}$. The Fermi energy in the dirty limit shows a sharp rise towards greater doping.

Van der Marel *et al.* computed the Fermi energy in dependence of the doping $E_F(n)$ with a theoretical model, $E(n)$ can be seen in figure 5.13 in (e) [82]. In figure 5.14 in (d) the Fermi energy in the dirty limit can be seen along with the prediction by van der Marel. It is apparent that the obtained values of E_F in this thesis are much smaller than the theoretically calculated E_F. Shifting the prediction by van der Marel by 60 meV shows accordance in absolute values and slope with the Fermi energy at high doping, it is not clear whether this is a coincidence or if a systematic error entered. It is noted that the Fermi energy E_F enters equation (5.10) and (5.10) via the Fermi velocity v_F, it may be speculated that a relation between the coherence length ξ_Δ and the Fermi energy E_F may not be straightforwardly established as previously assumed.

5.5 Partial Band filling

So far it is established that for sufficiently high frequency the optical conductivity can be assumed as linear composite of a relatively robust superconducting state and the normal conducting vortices with weight according to the occupied volume in the bulk. Further it is established that a vortex has two GL coherence lengths that correspond to two critical upper fields B^*, B_{C2} due to two superconducting bands, the middle band with ξ_{GL}^m and $m = 1.5\,m_e$ is depleted at B^* and the lower band with ξ_{GL}^l and $m = 4.2\,m_e$ is depleted at B_{C2} [88]. The close to linear decrease of $\sigma_2(B)$ in dependence of B and the identification of the two critical upper fields B^*, B_{C2} with two bands suggests further that the interaction of the bands with each other can be neglected. In this section the linear B-dependence of $\sigma_2(B)$ is used to obtain a partial filling factor of the bands. It is focused on σ_2 at sufficient high frequencies to exclude the effects of the B-coherence peak.

It is now turned to the determination of the partial band filling. The optical conductivity respectively for the lower and middle band is expressed as linear mean of the optical conductivity of the superconducting state and the normal conducting vortices with volume filling factor $f_n^{l,m}$

$$\frac{\hat{\sigma}^{l,m}}{\sigma_{\mathrm{DC}}^{l,m}} = \frac{\sigma_1^{l,m} + \mathrm{i}\sigma_2^{l,m}}{\sigma_{\mathrm{DC}}^{l,m}} = f_n^{l,m} + (1 - f_n^{l,m})\hat{f}^{\mathrm{MB}}. \tag{5.15}$$

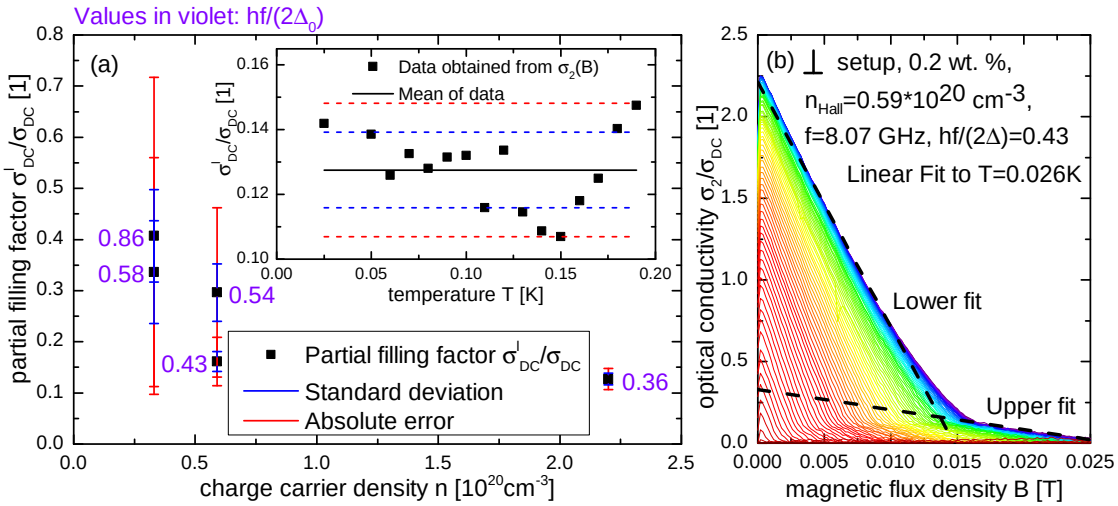

Fig. 5.15: In (a) the partial filling factor, namely the ratio of the DC contribution of the lower band to the total DC conductivity σ^l_{DC} can be seen. The inset in (a) shows how the error bars are obtained exemplary for the highest doped sample $n = 2.2 \cdot 10^{20}\,\mathrm{cm}^{-3}$, the red line marks the total error and the blue line the standard deviation. In (b) the data from figure 5.11 can be seen with linear fits to $T = 0.026\,\mathrm{K}$, from the intercept of both fits with the $\sigma_2/\sigma_{\mathrm{DC}}$-axis $\sigma^l_{\mathrm{DC}}/\sigma_{\mathrm{DC}}$ is obtained.

$\hat{\sigma}^{l,m}$ accounts for the band-specific optical conductivity and $\sigma^{l,m}_{\mathrm{DC}}$ accounts for the DC conductivity that is contributed by the lower (index l) and middle (index m) band. The conductivities are assumed to return the total values as superposition $\hat{\sigma} = \hat{\sigma}^l + \hat{\sigma}^m$ and $\sigma_{\mathrm{DC}} = \sigma^l_{\mathrm{DC}} + \sigma^m_{\mathrm{DC}}$. The volume filling factor is normalized such that $0 \leq f^{l,m}_n \leq 1$. It is further assumed that the superconducting volume follows the Mattis-Bardeen prediction (2.26) with $\hat{f}^{\mathrm{MB}} = f^{\mathrm{MB}}_1 + \mathrm{i} f^{\mathrm{MB}}_2$. The Mattis-Bardeen prediction for both bands depends on Δ, since Nb:SrTiO$_3$ is a single gap superconductor [88] the Mattis-Bardeen prediction for both bands is the same.

It is appropriate to consider how both bands contribute to σ_2. With equation (5.15) it can be obtained

$$\begin{aligned}\frac{\sigma_2}{\sigma_{\mathrm{DC}}} &= \frac{\sigma^l_2 + \sigma^m_2}{\sigma_{\mathrm{DC}}} = \frac{\sigma^l_{\mathrm{DC}}}{\sigma_{\mathrm{DC}}}\frac{\sigma^l_2}{\sigma^l_{\mathrm{DC}}} + \frac{\sigma^m_{\mathrm{DC}}}{\sigma_{\mathrm{DC}}}\frac{\sigma^m_2}{\sigma^m_{\mathrm{DC}}} = \left(1 - \frac{\sigma^l_{\mathrm{DC}} f^l_n + \sigma^m_{\mathrm{DC}} f^m_n}{\sigma_{\mathrm{DC}}}\right) f^{\mathrm{MB}}_2 \\ &= \left(1 - \frac{\sigma^l_{\mathrm{DC}}}{\sigma_{\mathrm{DC}}}\frac{B}{B^*}\Theta(B^* - B) - \frac{\sigma^m_{\mathrm{DC}}}{\sigma_{\mathrm{DC}}}\frac{B}{B_{C2}}\Theta(B_{C2} - B)\right) f^{\mathrm{MB}}_2.\end{aligned} \tag{5.16}$$

In the last line a linear B-dependence of $f^{l,m}_n$ is assumed and $\Theta(x)$ is the Heaviside step function. The linear B-dependence is justified since the distance between two vortices scales as $a_\Delta \propto B^{-1/2}$ as it can be seen from equation 2.38. The experimental observation that σ_2 decreases linearly with B justifies to neglect the B-dependence of f^{MB}_2.

It is readily seen that the intercepts of two linear fits to σ_2 in dependence of B for $B < B^*$ and $B > B^*$ with the $\sigma_2/\sigma_{\mathrm{DC}}$-axis can be used to obtain the partial filling factor, here

expressed as the ratio of the DC contribution of the lower band to the total DC conductivity $\sigma^l_{\mathrm{DC}}/\sigma_{\mathrm{DC}}$. The linear fits used to determine the intercepts can be seen in figure 5.15 in (b), the ratio of the intercept of the upper fit with the $\sigma_2(B)/\sigma_{\mathrm{DC}}$-axis to the intercept of the lower fit with the $\sigma_2(B)/\sigma_{\mathrm{DC}}$-axis equals $\sigma^l_{\mathrm{DC}}/\sigma_{\mathrm{DC}}$. The partial filling factor $\sigma^l_{\mathrm{DC}}/\sigma_{\mathrm{DC}}$ is obtained for every temperature T and then averaged. The partial filling factor shows strong deviations that are attributed to deviations of the linear B-dependence of σ_2. These deviations are used to obtain the error bars for the measured partial filling factor, a standard deviation is computed as well as an absolute error that accounts for the maximal deviation. In figure 5.15 in (a) in the inset the obtained values for $\sigma^l_{\mathrm{DC}}/\sigma_{\mathrm{DC}}$ for different temperatures can be seen for the highest doped sample, the inset also shows the standard deviation and the absolute error. The data that was used to obtain the partial filling factor can be found seen in figure 8.3, 5.5, 5.11, 8.7, 8.10.

It is important to discuss the role of the DC conductivities $\sigma^{l,m}_{\mathrm{DC}}$ that were attributed to the lower and middle band. Although labeled DC conductivities in analogy to the Mattis-Bardeen formalism as used in this thesis, $\sigma^{l,m}_{\mathrm{DC}}$ are technically normalization factors for the superconducting optical conductivities to compute the linear mean that was measured. In that sense $\sigma^{l,m}_{\mathrm{DC}}$ attributes for charge carrier concentration, scattering time and effective mass at once for one considered band. It may be tempting to argue that for greater $\sigma^l_{\mathrm{DC}}/\sigma_{\mathrm{DC}}$ the lower band may contribute more charge carriers, but from physics perspective this statement is not straightforward to make. In addition and in regard to the B-coherence peak it is noted that the assumption that the two bands do not interact is a rather heuristic assumption to apply the just conducted analysis.

The obtained values for the partial filling as it can be seen in figure 5.15 in (a) do not allow a straightforward interpretation. Despite the objections that were just mentioned, it may be guessed that with greater doping the partial filling of the lower band should decrease, although the bare values seem to confirm this trend the large error bars do not allow to make a quantified statement. It is noted that for the second lowest doped sample the values are not located within the error bars of the standard deviation. With the absolute error in mind it could also be the case that the partial filling factor remains constant.

6 Conductivity enhancing effects in the Shubnikov phase

6.1 Preceding considerations

The last chapter established the B-coherence peak in the Shubnikov phase of the Type II superconductor Nb:$SrTiO_3$. The characteristic properties of the B-coherence peak are a sharp initial rise of σ_1 in dependence of B with a slope that is greater than it would be expected from the composite conductivity of normal conducting vortices in the superconducting bulk, absolute values of σ_1 that rise to multiple times of σ_{DC}, persistence of the peak down to lowest temperatures, and the weakening and disappearance for greater frequencies. In contrast the T-coherence peak in zero-field describes the increase of $\sigma_1 > \sigma_{\mathrm{DC}}$ close to T_C for small frequencies $hf \ll 2\Delta$ as result of the density of states that diverges at $E = \pm\Delta$, a feature whose experimental evaluation is considered as one of the early confirmations of the BCS theory. The superconducting state is usually well protected against small changes of B and T when it is $B \ll B_{C1}$, B_{C2} and $T \ll T_C$. In the case of Nb:$SrTiO_3$ that has a very small B_{C1}, it is one possible explanation to assume that the B-coherence peak is a result of enhanced conductivity in the vortex core.

In this chapter possible explanations for the B-coherence peak are reviewed. The first investigation is a theoretical investigation on the effects of a B-dependent energy gap $\Delta(B)$ in the superconducting volume on the optical conductivity σ_1. The second investigation will focus on states in the vortex core, the so-called Caroli-deGennes-Matricon mode (CdGM mode) [95]. It will be shown that the states in the vortex core provide a reasonable explanation for the B-coherence peak. The Two-Band nature of $SrTiO_3$ is neglected in this chapter.

6.2 $\vec{B}$ dependence of the energy gap $\triangle$ in the mixed state

6.2.1 Effective $\vec{B}$ in the superconducting area

In this subsection it is investigated on the magnetic flux density B that penetrates a type II superconductor in the Shubnikov phase. For clarity a distinction is made between the externally applied B_{ext} that was so far in the experimental context referred to as B, and the actual magnetic flux density $B_{\mathrm{int}}(r)$ in the superconductor that may be also position dependent although it will turn out that B_{int} is reasonably isotropic with the assumptions that are made in the text. The optical conductivity will be assumed as linear mean of the superconducting volume and the normal conducting vortices with weight according to the occupied volume of the vortices that are assumed to be cylinders with radius ξ_{GL}. The optical

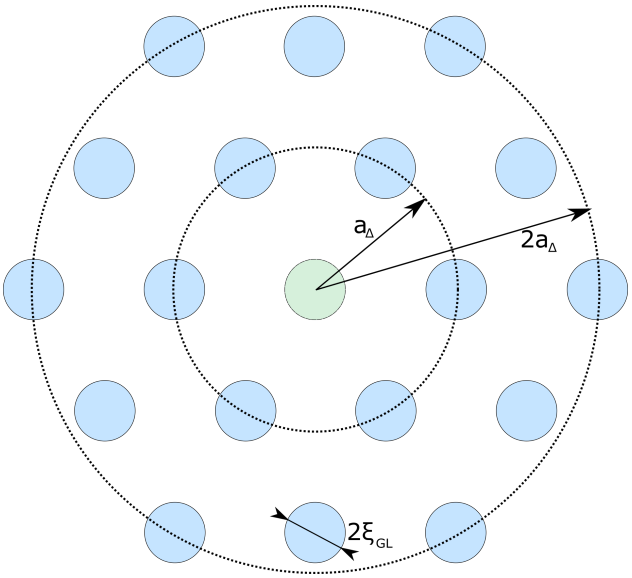

Fig. 6.1: A complementary depiction to the calculation of B_{int} can be seen. B_{int} is calculated in the center vortex by adding B_{vortex} from equation (6.1) of all vortices except that of the center vortex. For simplicity it is assumed that all vortices are on circles with radius that are integer multiples of a_Δ.

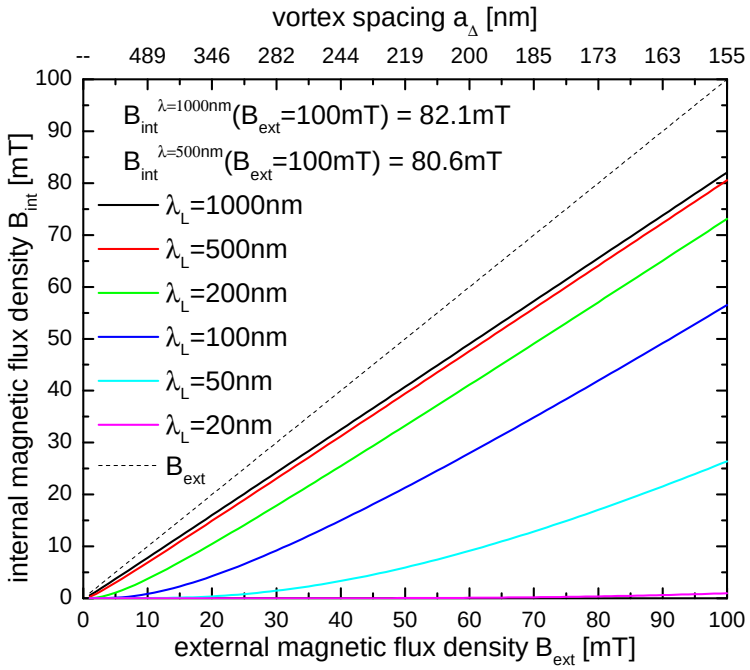

Fig. 6.2: The close to isotropic internal magnetic flux density B_{int} in dependence of the external magnetic flux density B_{ext} according to equation (6.2), B_{ext} enters via equation (2.38) through the vortex spacing a_Δ. For $\lambda_L > 500\,\text{nm}$ an almost linear relation $B_{\text{int}}(B_{\text{ext}}) = 0.81 B_{\text{ext}}$ can be observed. The result is only valid for high κ samples with $a_\Delta > \xi_{\text{GL}}$.

conductivity of the superconducting volume will be assumed to follow the Mattis Bardeen prediction with a B_{int}-dependent energy gap $\Delta(B_{\text{int}})$. This way the real part of the composite optical conductivity σ_1 of a superconductor in the Shubnikov phase is obtained and can be checked with the experimentally observed data from the previous chapter, specifically if a feature like the B-coherence peak or characteristics of B-coherence peak are reproduced.

For an external magnetic flux density $B_{c1} < B_{\text{ext}} < B_{c2}$ a type II superconductor enters the Shubnikov phase. A vortex is assumed to be a normal conducting cylinder with radius ξ_{GL} [33, 91]. In GL theory a single isolated vortex displays a radially varying magnetic flux density

$$B_{\text{vortex}}(r) = \frac{\Phi_0}{2\pi\lambda_{\text{eff}}^2} K_0\left(\frac{r}{\lambda_{\text{eff}}}\right) \approx \frac{\Phi_0}{2\pi\lambda_{\text{eff}}^2}\sqrt{\frac{\pi}{2}\frac{\lambda_{\text{eff}}}{r}} \cdot e^{-\frac{r}{\lambda_{\text{eff}}}} \tag{6.1}$$

according to equation (2.37), the approximation holds for $r \gg \lambda_L$ and r is the distance from the vortex core. In the limit $\kappa \gg 1$ the superposition of the magnetic flux densities of the respective vortices is valid [33]. The limit $\kappa \gg 1$ applies to the investigated Nb:$SrTiO_3$ samples in this thesis [88]. The value of the internal magnetic flux density B_{int} in the Shubnikov phase in the presence of an external magnetic flux density B_{ext} can be obtained by summing over the magnetic flux densities $B_{\text{vortex}}(r)$ of all vortices. The sum is evaluated at the center of a vortex and the magnetic flux density of that vortex in the center is set to $B_{\text{vortex}}(r = 0) = 0$ for simplicity. It is obtained

$$\begin{aligned} B_{\text{int}} &= 6 \cdot \sum_{n=1}^{\infty} B_{\text{vortex}}(n a_\Delta) \cdot n \\ &= 6 \cdot \left[\sum_{n=1}^{n_0} B_{\text{vortex}}(n a_\Delta) \cdot n + \frac{\Phi_0}{2\pi\lambda_{\text{eff}}^2}\sqrt{\frac{\pi}{2}} \sum_{n=n_0+1}^{\infty} \sqrt{\frac{n\lambda_{\text{eff}}}{a_\Delta}} e^{-\frac{n a_\Delta}{\lambda_{\text{eff}}}}\right] \\ &= 6 \cdot \frac{\Phi_0}{2\pi\lambda_{\text{eff}}^2}\left\{\sum_{n=1}^{n_0}\left[n \cdot K_0\left(n\frac{a_\Delta}{\lambda_{\text{eff}}}\right) - \sqrt{\frac{n\pi\lambda_{\text{eff}}}{2a_\Delta}} e^{-n\frac{a_\Delta}{\lambda_{\text{eff}}}}\right] + \sqrt{\frac{\pi\lambda_{\text{eff}}}{2a_\Delta}}\text{Li}_{-\frac{1}{2}}\left(e^{-\frac{a_\Delta}{\lambda_{\text{eff}}}}\right)\right\} \end{aligned} \tag{6.2}$$

with the polylogarithmic function $\text{Li}_{-\frac{1}{2}}(x)$ and $n_0 \gg \frac{\lambda_{\text{eff}}}{a_\Delta}$ [96]. For simplicity the vortices were assumed to be on circles with radius $n a_\Delta$ whereas the real triangular lattice is denser in space as it can be seen in figure 6.1. Thus the obtained B_{int} from (6.2) is expected to provide a lower bound for the exact internal magnetic flux density. The dependence on B_{ext} enters via the vortex spacing $a_\Delta \propto B_{\text{ext}}^{-1/2}$ according to equation (2.38).

In figure 6.2 the dependence of $B_{\text{int}}(B_{\text{ext}})$ on B_{ext} for different λ_{eff} can be seen. Although equation (6.2) does not depend explicitly on ξ_{GL} it is required $\lambda_{\text{eff}} \gg \xi_{\text{GL}}$ as well as $a_\Delta > \xi_{\text{GL}}$. It is only reasonable to compute B_{int} for $B_{\text{ext}} > B_{C1}$. So depending on the present B_{C1} and ξ_{GL} of the considered sample only a finite range of B_{ext} may be considered. It can be seen that for λ_{eff} in the order of μm the relation between B_{int} and B_{ext} is almost linear. For smaller λ_{eff}, B_{int} shows an exponential slope. Since Nb:$SrTiO_3$ has a big $\lambda_{\text{eff}} \sim \mu$m with a very small B_{C1} it is set

$$B_{\text{int}} = 0.81 B_{\text{ext}} \tag{6.3}$$

for further analysis. Figure 6.2 suggests that 0.81 is a reasonable proportionality constant.

Technically it was only calculated the $B_{\mathrm{int}}(r)$ for $r = 0$ at the center of a vortex while neglecting the magnetic flux density of that center vortex. It is commented on the question how strong the obtained B_{int} varies on space. Therefore the magnetic flux density $B_{\mathrm{vortex}}(r = \xi_{\mathrm{GL}})$ is calculated at the radius of a single vortex. The actual $B_{\mathrm{int}}(r)$ in the superconducting bulk will vary with maximal deviation $B_{\mathrm{vortex}}(r = \xi_{\mathrm{GL}})$. With equation (6.1), minimal $\lambda_{\mathrm{eff}} = 1.4\,\mu\mathrm{m}$ and minimal ratio $\xi^{l}_{\mathrm{GL}}/\lambda_{\mathrm{eff}} = 0.05$ from table 5.2 it is obtained

$$B_{\mathrm{vortex}}(r = \xi_{\mathrm{GL}}) = \frac{\Phi_0}{2\pi\lambda^2_{\mathrm{eff}}} K_0\left(\frac{\xi_{\mathrm{GL}}}{\lambda_{\mathrm{eff}}}\right) = 0.50\,\mathrm{mT} \tag{6.4}$$

as maximal deviation. With regard to the following calculation of the B_{int}-dependent optical conductivity and the critical magnetic flux densities of the Nb:$SrTiO_3$ samples in this thesis that go up to multiple values of 10 mT it is a convenient and sufficient choice to go with $B_{\mathrm{int}} = 0.81 B_{\mathrm{ext}}$.

6.2.2 Optical conductivity due to $\vec{B}$ dependent $\Delta(B)$

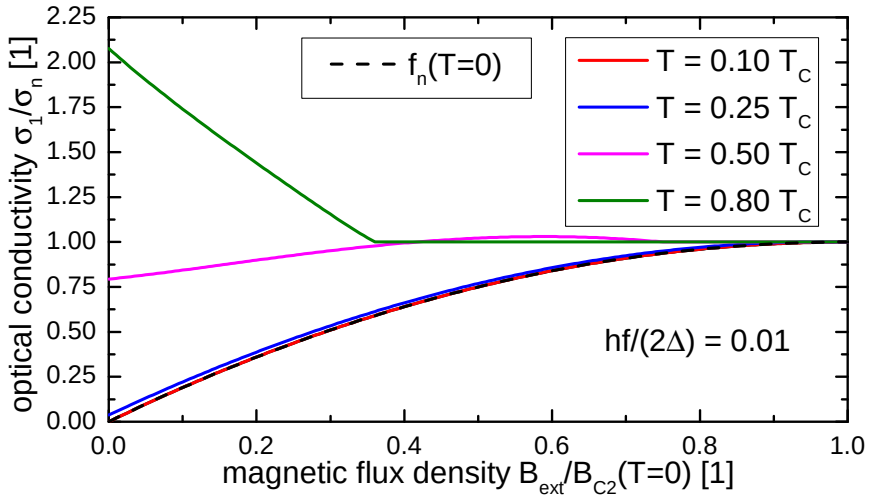

Fig. 6.3: Real part of the optical conductivity in equation (6.5) for frequency $hf/(2\Delta) = 0.01$ when assuming a DC conductivity for the vortices and the Mattis Bardeen prediction for the superconducting bulk along with the volume filling factor f_n from equation (6.6).

The previous subsection showed that high κ materials in the Shubnikov phase exhibit in the superconducting volume a relatively isotropic internal magnetic flux density $B_{\mathrm{int}} = a_{\mathrm{ext}} B_{\mathrm{ext}}$ that is directly proportional to the external magnetic flux density B_{ext}. A proportionality constant of $a_{\mathrm{ext}} = 0.81$ was obtained that will be used in the further analysis. Typical experiments with effects of a B-dependent Δ feature very thin samples so that the magnetic flux density can be assumed to be uniform in the superconductor [97, 98], it is reasonable to obtain the theoretical expression for the conductivity in analogy to these experiments but with replaced magnetic flux density $B \to B_{\mathrm{int}}$ for the energy gap $\Delta(T, B_{\mathrm{int}})$.

The total conductivity can be obtained with effective medium theory [99]. For analyzing experimental data effective medium theory typically consists of using Bruggeman's theory which features in the most simple case the computation of the mean conductivity

$$\hat{\sigma}_{\mathrm{mean}} = f_n(T, B_{\mathrm{ext}})\hat{\sigma}_{\mathrm{n}} + (1 - f_n(T, B_{\mathrm{ext}}))\hat{\sigma}_{\mathrm{sc}} \tag{6.5}$$

of the superconducting conductivity $\hat{\sigma}_{\mathrm{sc}}$ and normal conducting conductivity $\hat{\sigma}_{\mathrm{n}}$ of the vortex whereas the volume filling factor

$$f_n(T, B_{\mathrm{ext}}) = \frac{1 - \left(\frac{T_C(B_{\mathrm{ext}})}{T_C}\right)^4}{1 - \left(\frac{T}{T_C}\right)^4} = \frac{1 - \left(1 - \frac{B_{\mathrm{ext}}}{B_{C2}}\right)^2}{1 - \left(\frac{T}{T_C}\right)^4} \tag{6.6}$$

is the ratio of the normal conducting volume to the total volume in the superconductor [98].

To compute $\hat{\sigma}_{\mathrm{mean}}$ the conductivity of the vortex is set to the DC conductivity $\hat{\sigma}_{\mathrm{n}} = \sigma_{\mathrm{DC}}$. The superconducting bulk is set to the Mattis Bardeen prediction $\hat{\sigma}_{\mathrm{sc}}/\sigma_{\mathrm{DC}} = f_1^{\mathrm{MB}} + \mathrm{i}f_2^{\mathrm{MB}}$ according to equation (2.26). The energy gap $\Delta(T, B_{\mathrm{int}})$ that enters the Mattis Bardeen prediction, this means the energy gap $\Delta(T, B_{\mathrm{int}})$ in the superconducting volume of the Shubnikov phase for high κ materials, is given by [33, 97, 98]

$$\Delta(T, B_{\mathrm{int}}) = \Delta(T = 0, B_{\mathrm{int}} = 0) \cdot \sqrt{\cos\left(\frac{\pi}{2}\left(\frac{T}{T_C}\right)^2\right)} \cdot \sqrt{1 - \left(\frac{B_{\mathrm{int}}}{B_{\mathrm{C2}}(T)}\right)^2} \tag{6.7}$$

with

$$\frac{B_{C2}(T)}{B_{C2}(T = 0)} = 1 - \left(\frac{T}{T_C}\right)^2. \tag{6.8}$$

In figure 6.3 the real part of the optical conductivity in equation (6.5) can be seen for frequency $hf/(2\Delta(T = 0, B_{\mathrm{int}} = 0)) = 0.01$. For low temperatures the real part of the optical conductivity rises with decreasing slope for greater B_{ext} towards $\sigma_1 \to \sigma_{\mathrm{DC}}$. For $T = 0.5\,T_C$ the initial optical conductivity starts at $\sigma_1(B_{\mathrm{ext}} = 0) > 0.75\,\sigma_{\mathrm{DC}}$ and shows indeed a coherence peak although it is weakly developed. For $T = 0.8\,T_C$ at low B_{ext} the T-coherence peak can be seen, for greater B_{ext} the optical conductivity decreases to $\sigma_1 \to \sigma_{\mathrm{DC}}$ due to the linear increase of the normal conducting volume.

The coherence peak of σ_1 observed theoretically in figure 6.3 shows qualitatively different features than the experimentally observed B-coherence peak. There is no sharp initial rise of $\sigma_1(B_{\mathrm{ext}})$ in dependence of B_{ext} and only for temperatures close to T_C a very weak and broad maximum is observed. The theoretical computed σ_1 for $T = 0.8\,T_C$ in figure 6.3 resembles the behavior of $\sigma_1(B)$ in dependence of B for T close to T_C in figure 5.4 and 5.7, in that sense the model explains the decrease of σ_1 at temperatures where σ_1 is mainly characterized by the T-coherence peak. It is concluded that the B-coherence peak is not appropriately taken care of by assuming a B-dependence of Δ for the superconducting bulk in a composite model with normal conducting vortices.

6.3 Caroli-deGennes-Matricon mode

6.3.1 Introduction to the CdGM mode

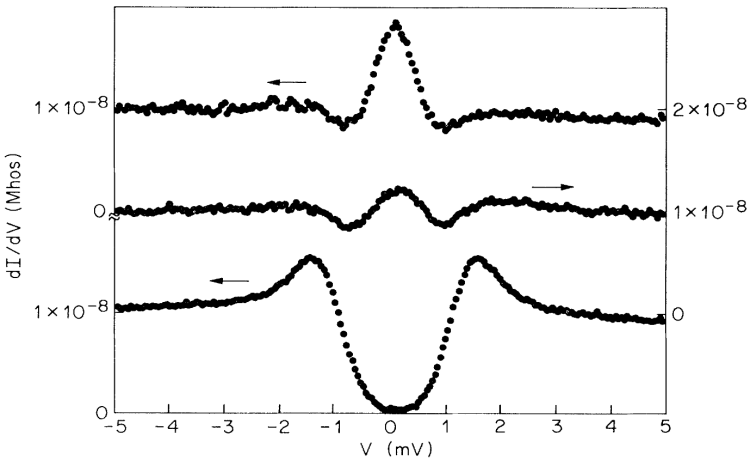

Fig. 6.4: Differential conductance $\mathrm{d}I/\mathrm{d}V$ in dependence of V measured with a tunneling scanning microscope. The material is superconducting $NbSe_2$ at $T = 1.85\,\mathrm{K}$ and $B = 0.02\,\mathrm{T}$, from top to down the data is observed at the vortex core and at distance 7.5 nm and 20 nm from the vortex core. Data taken from [100].

Caroli *et al.* found that low lying states with excitation energy $E_0 \sim \Delta^2/E_F$ are localized in the vortex core, these low lying states are referred to as Caroli-deGennes-Matricon modes [95]. Caroli *et al.* argued that for excitation energies above E_0 the density of states in the vortex core is comparable to that of a normal conducting cylinder of radius ξ_{GL}, thus the investigation by Caroli *et al.* is a microscopic justification for the Bardeen-Stephen model [33, 91, 95]. Scanning-tunneling-microscope (STM) measurements carried out by Hess *et al.* on $NbSe_2$ revealed a strong zero-bias peak of the differential conductance $\mathrm{d}I/\mathrm{d}V$ located at the Fermi energy in the vortex core whereas for greater distances from the vortex core the BCS prediction was reproduced [100, 101]. The observation by Hess *et al.* can be seen in figure 6.4. The finding of Hess *et al.* strongly suggests that the local DOS peaks $N_{\mathrm{loc}}(0) > N_{\mathrm{n}}(0)$ at the Fermi energy E_F. $N_{\mathrm{n}}(0)$ is the density of states in the normal conducting phase at the Fermi energy E_F. Other measurements that also show the mentioned peak can be found in [102, 103].

Theoretical investigations showed that the zero-bias peak of the differential conductance as measured by Hess *et al.* is a result of the low-lying CdGM mode. The local DOS was obtained by solving numerically the Bogoliubov-deGennes equations [104–106]. Most notable is the investigation by Gygi *et al.* who solved the Bogoliubov deGennes equations in a self-consistent manner [104]. In this section the investigation by Gygi will be repeated with some simplifications whereas it will be shown that the simplifications do not change significantly the result. After obtaining with theoretical methods the local DOS along with the peak at the vortex the optical conductivity will be computed.

6.3.2 Local DOS in a vortex due to the CdGM mode

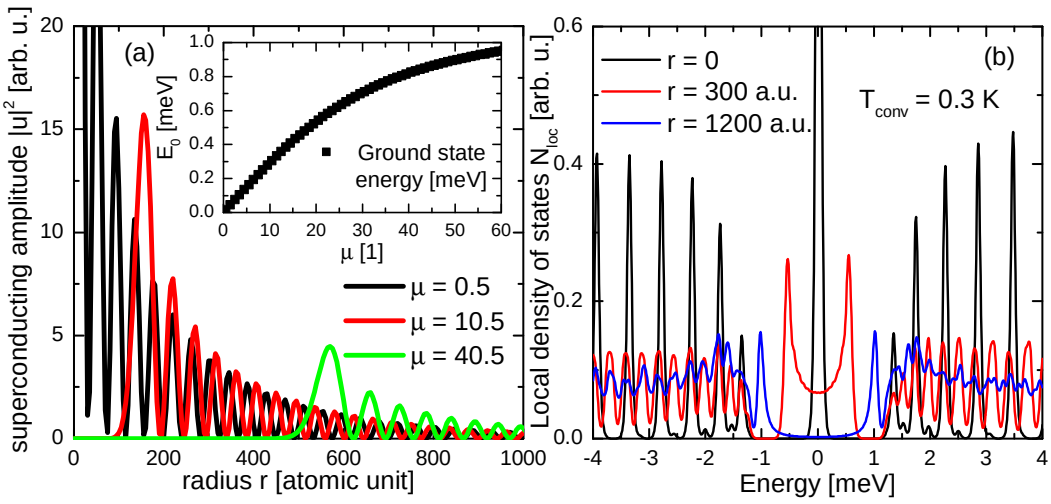

Fig. 6.5: In (a) the superconducting amplitude $|u(r)|^2$ in arbitrary units (arb. u.) for the lowest eigenvalue E_0 can be seen in dependence of the distance r from the vortex for chosen quantum angular number μ. In the inset of (a) the lowest energy E_0 of the bound state in dependence of μ can be seen. In (b) the local density of states N_{loc} for different positions r can be seen.

The BdG equations with parameters specified for $NbSe_2$ are solved in this chapter, most of this subsection is taken from [104]. The clean limit is assumed so that it can be set $U(\vec{r}) = 0$ in equation (2.19). Experimental data suggests that the peak of the local DOS survives as long as the material is not in the strong dirty limit [107]. It is further set $\vec{A} = 0$, the similar theoretical results of Shore *et al.* and Gygi *et al.* motivate this simplification [104, 105]. Since the vortex state has translational invariance along it's axis (here z-axis), the superconducting amplitudes are expressed as

$$\begin{aligned} u_i(\vec{r}) &= u_{n,\mu}(\vec{r}) e^{\mathrm{i}(\mu - 1/2)\theta} \\ v_i(\vec{r}) &= v_{n,\mu}(\vec{r}) e^{\mathrm{i}(\mu + 1/2)\theta} \end{aligned} \tag{6.9}$$

with the angular coordinate θ, the radial quantum number n and angular quantum number μ, the k_z dependence is neglected. The gauge of the energy gap is set to $\Delta(\vec{r}) = |\Delta(\vec{r})| e^{-\mathrm{i}\theta}$.

The superconducting amplitudes are now expanded on a disc $R = 5000\,\mathrm{a.u.}$, where a.u. is the atomic unit, in terms of functions

$$\phi_{j,m}(r) = \frac{\sqrt{2}}{R J_{m+1}(\alpha_{j,m})} J_m\left(\alpha_{j,m} \frac{r}{R}\right), \tag{6.10}$$

j goes from 1 to ∞ in integer steps and it is $m = \mu \pm 1/2$ and m is also integer. $\alpha_{j,m}$ is the jth zero of the Bessel function of the first kind $J_m(x)$. The $\phi_{j,m}$(r) fulfill the orthogonality relation

$$\int_0^R \phi_{j,m}(r)\phi_{j',m}(r) r \mathrm{d}r = 0 \tag{6.11}$$

for $j \neq j'$ [96]. The superconducting amplitudes are expressed as

$$\begin{aligned} u_{n,\mu}(r) &= \sum_j c_{n,\mu,j}\phi_{j,\mu-1/2}(r) \\ v_{n,\mu}(r) &= \sum_j d_{n,\mu,j}\phi_{j,\mu+1/2}(r) \end{aligned} \tag{6.12}$$

with complex coefficients $c_{n,\mu,j}$ and $d_{n,\mu,j}$. With the vector $\Psi_{n,\mu}^T = (\{c_{n,\mu,j}\}_{j=1}^{N_{\max}}, \{d_{n,\mu,j}\}_{j=1}^{N_{\max}})$ with $N_{\max} = 250$ the BdG equation can be expressed as $2N_{\max} \times 2N_{\max}$ matrix eigenvalue problem

$$\begin{bmatrix} T^- & \tilde{\Delta} \\ \tilde{\Delta}^T & T^+ \end{bmatrix} \Psi_{n,\mu} = E_{n,\mu}\Psi_{n,\mu} \tag{6.13}$$

with

$$T_{j,j'}^{\pm} = \mp \left[\frac{\hbar^2}{2m} \frac{\alpha_{j,\mu\pm1/2}^2}{R^2} - E_F \right] \delta_{j,j'} \tag{6.14}$$

and

$$\tilde{\Delta}_{j,j'} = \int_0^R \phi_{j,\mu-1/2}(r)|\Delta(r)|\phi_{j',\mu+1/2}(r) r \mathrm{d}r. \tag{6.15}$$

As $\Delta(r)$ an absolute value of $\Delta(r \to \infty) = 1.2\,\mathrm{meV}$ is used with an r dependence according to equation (2.36) with $\xi_{\mathrm{GL}} = 200\,\mathrm{a.u.}$, the Fermi energy is set to $E_F = 38.5\,\mathrm{meV}$ and the effective mass to $m = 2m_e$. It is noted that the $\mp$ sign in equation (6.14) is missing in [104] in equation (9), this is an error in the original publication. Solving equation (6.13) returns $2N_{\max}$ eigenvectors $\Psi_{n,\mu}$ for a specific μ with $1 \leq n \leq 2N_{\max}$ and n is integer. Equation (6.13) is solved for $1/2 \leq \mu \leq 550 + 1/2$ whereas μ is half of an odd integer, this means for 550 values of μ. The BdG equations are not solved in a self-consistent manner as in [104]. A self-consistent solution is obtained by using the solution of equation (6.13) to calculate $\Delta(r)$, by reinserting $\Delta(r)$ into equation (6.13) and solving again multiple times until $\Delta(r)$ converged.

In figure 6.5 in (a) the computed superconducting amplitude $|u_i|^2$ for the lowest eigenvalue $E_{n,\mu}$ for different μ can be seen, the behavior of u in figure 6 in [104] is reproduced. The low-lying CdGM-modes are localized in the vortex core and the maximum of $|u|$ moves to greater distances for greater quantum angular momentum number μ. In the inset of figure (a) the dependence of E_0 can be seen on μ, E_0 initially increases linearly and levels off towards the value of the energy gap 1.2 meV. The inset in figure (a) reproduces figure 3 in [104]. The local density of states $N_{\mathrm{loc.}}$ is expressed as

$$N_{\mathrm{loc}}(r, E) = -\sum_{i=n,\mu} \left[u_i^2(r) f_F'(E - E_{n,\mu}, T_{\mathrm{conv}}) + v_i^2(r) f_F'(E + E_{n,\mu}, T_{\mathrm{conv}}) \right] \tag{6.16}$$

with the derivative of the Fermi distribution from equation (2.16). N_{loc} is convoluted with the Fermi distribution to reduce errors that could enter due to the discretization of the energy states $E_{n,\mu}$. $T_{\mathrm{conv}} = 0.3\,\mathrm{K}$ was found to be a fitting value. In figure 6.5 in (b) N_{loc} can be seen. The peak of $N_{\mathrm{loc}}(r, E)$ at $r = 0$, $E = 0$ splits and moves to greater energies $|E|$ for greater distance from the vortex. The structure beyond the energy gap $|E| > 1.2\,\mathrm{meV}$ results from the finite disc size $R = 5000\,\mathrm{a.u.}$ of the numerical computation. For the evaluation of the optical conductivity due to N_{loc} the structure for $|E| > 1.2\,\mathrm{meV}$ plays no role for sufficient low temperature T and low frequency $hf \ll 2\Delta$. For further investigations N_{loc} is averaged for $|E| > 1.2\,\mathrm{meV}$ and fitted with a constant value whereas 0.07358 is obtained, this way N_{loc} can be normalized by dividing with 0.07358.

6.3.3 Optical conductivity due to the CdGM mode

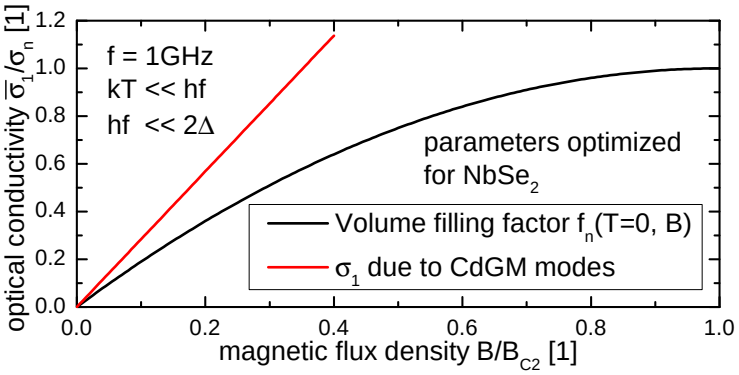

Fig. 6.6: Optical conductivity as obtained from equation (6.23) up to $B/B_{C2} = 0.4$ together with the volume filling factor in equation (6.6).

The optical conductivity can be obtained from equation (2.24), in fact the Mattis Bardeen equations follow from entering the BCS prediction into equation (2.24). Since the superconducting amplitudes are now complex the coherence factor F must be determined from first hand principles. The interaction hamiltonian is given by

$$\mathcal{H}_I = \sum_{\vec{k}\sigma,\vec{k}'\sigma'} B_{\vec{k}'\sigma',\vec{k}\sigma} c^*_{\vec{k}'\sigma'} c_{\vec{k}\sigma} \tag{6.17}$$

with the matrix elements of the perturbing operator $B_{\vec{k}'\sigma',\vec{k}\sigma}$. The annihilation and creation operator are expressed as linear superposition of the Bogoliubov operators

$$\begin{aligned} c_{\vec{k}\uparrow} &= u^*_{\vec{k}} \gamma_{\vec{k}0} + v_{\vec{k}} \gamma^*_{\vec{k}1} \\ c^*_{-\vec{k}\downarrow} &= -v^*_{\vec{k}} \gamma_{\vec{k}0} + u_{\vec{k}} \gamma^*_{\vec{k}1}. \end{aligned} \tag{6.18}$$

With the behavior of the matrix transition elements that is typical for case II coherence factor $B_{\vec{k}'\uparrow,\vec{k}\uparrow} = -B_{-\vec{k}'\downarrow,-\vec{k}\downarrow}$ it can be obtained

$$c^*_{\vec{k}'\uparrow}c_{\vec{k}\uparrow} - c^*_{-\vec{k}\downarrow}c_{-\vec{k}'\downarrow} = \left(u_{\vec{k}'}u^*_{\vec{k}} + v^*_{\vec{k}}v_{\vec{k}'}\right)\gamma^*_{\vec{k}'0}\gamma_{\vec{k}0} - \left(v^*_{\vec{k}'}v_{\vec{k}} + u_{\vec{k}}u^*_{\vec{k}'}\right)\gamma^*_{\vec{k}1}\gamma_{\vec{k}'1}, \tag{6.19}$$

the terms that are associated with the creation and annihilation of quasi-particles are neglected since scattering is the main mechanism that contributes to the optical conductivity. It is straightforward to see that assuming real superconducting amplitudes allows to put together both terms in equation (6.19), this way the coherence factor $F = (uu' + vv')$ can be defined whereas further analysis within the BCS framework results in equation (2.25). So far the analysis followed the derivation of F by Tinkham [33].

It is now assumed that the superconducting state is probed at sufficiently small frequencies such that it can be set $\vec{k} \sim \vec{k}'$. This means that hf should be at the order of magnitude of Δ_0^2/E_F, this assumption may hold specifically for Nb:$SrTiO_3$ due to the very small Fermi energy. This way and with a fitting normalization it is obtained as coherence factor

$$F = |u_{\vec{k}}|^2 + |v_{\vec{k}}|^2 = 1. \tag{6.20}$$

For simplicity it is assumed $kT \ll hf$, in fact if this assumption would not be fulfilled it would mean that equation (2.24) must be integrated, a more cumbersome task that is expected to return qualitatively the same results. Since the B-coherence peak appears for low frequencies and is most pronounced towards low temperatures, these approximations are reasonable. This way it can be obtained from equation (2.24)

$$\sigma_1(r,f)/\sigma_{\mathrm{DC}} = N_{\mathrm{loc}}\left(r, -\frac{hf}{2}\right)N_{\mathrm{loc}}\left(r, \frac{hf}{2}\right) \tag{6.21}$$

for the frequency- and position-dependent optical conductivity $\sigma_1(r,f)$.

Averaging the position-dependent conductivity $\sigma_1(r,f)$ allows to obtain the experimentally observable real part of the optical conductivity $\bar{\sigma}_1$. It suffices to integrate $\sigma_1(r,f)$ over the surface of a circle with radius $a_\Delta/2$, this way it is obtained

$$\bar{\sigma}_1 = \frac{8}{a_\Delta^2}\int_0^{a_\Delta/2} \mathrm{d}r\, r\sigma_1^{\mathrm{loc}}(r). \tag{6.22}$$

It is seen that a linear B-dependence enters via a_Δ. Equation (6.22) holds for big enough vortex spacing $a_\Delta > 2\gamma\xi_{\mathrm{GL}}$. For simplification the integral in equation (6.22) can be cut off at $\gamma\xi_{\mathrm{GL}}$ since for great distance r from the vortex core $\sigma_1(r,f)$ decreases to 0. Here γ is introduced as cut-off variable, great values for γ allow to consider features of $\sigma_1(r,f)$ that may be further located from the vortex center, smaller values for γ neglect those features to extend the optical conductivity to greater values of B/B_{C2}. It is found that $\gamma = 1$ is a

reasonable choice. With equation (2.38) and (2.39) and setting the integral to zero for values $\rho' > \gamma\xi_{\mathrm{GL}}$ it is obtained

$$\bar{\sigma}_1 = \frac{B}{B_{C2}} \cdot \frac{\sqrt{3}}{2\pi} \frac{1}{\xi_{\mathrm{GL}}^2} \int_0^{\gamma\xi_{\mathrm{GL}}} \mathrm{d}\rho' \rho' \sigma_1^{\mathrm{loc.}}(\rho') \tag{6.23}$$

as long as $a_\Delta > 2\gamma\xi_{\mathrm{GL}}$. From $a_\Delta > 2\gamma\xi_{\mathrm{GL}}$ it follows that only values up to $B/B_{C2} = \pi/(\gamma^2\sqrt{3}) = 0.45$ should be considered.

In figure 6.6 the optical conductivity from equation (6.23) due to the CdGM modes can be seen along with the volume filling factor $f_n(T = 0, B)$ from equation (6.6). The volume filling factor f_n accounts reasonably well for $\bar{\sigma}_1$ at low temperatures as it was established in figure 6.3. For small B the slope of $\bar{\sigma}_1$ is greater than the slope of f_n, this a characteristic feature of the B-coherence peak. Also the peak persists at low temperatures T. But the order of magnitude of the B-coherence peak of Nb:$SrTiO_3$ is stronger. In the case of an unconventional superconductor like Nb:$SrTiO_3$ additional effects could play a role in the strong enhancement in the conductivity of $\bar{\sigma}_1$. It is noted that for $B/B_{C2} \sim 0.4$, $f_n(T = 0, B)$ starts to deviate slightly from the linear slope. For $B > 0.4\,B_{C2}$ the vortices are expected to interact, assuming overlapping vortices results in an effectively lowered gap Δ and the CdGM modes with the highest energy turn into Bloch waves thus resulting in $\bar{\sigma}_1 \to \sigma_{\mathrm{DC}}$ for $B \to B_{C2}$. It is concluded that low-lying states in the vortex core can produce a feature similar to the B-coherence peak. A more detailed investigation should address how $\bar{\sigma}_1$ evolves towards B_{C2} and make a quantified statement on the maximum value of $\bar{\sigma}_1$.

6.3.4 Maximum of the B-coherence peak

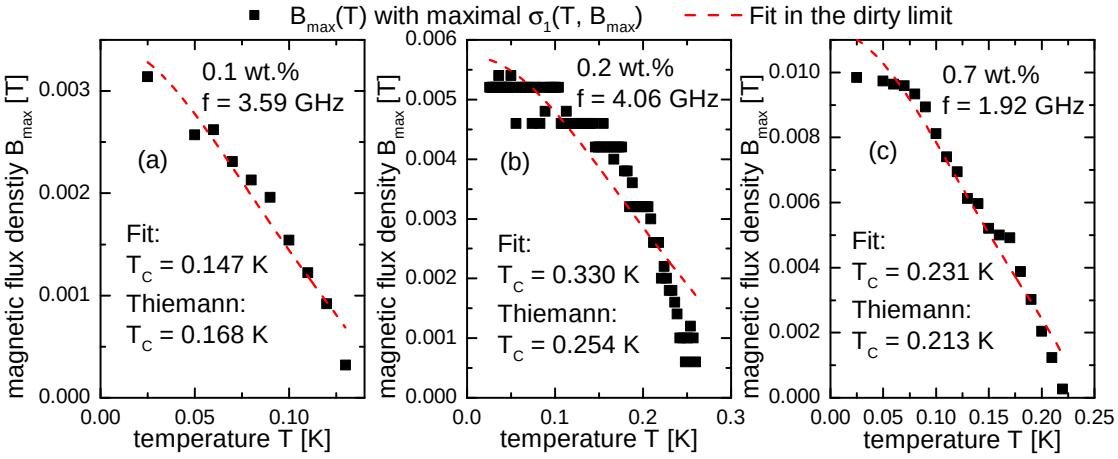

Fig. 6.7: Magnetic flux density $B_{\max}(T)$ where $\sigma_1(T, B_{\max})$ is maximal for the samples investigated in this thesis. The respective optical conductivity can be seen in figure 5.4, 5.10 and 5.7. The data is fitted with equation (6.26). The T_C according to Thiemann is taken from [17].

The preceding subsection established low-lying condensed states in the vortex core as possible explanation for the B-coherence peak. The maximum of $\sigma_1(B = B_{\max})$ at magnetic flux density $B_{\max}$ is reached for a critical spacing of the vortices so that a closer spacing would result in overlapping vortices and a more remote spacing in less vortices with enhanced conductivity. As result it follows as condition for the maximum of the B-coherence peak

$$\eta_{\max}\xi_{\mathrm{GL}} = a_{\Delta}(B = B_{\max}). \tag{6.24}$$

The critical spacing constant $\eta_{\max}$ is introduced, since the B-coherence peak shows a frequency dependence the critical spacing constant may depend on frequency $\eta_{\max}(f)$. Here it is focused on the temperature dependence of ξ_{GL} and a_{Δ}. With equation (2.32) and (2.38) and the experimentally verified relation $B_C(T) = B_C(T = 0)(1 - (T/T_C)^2)$ and the penetration depth in the clean limit $\lambda_{\mathrm{eff}}(T) = \lambda_{\mathrm{eff}}(T = 0)(1 - (T/T_C)^4)^{-1/2}$ it is obtained

$$\frac{B_{\max}(T)}{B_{C2}(T = 0)} = \frac{4\pi}{\sqrt{3}\eta_{\max}^2}\frac{1 - \left(\frac{T}{T_C}\right)^2}{1 + \left(\frac{T}{T_C}\right)^2}. \tag{6.25}$$

In the dirty limit $\lambda_{\mathrm{eff}}(T) = \lambda_{\mathrm{eff}}(T = 0)(1 - (T/T_C)^4)^{-3/4}$ can be used as approximate temperature dependence [33], it is then obtained

$$\frac{B_{\max}(T)}{B_{C2}(T = 0)} = \frac{4\pi}{\sqrt{3}\eta_{\max}^2}\frac{\left(1 - \left(\frac{T}{T_C}\right)^2\right)^{\frac{1}{2}}}{\left(1 + \left(\frac{T}{T_C}\right)^2\right)^{\frac{3}{2}}}. \tag{6.26}$$

Here $B_{\max}(T)$ is the magnetic flux density where $\sigma_1(B)$ is maximal. Considering the experimental evidence of Thiemann [17] that the present $SrTiO_3$ samples are in the dirty limit, equation (6.26) is used to fit the experimentally obtained $B_{\max}(T)$. In fact equation (6.25) and (6.26) show a relatively similar temperature dependence. Accordance of the fit with experimental data can be understood as indication that conductivity enhancing effects in the vortex core are the mechanism behind the B-coherence peak.

In figure 6.7 $B_{\max}(T)$ can be seen for the samples that are investigated in this thesis. The data does no suggest a consistent behavior for the measured samples. The fit returns values for T_C that are in reasonable agreement with previous measurements by Thiemann except for the 0.2 wt.% sample. The fit to $B_{\max}(T)$ does not cover the behavior of the data. This may be attributed to difficulties in obtaining the correct values of $B_{\max}(T)$, but it is also assumed that the correct temperature dependence of $\xi_{\mathrm{GL}}(T)$ is deviating from the derived temperature dependence in this subsection. For $T \leq T_C$ it is typically approximated $\xi_{\mathrm{GL}}^{-2}(T) \propto 1 - T/T_C$ [33], the linear temperature dependence of $B_{\max}(T)$ for $T \leq T_C$ can be observed for all considered samples. In that sense the observed $B_{\max}(T)$ can be seen with caution as indication that vortices in Nb:$SrTiO_3$ display enhanced conductivity.

6.4 Clean and dirty limit

It is appropriate to discuss whether the investigated Nb:$SrTiO_3$ samples in this thesis are in the dirty or clean limit. The expression for the conductivity

$$\vec{J}_{\mathrm{sc}}(\vec{r}) = -\frac{3}{4\pi\mu_0\xi_\Delta\lambda_L^2}\int_{\mathbb{R}^3}\frac{\vec{R}\left[\vec{R}\cdot\vec{A}(\vec{r}')\right]}{R^4}J(R,T)\mathrm{e}^{-R/l}\mathrm{d}\vec{r}' \tag{6.27}$$

is considered with $R = |\vec{R}|$ and $\vec{R} = \vec{r} - \vec{r}'$ [33]. The similarity to equation (2.23) is noted, the exponential e^{-R/ξ_Δ} is replaced by the similar behaving kernel function $J(R,T)$ in the framework of the BCS theory and in a phenomenological approach the effect of the free mean path is accounted for by an additional exponential $e^{-R/l}$. The integral (6.27) can be transformed into a local relation $\vec{J}_{\mathrm{sc}}(\vec{r}) \propto \vec{A}(\vec{r}')$ depending on the length scale λ_L, ξ_Δ and l, from the relation of those length scales to each other follows the distinction into the local and non-local limit and the dirty and clean limit. The local relation is obtained when $\vec{A}(\vec{r})$ varies slowly compared to $J(R,T)\exp(-R/l)$. The respective limits are considered in subsection 2.2.4.

The length scales of the samples measured in this thesis ξ_Δ and l are in a similar order of magnitude, the obtained values can be seen in table 5.2, ξ_{GL} and ξ_Δ do not differ significant due to equation (2.34). As result Nb:$SrTiO_3$ may display properties of clean and dirty superconductors. Renner *et al.* observed that the zero-bias conductivity peak that was measured by Hess *et al.* decreases when the superconductor is driven from the clean to the dirty limit, the peak vanishes completely in the strong dirty limit [107]. Thiemann calculated the averaged DOS of a two-gap superconductor and showed that already for moderate scattering $2\pi^2\xi_\Delta/l = \hbar\Gamma/\Delta \geq 1$ the gaps merged, consistent with their experimental observations [17].

Collignon *et al.* observed a departure of the superfluid density n_{sc} from the charge carrier density n for a doping that is comparable to the samples that are investigated in this thesis [19]. This is interpreted as a transition from the clean to the dirty limit. Although the values in table 5.2 contain uncertainties, it can be seen that for the lowest doped sample $l > \xi_{\mathrm{GL}}$ and for the highest doped sample $l < \xi_{\mathrm{GL}}$ thus suggesting a transition from the clean to the dirty limit whereas for all doping concentrations the bare values of l, ξ_{GL} are in a comparable order of magnitude. Nb:$SrTiO_3$ may be a material that exhibits properties of both the dirty and clean limit to a varying extent.

7 Summary

In this thesis the optical conductivity of Nb-doped $SrTiO_3$ was obtained. The five samples investigated in this thesis have charge carrier concentrations $n_{\mathrm{Hall}} = 0.33 \cdot 10^{20}\,\mathrm{cm}^{-3}$, $n_{\mathrm{Hall}} = 0.59 \cdot 10^{20}\,\mathrm{cm}^{-3}$, $n_{\mathrm{Hall}} = 1.1 \cdot 10^{20}\,\mathrm{cm}^{-3}$, $n_{\mathrm{Hall}} = 2.0 \cdot 10^{20}\,\mathrm{cm}^{-3}$, $n_{\mathrm{Hall}} = 2.2 \cdot 10^{20}\,\mathrm{cm}^{-3}$. Superconducting Stripline resonators were used to probe the optical properties of Nb:$SrTiO_3$. Stripline resonator made of superconductors such as lead and tin display a change in resonance frequency f due to the temperature dependent properties of the superconducting material, it was shown that this temperature dependence can be related to the effective London penetration depth λ_{eff} and fitting absolute values for the effective London penetration of lead and tin were found. When a ground plane of the lead stripline resonator is replaced by a Nb:$SrTiO_3$ sample, the optical conductivity of Nb:$SrTiO_3$ can be obtained with the cavity perturbation technique.

The optical conductivity of Nb:$SrTiO_3$ reveals features that are typically associated with a dirty single-gap superconductor. At low frequencies the coherence peak predicted by the BCS theory, here referred to as T-coherence peak, is observed. Real and imaginary part of the optical conductivity display in dependence of the magnetic flux density B an abrupt change of slope, this means a kink at B^*. At the critical magnetic flux densities B^* and B_{C2} the two superconducting bands with two coherence lengths ξ_{GL} in Nb:$SrTiO_3$ are respectively depleted. Starting at $B = 0$ the real part of the optical conductivity σ_1 displays a strong increase of σ_1 in dependence of B even at lowest achieved temperature T and it is observed $\sigma_1 > \sigma_{\mathrm{DC}}$. The behavior of σ_1 in dependence of B is reminiscent of the T-coherence peak since both features are only observed for low frequencies $hf \ll 2\Delta$, but are qualitatively different since for the T-coherence peak σ_1 peaks towards $T \leq T_C$ whereas for the B-dependence of σ_1 a sharp initial slope is observed that is greater than it would expected from assuming normal conducting vortices. Thus the just described characteristics of the B-dependence of σ_1 are referred to as B-coherence peak.

The dome of critical fields B^*, B_{C2} suggests $T_C^2 \propto B^*$ and $T_C^2 \propto B_{C2}$. With the BCS and Ginzburg Landau theory it can be obtained $\Delta_0 \propto (E_F B^\alpha/m)^{1/2}$ in the clean limit and $\Delta_0 \propto lB^\alpha\,(E_F/m)^{1/2}$ in the dirty limit, here it is $B^\alpha = B^*, B_{C2}$. A relation between the ratio of the critical magnetic flux densities and the ratio of the effective masses of the lower band m^l and the middle band m^m, $B_{C2}^2/B^{*2} = m^l/m^m$ can be obtained in the dirty limit when the Fermi energy E_F and the free mean path l are assumed to be the same for both bands, the relation is supported by experimental data. The Fermi energy can be obtained, in the clean limit the Fermi energy displays a dome and in the dirty limit a monotonous increase in dependence of doping.

A characteristic feature of the B-coherence peak, the strong initial increase of σ_1 in dependence of B down to lowest temperature T, could be reproduced with a theoretical

argument. The Caroli-deGennes-Matricon modes are low-lying states localized in the vortex core that cause a sharp peak in the local density of states $N_{\mathrm{loc.}}(r, E)$ in the vortex core at the Fermi energy E_F. The local density of states $N_{\mathrm{loc.}}(r, E)$ due to those low-lying states results in a slope $\sigma_1/\mathrm{d}B|_{B=0}$ that is greater than it would be expected from assuming normal-conducting vortices with the Ginzburg Landau coherence length ξ_{GL} as radius.

The discussion whether Nb:$SrTiO_3$ is best described in the dirty or clean limit is not settled. Arguing on the basis of the length scales l and ξ_{GL} a transition from the clean to the dirty limit is observed with greater doping for the samples investigated in this thesis. The values of l and ξ_{GL} are in a similar order of magnitude, as result the Nb:$SrTiO_3$ samples in this thesis are not tuned from the strong clean to the strong dirty limit. Nb:$SrTiO_3$ may be a material that displays properties that are characteristic for superconductors in the clean and dirty limit.

8 Outlook

Research on superconducting doped $SrTiO_3$ seems to gain momentum in the last years. A few open questions that are of relevance, at least to the author, are listed here.

The peak of the local density of states in the vortex state due to the Caroli-deGennes-Matricon modes is typically associated with a shrinking of the vortex core, namely the Kramer-Pesch effect [108]. It is assumed that the Kramer-Pesch effect may be observable as unusual slope of the conductivity $\mathrm{Re}(\hat{\sigma})$ in dependence of temperature T for finite magnetic flux density B. Observing the Kramer-Pesch effect may validate the hypothesis that low-lying states in the vortex core cause the B-coherence peak. In addition a detailed temperature dependent measurement of $\hat{\sigma}$ may allow to track the energy gap Δ for different magnetic flux densities B more readily. In fact the experimental observation of $\Delta(B)$ in the case of $Nb:SrTiO_3$ would be highly desirable.

STM measurements of the vortex state of $Nb:SrTiO_3$ may provide the most fruitful contribution to the mystery behind the B-coherence peak. It is apparent that the rich vortex structure of a superconductor is averaged to obtain the macroscopic observable optical conductivity $\hat{\sigma}$. The B-coherence peak with the unusual characteristics is teasing towards a greater surprise that may be revealed with the help of STM measurements. In addition it is not clear whether $Nb:SrTiO_3$ is the only material that displays the B-coherence peak. Comparable studies on reference materials may provide insight into a so far insufficient investigated topic in the field of superconductivity.

Also the discrepancy between the obtained absolute values of the Fermi energy in this thesis and from theoretical studies should be investigated. Whereas the ratio of the upper magnetic flux densities where the two bands of $SrTiO_3$ are respectively depleted may be straightforwardly related to an experimentally confirmed ratio of effective masses in the dirty limit, it is not clear why the obtained absolute values of the Fermi energy are smaller than the theoretical prediction [82]. A theoretical investigation should also clarify how Cooper-pairs of two bands that couple in k-space can exhibit in real space two different coherence lengths.

Appendix

Optical conductivity of Nb:$SrTiO_3$

All measured optical conductivities $\hat{\sigma}$ that are not shown in the main text are shown here.

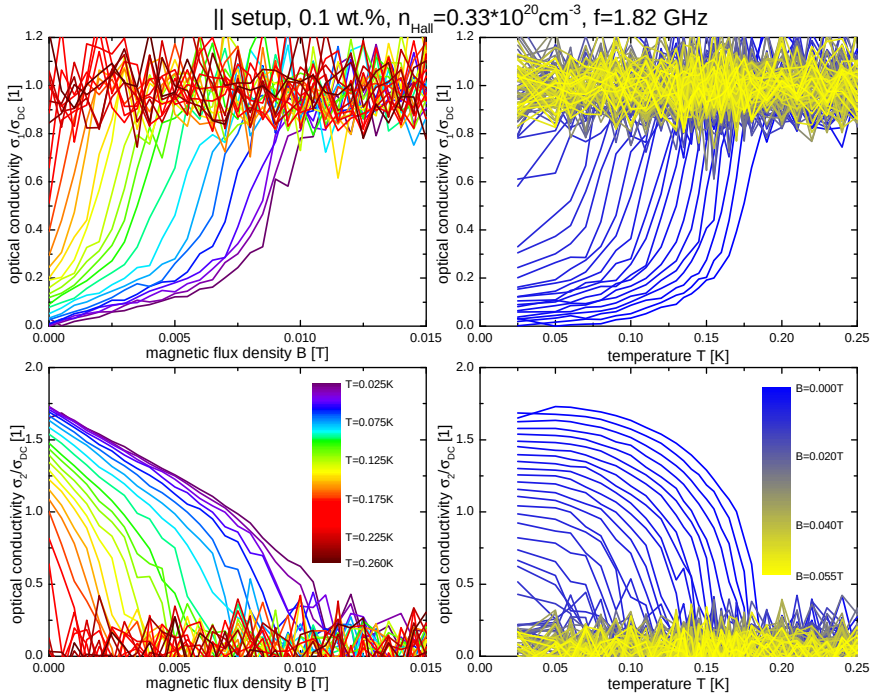

Fig. 8.1: Optical conductivity of the 0.1 wt. % Nb-doped $SrTiO_3$ sample at $f = 1.82\,\mathrm{GHz}$ in || orientation.

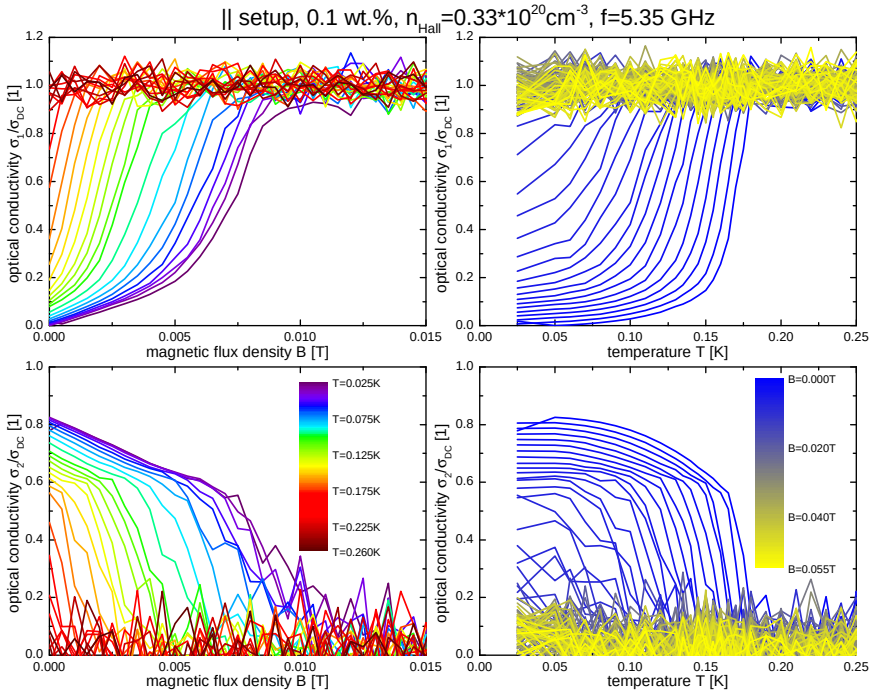

Fig. 8.2: Optical conductivity of the 0.1 wt. % Nb-doped $SrTiO_3$ sample at $f = 5.35\,\mathrm{GHz}$ in || orientation.

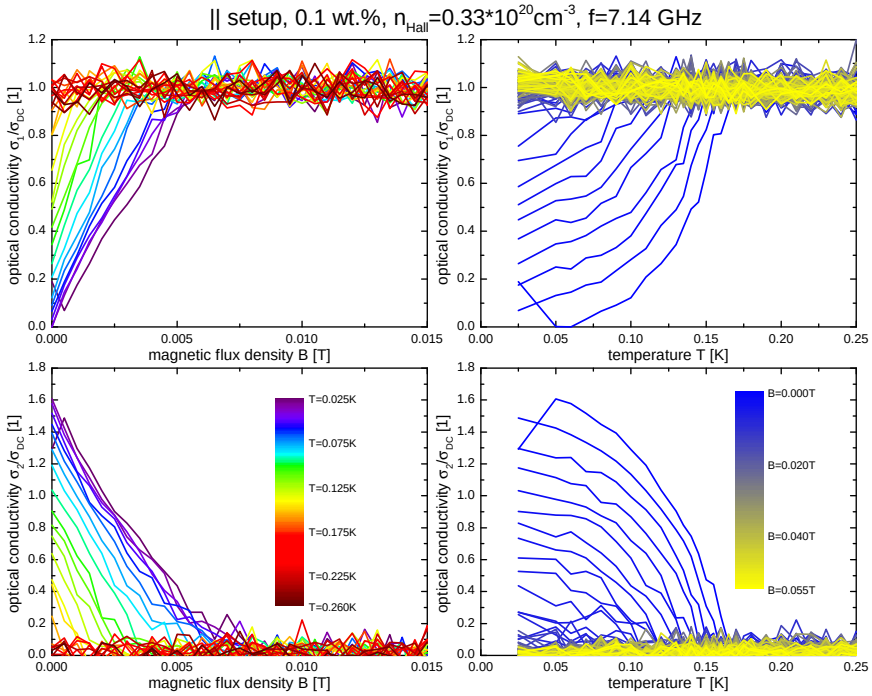

Fig. 8.3: Optical conductivity of the 0.1 wt. % Nb-doped $SrTiO_3$ sample at $f = 7.14\,\mathrm{GHz}$ in || orientation.

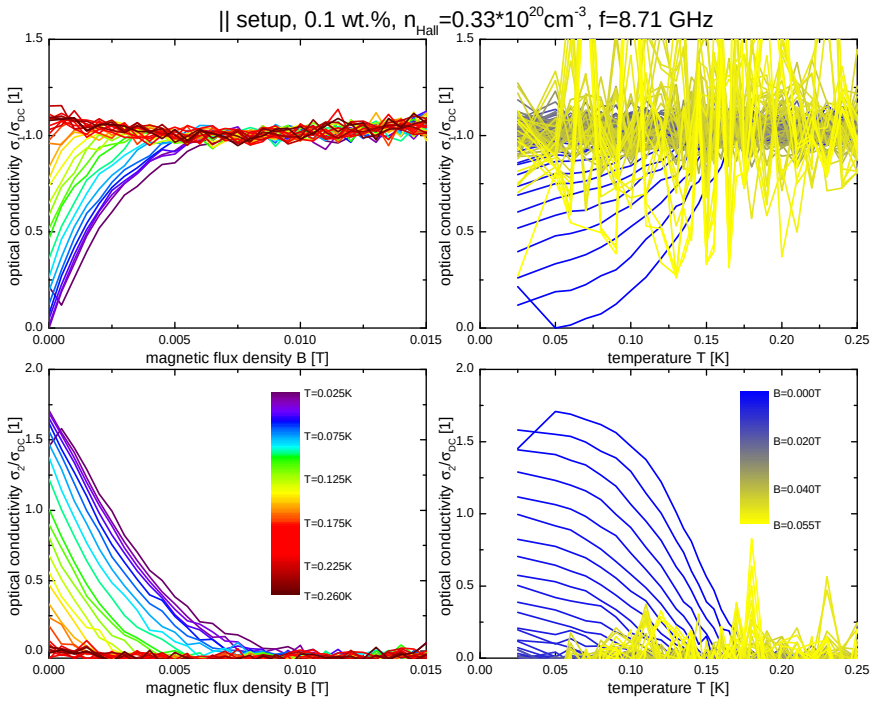

Fig. 8.4: Optical conductivity of the 0.1 wt. % Nb-doped $SrTiO_3$ sample at $f = 8.71\,\mathrm{GHz}$ in || orientation.

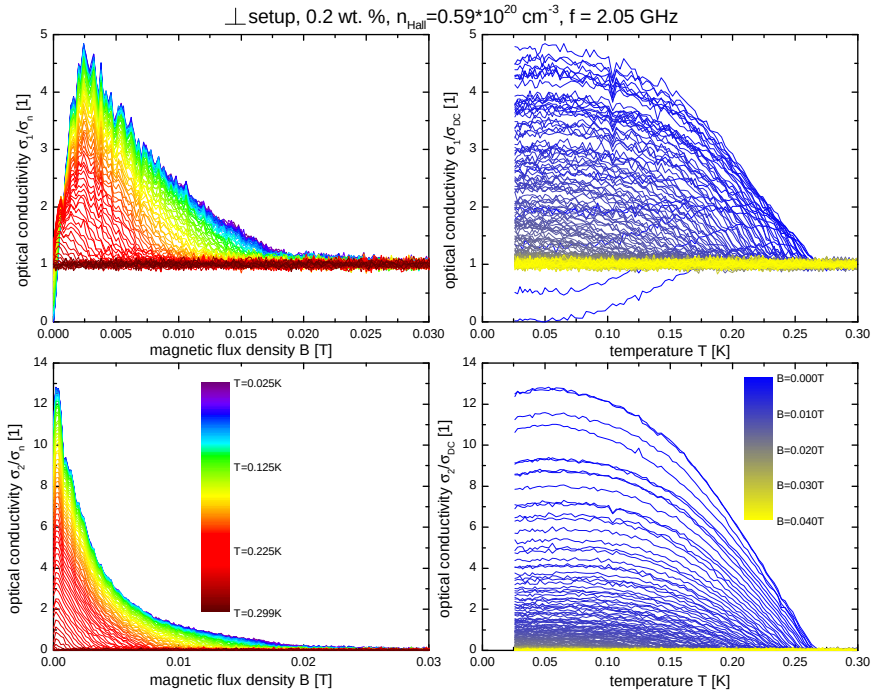

Fig. 8.5: Optical conductivity of the 0.2 wt. % Nb-doped $SrTiO_3$ sample at $f = 2.05\,\mathrm{GHz}$ in ⊥ orientation.

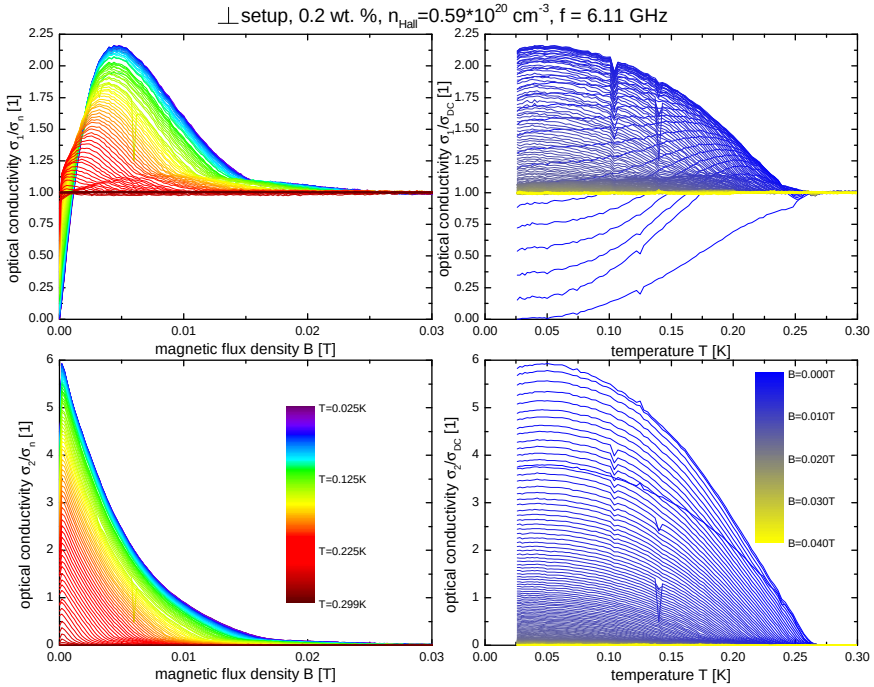

Fig. 8.6: Optical conductivity of the 0.2 wt. % Nb-doped $SrTiO_3$ sample at $f = 6.11\,\mathrm{GHz}$ in $\perp$ orientation.

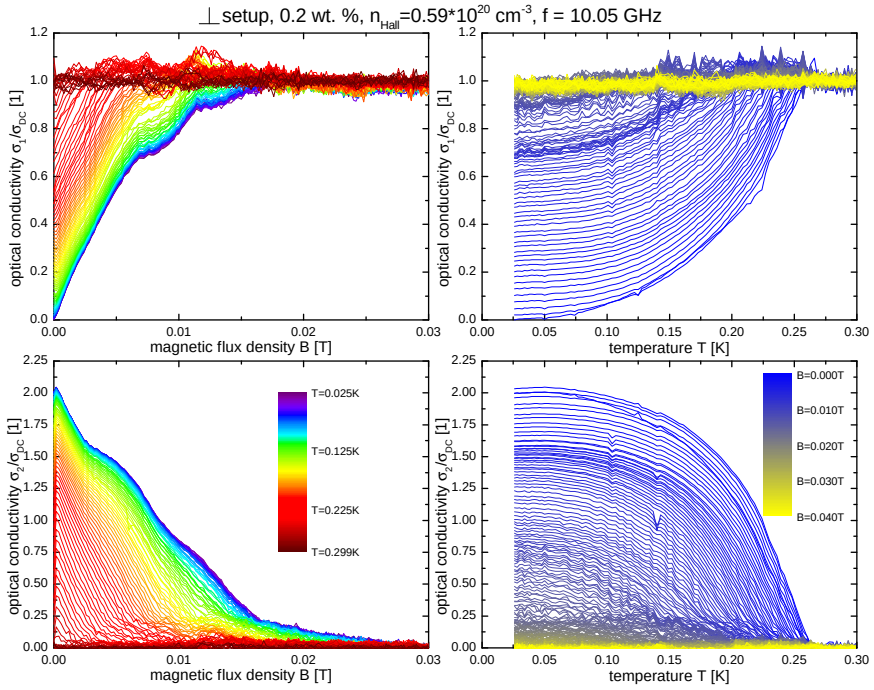

Fig. 8.7: Optical conductivity of the 0.2 wt. % Nb-doped $SrTiO_3$ sample at $f = 10.05\,\mathrm{GHz}$ in $\perp$ orientation.

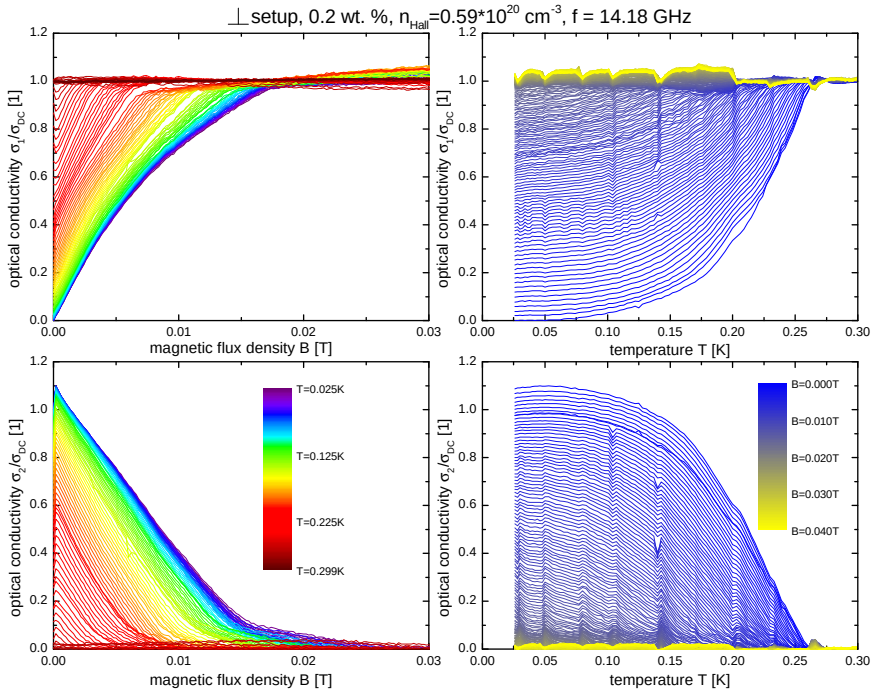

Fig. 8.8: Optical conductivity of the 0.2 wt. % Nb-doped $SrTiO_3$ sample at $f = 14.18$ GHz in $\perp$ orientation.

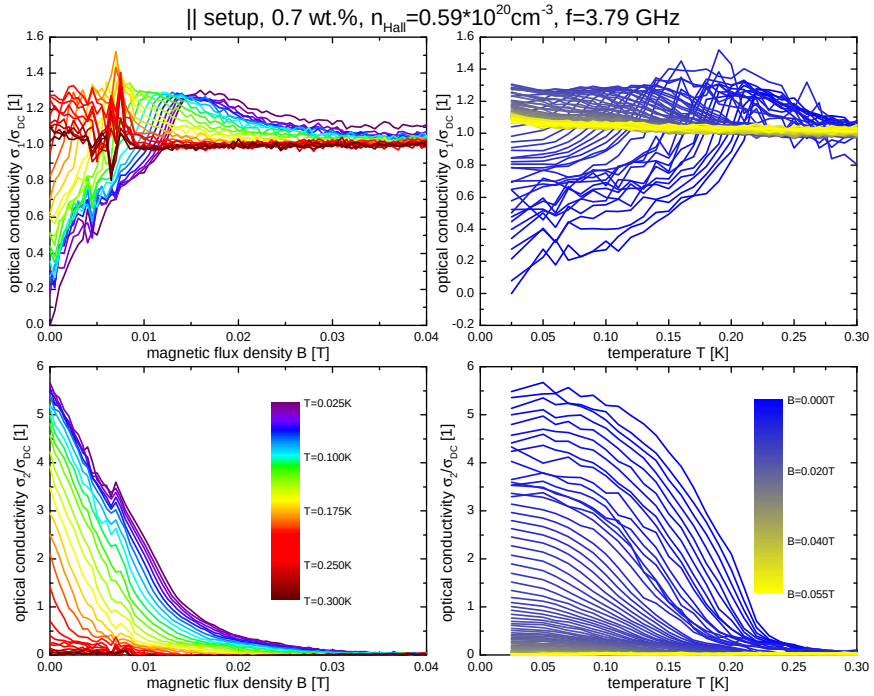

Fig. 8.9: Optical conductivity of the 0.7 wt. % Nb-doped $SrTiO_3$ sample at $f = 3.79$ GHz in || orientation.

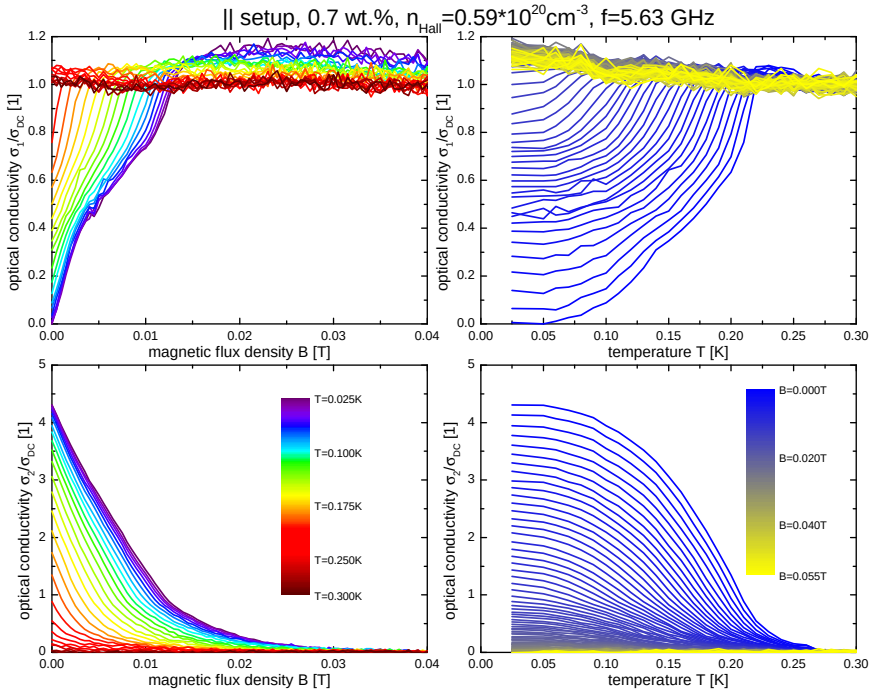

Fig. 8.10: Optical conductivity of the 0.7 wt. % Nb-doped $SrTiO_3$ sample at $f = 5.63\,\mathrm{GHz}$ in || orientation.

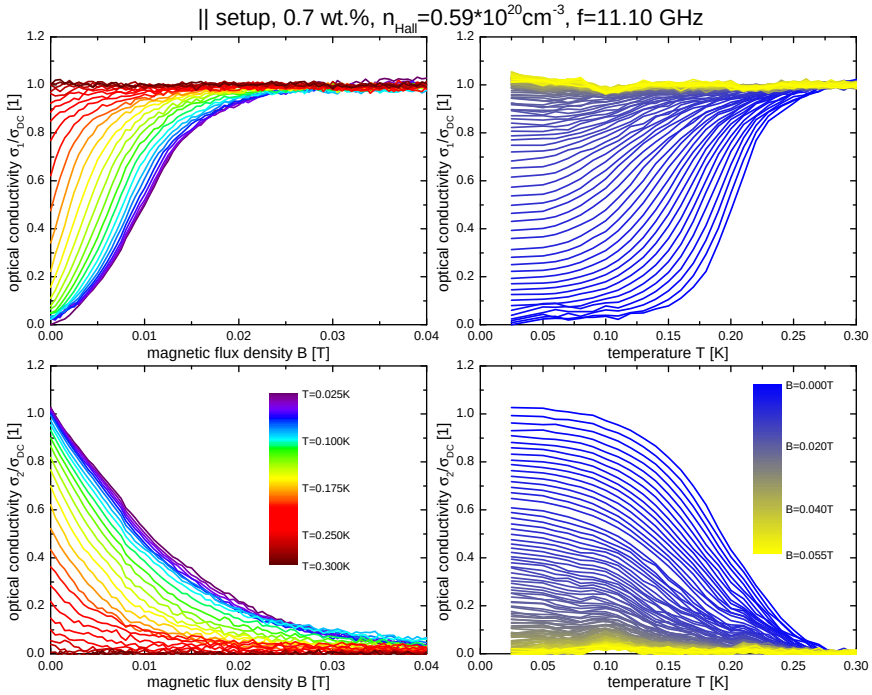

Fig. 8.11: Optical conductivity of the 0.7 wt. % Nb-doped $SrTiO_3$ sample at $f = 11.10\,\mathrm{GHz}$ in || orientation.

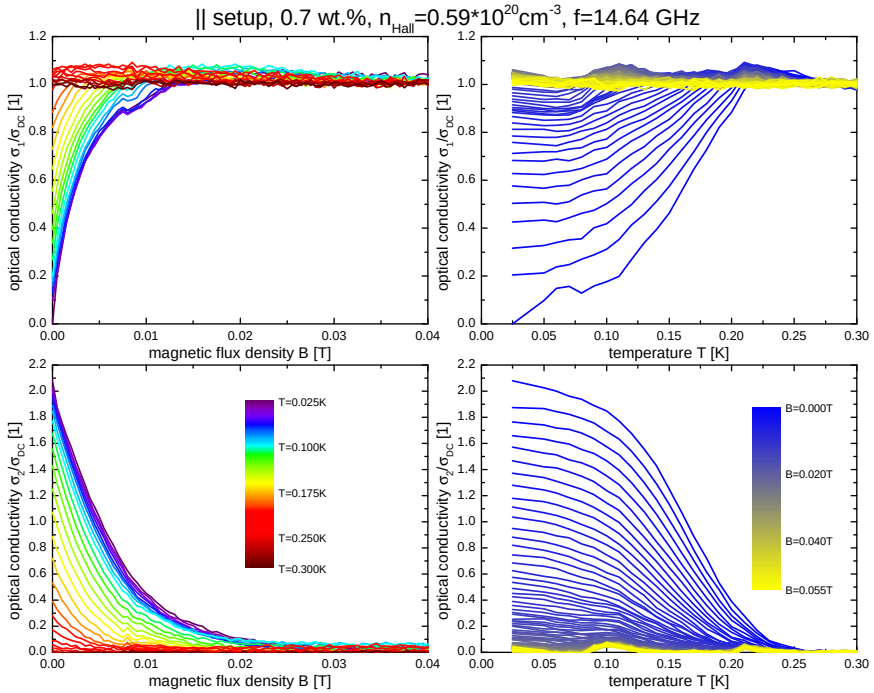

Fig. 8.12: Optical conductivity of the 0.7 wt. % Nb-doped $SrTiO_3$ sample at $f = 14.64\,\mathrm{GHz}$ in || orientation.

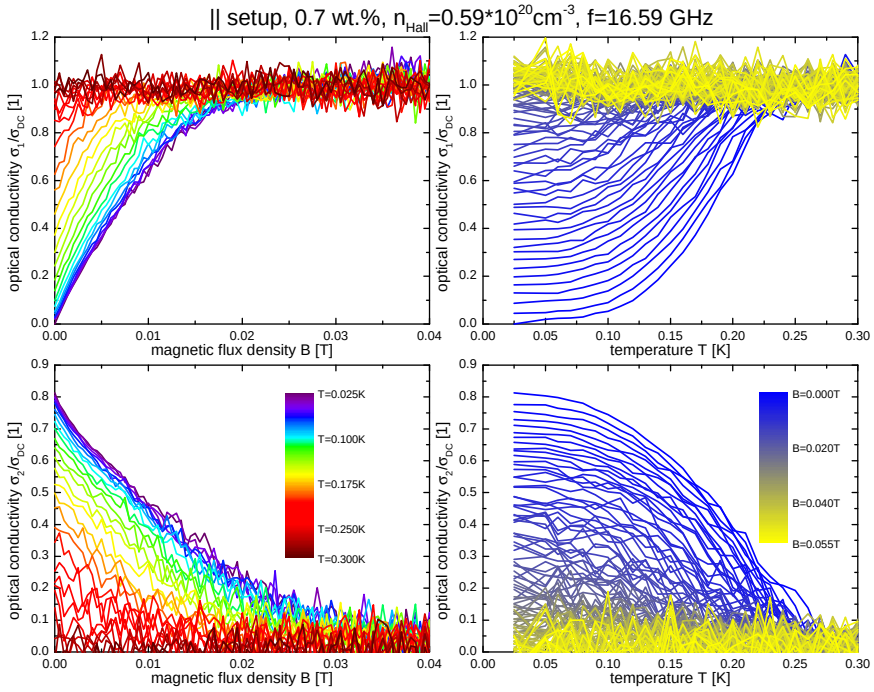

Fig. 8.13: Optical conductivity of the 0.7 wt. % Nb-doped $SrTiO_3$ sample at $f = 16.59\,\mathrm{GHz}$ in || orientation.

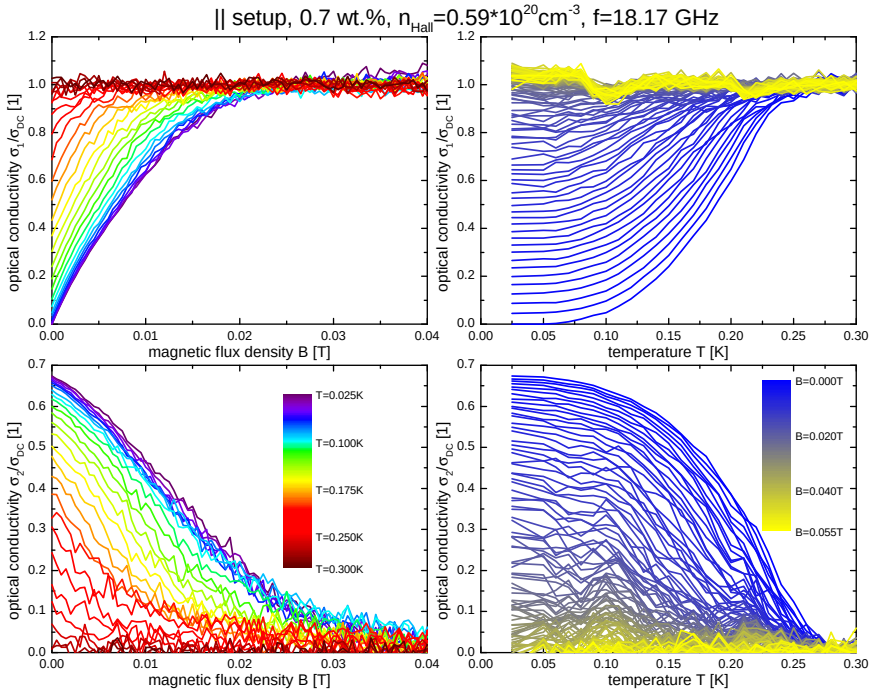

Fig. 8.14: Optical conductivity of the 0.7 wt. % Nb-doped $SrTiO_3$ sample at $f = 18.17\,\mathrm{GHz}$ in || orientation.

Deutsche Zusammenfassung

Diese Arbeit behandelt Supraleitung in Strontiumtitanat $SrTiO_3$, konkret sind Proben niobdotierten Strontiumtitanats gemessen worden. Dotiertes $SrTiO_3$ is bekannt für seine ungewöhnlich kleine Fermifläche. Supraleitendes $SrTiO_3$ zeigt ein kuppelförmiges Verhalten der kritischen Temperatur T_C in Abhängigkeit der Dotierung n. Es ist nicht abschließend geklärt, wie ein Material mit so geringer Fermienergie supraleitend werden kann, sowohl ist der Kopplungsmechanismus der Cooper-Paare nicht vollständig geklärt als auch nicht klar wie der Grundzustand eines solchen Systems mathematisch beschrieben werden muss. Diese Arbeit konzentriert sich auf die Messung der frequenzabhängigen, temperaturabhängigen und magnetfeldabhängigen optischen Leitfähigkeit $\hat{\sigma}(B, T, f)$ in Nb:$SrTiO_3$.

Die fünf untersuchten Proben in dieser Arbeit haben eine Ladungsträgerkonzentration von $n_{\text{Hall}} = 0.33 \cdot 10^{20}\,\text{cm}^{-3}$, $n_{\text{Hall}} = 0.59 \cdot 10^{20}\,\text{cm}^{-3}$, $n_{\text{Hall}} = 1.1 \cdot 10^{20}\,\text{cm}^{-3}$, $n_{\text{Hall}} = 2.0 \cdot 10^{20}\,\text{cm}^{-3}$, $n_{\text{Hall}} = 2.2 \cdot 10^{20}\,\text{cm}^{-3}$. Es wurden supraleitende Streifenleiterresonatoren verwendet um die optischen Eigenschaften von Nb:$SrTiO_3$ zu messen. Aus Supraleitern wie Blei oder Zinn hergestellte Streifenleiterresonatoren zeigen eine Änderung der Resonanzfrequenz f aufgrund der temperaturabhängigen Eigenschaften der supraleitenden Materials. Es wurde gezeigt dass die Temperaturabhängigkeit theoretisch unter Berücksichtigung der effektiven London'schen Eindringtiefe λ_{eff} beschrieben werden kann und es wurden plausible Werte für λ_{eff} für Blei und Zinn gefunden. Wenn die Grundplatte eines Streifenleiterresonators aus Blei durch eine Nb:$SrTiO_3$ Probe ersetzt wird, dann kann die optische Leitfähigkeit von Nb:$SrTiO_3$ mithilfe der Cavity Perturbation Technique bestimmt werden.

Die optische Leitfähigkeit von Nb:$SrTiO_3$ zeigt Merkmale, welche typischerweise mit einem Supraleiter mit einer einzigen Energielücke im sogenannten "dirty" limit assoziiert werden. Bei niedrigen Frequenzen wird das von der BCS Theorie vorhergesagte Kohärenzmaximum beobachtet, hier im Weiteren das T-Kohärenzmaximum genannt. Real- und Imaginärteil der optischen Leitfähigkeit zeigen in Abhängigkeit des Magnetfeldes B eine abrupte Änderung der Änderungsrate, einen Knick an der Stelle B^*. An den kritischen Magnetfeldern B^* und B_{C2} werden die zwei supraleitenden Bänder mit den zwei Kohärenzlängen ξ_{GL} in Nb:$SrTiO_3$ jeweils geleert. Der Realteil der optischen Leitfähigkeit zeigt außerdem das B-Kohärenzmaximum: Beginnend bei $B = 0$ ist das B-Kohärenzmaximum charakterisiert durch eine starke Zunahme von $\text{Re}(\hat{\sigma})$ in Abhängigkeit von B sogar bei niedrigster erreichter Temperatur T, es ist $\text{Re}(\hat{\sigma}) > \sigma_{\text{DC}}$ beobachtet worden wobei σ_{DC} die DC Leitfähigkeit ist und das B-Kohärenzmaximum ist nur für niedrige Frequenzen $hf \ll 2\Delta$ beobachtet worden.

Die kuppelförmige Abhängigkeit der kritischen Magnetfelder B^*, B_{C2} von n_{Hall} lässt $T_C^2 \propto B^\alpha$ vermuten wobei $B^\alpha = B^*, B_{C2}$ eine Platzhaltervariable ist. Mit der BCS und Ginzburg Landau Theorie kann $\Delta_0 \propto (E_F B^\alpha/m)^{1/2}$ im sogenannten "clean" limit und $\Delta_0 \propto lB^\alpha\,(E_F/m)^{1/2}$ im dirty limit erlangt werden. Wenn für die Fermienergie E_F und die

freie Weglänge l für beide Bänder derselbe Wert angenommen wird, kann eine Relation zwischen dem Verhältnis der magnetischen Felder und dem Verhältnis der effektiven Massen $B_{C2}^2/B^{*2} = m^u/m^l$ im dirty limit hergeleitet werden, diese Relation konnte experimentell bestätigt werden. Die Fermienergie is bestimmt worden, im clean limit zeigt die Fermienergie eine kuppelförmige Abhängigkeit und im dirty limit ein monoton steigendes Verhalten in Abhängigkeit der Dotierung.

Ein charakteristisches Merkmal des B-Kohärenzmaximums, die starke anfängliche Zunahme von $\mathrm{Re}(\hat{\sigma})$ in Abhängigkeit von B bei niedrigster Temperatur T, konnte mit einem theoretischen Argument reproduziert werden. Die Caroli-deGennes-Matricon Moden sind tiefliegende Zustände welche im Vortex lokalisiert sind bei der Fermienergy E_F. Die lokale Zustandsdichte $N_{\mathrm{loc}}(r, E)$ als Folge dieser tiefliegenden Zustände resultiert in einer Änderungsrate $\mathrm{dRe}(\hat{\sigma})/\mathrm{d}B|_{B=0}$ welche größer ist als es erwartet wäre von normal leitenden Vortexen mit der Ginzburg Landau Konhärenzlänge ξ_{GL} als Radius.

Die Diskussion um die Frage ob Nb:$SrTiO_3$ am besten im dirty oder clean limit beschrieben werden kann ist nicht abschließend geklärt. Auf Grundlage der Längenskalen l und ξ_{GL} kann ein Übergang vom clean zum dirty limit mit größerer Dotierung für die Proben in dieser Arbeit beobachtet werden. Die Werte für l und ξ_{GL} sind in einer ähnlichen Größenordnung, somit kann nicht behauptet werden dass die Nb:$SrTiO_3$ Proben in dieser Arbeit vom starken clean zum starken dirty limit übergehen. Nb:$SrTiO_3$ kann somit Beispiel für ein Material sein, welches als Funktion der Dotierung Eigenschaften sowohl des clean limit als auch des dirty limit zeigt.

Acknowledgments

I want to thank everybody, who made this project possible and supported me throughout. In particular I want to thank

- Prof. Dr. Martin Dressel, for giving me the opportunity to work on this project
- Prof. Dr. Sebastian Loth for being my second examiner
- Dr. Marc Scheffler, for being my supervisor and for the helpful guidance and discussions
- Gabi Untereiner for sample preparation and assembling
- the students I worked with in the lab, Anastasia Bauernfeind, Paul Kugler, Frederik Bolle, Jan Pussykeilender, Marius Tochtermann, Ishan Sarvaiya, Christian Prange, Ilenia Neureuther, Florentine Scharwächter, for a nice time
- the low temperature department, for continuous supply of liquid helium
- Piers Coleman, Premala Chandra, Maria Gastiasoro and José Lorenzana for scientific communication
- the whole of 1. Physikalisches Institut, for the pleasant research atmosphere.
- my family for being there

Eigenständigkeitserklärung

Ich, Cenk Beydeda, bestätige hiermit, dass ich die vorliegende Arbeit eigenständig verfasst habe. Es wurden keine anderen Quellen verwendet als die angegebenen und alle wörtlich oder sinngemäß aus anderen Werken übernommenen Aussagen als solche gekennzeichnet. Diese Arbeit wurde weder vollständig, noch in Teilen in einem anderen Prüfungsverfahren verwendet und weder vollständig noch in Teilen bereits veröffentlicht. Der Inhalt des elektronischen Exemplars ist mit dem Inhalt des Druckexemplars identisch.

Stuttgart, den 7. November 2022

References

[1] J. F. Schooley, W. R. Hosler, and M. L. Cohen, *Phys. Rev. Lett.* **12**, 474 (1964).

[2] G. Binnig, A. Baratoff, H. E. Hoenig, and J. G. Bednorz, *Phys. Rev. Lett.* **45**, 1352 (1980).

[3] J. F. Schooley, W. R. Hosler, E. Ambler, J. H. Becker, M. L. Cohen, and C. S. Koonce, *Phys. Rev. Lett.* **14**, 305 (1965).

[4] J. G. Bednorz and K. A. Müller, *Rev. Mod. Phys.* **60**, 585 (1988).

[5] K. A. Müller and H. Burkard, *Phys. Rev. B* **19**, 3593 (1979).

[6] S. Rowley, L. Spalek, R. Smith, M. Dean, M Itoh, J. Scott, G. Lonzarich, and S. Saxena, *Nat. Phys.* **10**, 367 (2014).

[7] V. T. Engl, N. G. Ebensperger, L. Wendel, and M. Scheffler, *arXiv* **cond-mat.supr-con**, 1911.11456 (2019).

[8] C. Collignon, X. Lin, C. Rischau, B. Fauqué, and K. Behnia, *Annu. Rev. Condens. Matter Phys.* **10**, 25 (2018).

[9] M. N. Gastiasoro, J. Ruhman, and R. M. Fernandes, *Ann. Phys.* **417**, 168107 (2020).

[10] K. Bennemann and J. Ketterson, *Superconductivity* (Springer, 2008).

[11] A Ohtomo and H. Hwang, *Nature* **427**, 423 (2004).

[12] N. Reyren, S. Thiel, A. D. Caviglia, L. F. Kourkoutis, G. Hammerl, C. Richter, C. W. Schneider, T. Kopp, A.-S. Rüetschi, D. Jaccard, M. Gabay, D. A. Muller, J.-M. Triscone, and J. Mannhart, *Science* **317**, 1196 (2007).

[13] A. Caviglia, S. Gariglio, N. Reyren, D. Jaccard, T Schneider, M Gabay, S. Thiel, G. Hammerl, J. Mannhart, and J.-M. Triscone, *Nature* **456**, 624 (2008).

[14] S. Goswami, E. Mulazimoglu, A. M. Monteiro, R. Wölbing, D. Koelle, R. Kleiner, Y. M. Blanter, L. M. Vandersypen, and A. D. Caviglia, *Nat. Nanotechnol.* **11**, 861 (2016).

[15] A. G. Swartz, H. Inoue, T. A. Merz, Y. Hikita, S. Raghu, T. P. Devereaux, S. Johnston, and H. Y. Hwang, *Proc. Natl. Acad. Sci.* **115**, 1475 (2018).

[16] X. Lin, A. Gourgout, G. Bridoux, F. m. c. Jomard, A. Pourret, B. Fauqué, D. Aoki, and K. Behnia, *Phys. Rev. B* **90**, 140508 (2014).

[17] M. Thiemann, M. H. Beutel, M. Dressel, N. R. Lee-Hone, D. M. Broun, E. Fillis-Tsirakis, H. Boschker, J. Mannhart, and M. Scheffler, *Phys. Rev. Lett.* **120**, 237002 (2018).

[18] P. Anderson, *J. Phys. Chem. Solids* **11**, 26 (1959).

[19] C. Collignon, B. Fauqué, A. Cavanna, U. Gennser, D. Mailly, and K. Behnia, *Phys. Rev. B* **96**, 224506 (2017).

[20] J. C. Maxwell, *Philos. Trans. Roy. Soc. London* **155**, 459 (1865).

[21] M. Dressel and G. Grüner, *Electrodynamics of solids: optical properties of electrons in matter* (Cambridge University Press, 2011).

[22] R. E. Collin, *Foundations for microwave engineering* (John Wiley & Sons, 2000).

[23] G. S. Ohm, *Die galvanische kette: mathematisch* (TH Riemann, 1827).

[24] J. S. Toll, *Phys. Rev.* **104**, 1760 (1956).

[25] H. Kamerlingh Onnes, *Comm. Phys. Lab. Univ. Leiden* **122**, 122 (1911).

[26] J. Bardeen, L. N. Cooper, and J. R. Schrieffer, *Phys. Rev.* **108**, 1175 (1957).

[27] W. S. Corak, B. B. Goodman, C. B. Satterthwaite, and A. Wexler, *Phys. Rev.* **96**, 1442 (1954).

[28] W. Meissner and R. Ochsenfeld, *Naturwissenschaften* **21**, 787 (1933).

[29] W. L. McMillan, *Phys. Rev.* **167**, 331 (1968).

[30] J. G. Bednorz and K. A. Müller, *Z. Phys. B Con. Mat.* **64**, 189.

[31] M. Ruby, B. W. Heinrich, J. I. Pascual, and K. J. Franke, *Phys. Rev. Lett.* **114**, 157001 (2015).

[32] U. S. Pracht, N. Bachar, L. Benfatto, G. Deutscher, E. Farber, M. Dressel, and M. Scheffler, *Phys. Rev. B* **93**, 100503 (2016).

[33] M. Tinkham, *Introduction to superconductivity* (Dover Publications, 2004).

[34] P.-G. De Gennes and P. A. Pincus, *Superconductivity of metals and alloys* (CRC Press, 1999).

[35] V. V. Schmidt, V. Schmidt, P. Müller, and A. V. Ustinov, *The physics of superconductors: introduction to fundamentals and applications* (Springer Science & Business Media, 1997).

[36] T. Kita, *Statistical mechanics of superconductivity* (Springer, 2015).

[37] J. R. Schrieffer, *Theory of superconductivity* (CRC press, 1999).

[38] A. Altland and B. D. Simons, *Condensed matter field theory*, 2nd ed. (Cambridge University Press, 2010).

[39] L. N. Cooper, *Phys. Rev.* **104**, 1189 (1956).

[40] N. W. Ashcroft and N. D. Mermin, *Solid state physics* (Brooks/Coole Cengage Learning, 2010).

[41] L. P. Gor'kov, *Sov. Phys. JETP* **9**, 1364 (1959).

[42] F. Marsiglio, *Ann. Phys.* **417**, 168102 (2020).

[43] F. London and H. London, *Proc. R. Soc. A: Math. Phys. Eng. Sci.* **149**, 71.

[44] A. B. Pippard and W. L. Bragg, *Proc. R. Soc. A: Math. Phys. Eng. Sci.* **216**, 547 (1953).

[45] D. C. Mattis and J. Bardeen, *Phys. Rev.* **111**, 412 (1958).

[46] W. Zimmermann, E. Brandt, M. Bauer, E. Seider, and L. Genzel, *Phys. C: Supercond. Appl.* **183**, 99 (1991).

[47] O. Klein, E. J. Nicol, K. Holczer, and G. Grüner, *Phys. Rev. B* **50**, 6307 (1994).

[48] A. A. Abrikosov, *Soviet Physics-JETP* **5**, 1174 (1957).

[49] R. E. Collin, *Field theory of guided waves* (John Wiley & Sons, 1991).

[50] H. M. Altschuler and A. A. Oliner, *IEEE Trans. Microw. Theory Techn.* **8**, 328 (1960).

[51] D. M. Pozar, *Microwave engineering* (John Wiley & Sons, Inc., 2011).

[52] H. Zu, W. Dai, and A. de Waele, *Cryogenics* **121**, 103390 (2022).

[53] M. Scheffler, M. M. Felger, M. Thiemann, D. Hafner, K. Schlegel, M. Dressel, K. S. Ilin, M. Siegel, S. Seiro, C. Geibel, *et al.*, *ACTA IMEKO* **4**, 47 (2015).

[54] Y. Wiemann, J. Simmendinger, C. Clauss, L. Bogani, D. Bothner, D. Koelle, R. Kleiner, M. Dressel, and M. Scheffler, *Appl. Phys. Lett.* **106**, 193505 (2015).

[55] M. Thiemann, M. Dressel, and M. Scheffler, *Phys. Rev. B* **97**, 214516 (2018).

[56] M. Scheffler, K. Schlegel, C. Clauss, D. Hafner, C. Fella, M. Dressel, M. Jourdan, J. Sichelschmidt, C. Krellner, C. Geibel, and F. Steglich, *Phys. Status Solidi B* **250**, 439 (2013).

[57] D. Hafner, M. Dressel, and M. Scheffler, *Rev. Sci. Instrum.* **85**, 014702 (2014).

[58] D. Hafner, M. Dressel, O. Stockert, K. Grube, H. v. Löhneysen, and M. Scheffler, *JPS Conf. Proc.* **3**, 012016 (2014).

[59] H. Wheeler, *IEEE Trans. Microw. Theory Techn.* **26**, 866 (1978).

[60] N. Marcuvitz, *Waveguide handbook* (Peregrinus, London, 1993).

[61] A. Oliner, *IEEE Trans. Microw. Theory Techn.* **3**, 134 (1955).

[62] D. S. Rausch, M. Thiemann, M. Dressel, D. Bothner, D. Koelle, R. Kleiner, and M. Scheffler, *J. Phys. D: Appl. Phys.* **51**, 465301 (2018).

[63] O. Klein, S. Donovan, M. Dressel, and G. Grüner, *Int. J. Infrared Millim. Waves* **14**, 2423 (1993).

[64] S. Donovan, O. Klein, M. Dressel, K. Holczer, and G. Grüner, *Int. J. Infrared Millim. Waves* **14**, 2459 (1993).

[65] M. Dressel, O. Klein, S. Donovan, and G. Grüner, *Int. J. Infrared Millim. Waves* **14**, 2489 (1993).

[66] H. H. Howe, *Stripline circuit design* (Artech House Dedham, MA, 1974).

[67] C. Kittel, *Introduction to solid state physics* (John Wiley & Sons, Inc., 2004).

[68] A. B. Pippard and W. L. Bragg, *Proc. R. Soc. A: Math. Phys. Eng. Sci.* **191**, 370 (1947).

[69] A. B. Pippard and W. L. Bragg, *Proc. R. Soc. A: Math. Phys. Eng. Sci.* **191**, 385 (1947).

[70] A. B. Pippard and W. L. Bragg, *Proc. R. Soc. A: Math. Phys. Eng. Sci.* **191**, 399 (1947).

[71] H. Wheeler, *Proceedings of the IRE* **30**, 412 (1942).

[72] J. Eisenstein, *Rev. Mod. Phys.* **26**, 277 (1954).

[73] J. A. Noland, *Phys. Rev.* **94**, 724 (1954).

[74] R. G. Geyer, B. Riddle, J. Krupka, and L. A. Boatner, *J. Appl. Phys.* **97**, 104111 (2005).

[75] C. S. Koonce, M. L. Cohen, J. F. Schooley, W. R. Hosler, and E. R. Pfeiffer, *Phys. Rev.* **163**, 380 (1967).

[76] X. Lin, Z. Zhu, B. Fauqué, and K. Behnia, *Phys. Rev. X* **3**, 021002 (2013).

[77] Y. Takada, *J. Phys. Soc. Jpn.* **49**, 1267 (1980).

[78] V. Engl, *Planar microwave resonators on srtio3 substrates* (MSc thesis, University of Stuttgart, 2019).

[79] L. Wendel, V. T. Engl, G. Untereiner, N. G. Ebensperger, M. Dressel, A. Farag, M. Ubl, H. Giessen, and M. Scheffler, *Rev. Sci. Instrum.* **91**, 054702 (2020).

[80] X. Lin, G. Bridoux, A. Gourgout, G. Seyfarth, S. Krämer, M. Nardone, B. Fauqué, and K. Behnia, *Phys. Rev. Lett.* **112**, 207002 (2014).

[81] X. Lin, B. Fauqué, and K. Behnia, *Science* **349**, 945 (2015).

[82] D. van der Marel, J. L. M. van Mechelen, and I. I. Mazin, *Phys. Rev. B* **84**, 205111 (2011).

[83] X. Lin, C. W. Rischau, C. J. van der Beek, B. Fauqué, and K. Behnia, *Phys. Rev. B* **92**, 174504 (2015).

[84] C. Homes, S. Dordevic, M Strongin, D. Bonn, R. Liang, W. Hardy, S. Komiya, Y. Ando, G Yu, N Kaneko, *et al.*, *Nature* **430**, 539 (2004).

[85] C. Collignon, P. Bourges, B. Fauqué, and K. Behnia, *Phys. Rev. X* **10**, 031025 (2020).

[86] C. Collignon, Y. Awashima, Ravi, X. Lin, C. W. Rischau, A. Acheche, B. Vignolle, C. Proust, Y. Fuseya, K. Behnia, and B. Fauqué, *Phys. Rev. Materials* **5**, 065002 (2021).

[87] A. Stucky, G. Scheerer, Z. Ren, D. Jaccard, J.-M. Poumirol, C. Barreteau, E. Giannini, and D. Van Der Marel, *Sci. Rep.* **6**, 37582 (2016).

[88] M. Thiemann, *Microwave investigations on superconducting nb-doped srtio3* (Doctor thesis, University of Stuttgart, 2018).

[89] M. Zinßer, *Microwave investigations on srtio3-based materials at mk temperatures* (MSc thesis, University of Stuttgart, 2018).

[90] N. G. Ebensperger, M. Thiemann, M. Dressel, and M. Scheffler, *Supercond. Sci. Technol.* **29**, 115004 (2016).

[91] J. Bardeen and M. J. Stephen, *Phys. Rev.* **140**, A1197 (1965).

[92] K. Steinberg, M. Scheffler, and M. Dressel, *Phys. Rev. B* **77**, 214517 (2008).

[93] R. Mallozzi, J. Orenstein, J. N. Eckstein, and I. Bozovic, *Phys. Rev. Lett.* **81**, 1485 (1998).

[94] D. Bothner, T. Gaber, M. Kemmler, D. Koelle, R. Kleiner, S. Wünsch, and M. Siegel, *Phys. Rev. B* **86**, 014517 (2012).

[95] C. Caroli, P. De Gennes, and J. Matricon, *Phys. Lett.* **9**, 307 (1964).

[96] M. Abramowitz and I. A. Stegun, *Handbook of mathematical functions with formulas, graphs, and mathematical tables*, Vol. 55 (US Government printing office, 1964).

[97] U. S. Pracht, M. Scheffler, M. Dressel, D. F. Kalok, C. Strunk, and T. I. Baturina, *Phys. Rev. B* **86**, 184503 (2012).

[98] M. Šindler, R. Tesař, J. Koláček, L. Skrbek, and Z. Šimša, *Phys. Rev. B* **81**, 184529 (2010).

[99] T. C. Choy, ed., *Effective medium theory: principles and applications*, Englisch, Repr., International series of monographs on physics ; 102, Includes bibliographical references and index (Oxford University Press, Oxford, 2007).

[100] H. F. Hess, R. B. Robinson, R. C. Dynes, J. M. Valles, and J. V. Waszczak, *Phys. Rev. Lett.* **62**, 214 (1989).

[101] H. F. Hess, R. B. Robinson, and J. V. Waszczak, *Phys. Rev. Lett.* **64**, 2711 (1990).

[102] I. Guillamón, H. Suderow, S. Vieira, L. Cario, P. Diener, and P. Rodière, *Phys. Rev. Lett.* **101**, 166407 (2008).

[103] A. Fente, E. Herrera, I. Guillamón, H. Suderow, S. Mañas Valero, M. Galbiati, E. Coronado, and V. G. Kogan, *Phys. Rev. B* **94**, 014517 (2016).

[104] F. Gygi and M. Schlüter, *Phys. Rev. B* **43**, 7609 (1991).

[105] J. D. Shore, M. Huang, A. T. Dorsey, and J. P. Sethna, *Phys. Rev. Lett.* **62**, 3089 (1989).

[106] N. Hayashi, T. Isoshima, M. Ichioka, and K. Machida, *Phys. Rev. Lett.* **80**, 2921 (1998).

[107] C. Renner, A. D. Kent, P. Niedermann, Ø. Fischer, and F. Lévy, *Phys. Rev. Lett.* **67**, 1650 (1991).

[108] L. Kramer and W. Pesch, *Z. Physik* **269**, 59 (1974).